

THE STUDY OF BETA-DELAYED NEUTRON DECAY  
NEAR THE NEUTRON DRIP LINE

By

Chandana Sujeewa Sumithrarachchi

A DISSERTATION

Submitted to  
Michigan State University  
in partial fulfillment of the requirements  
for the degree of

DOCTOR OF PHILOSOPHY

Department of Chemistry

2007

# ABSTRACT

The Study of Beta-delayed Neutron Decay Near The Neutron Drip Line

By

Chandana Sujeewa Sumithrarachchi

The study of neutron-rich oxygen and fluorine isotopes can provide important information on the evolution of nuclear shell structure close to the neutron drip line. The structural changes in this region are reflected with observations of the rapid change in the location of the drip line at fluorine and appearance of a new shell closure at  $N = 14$ . The recent experiments along with the shell model calculations provide evidence for the doubly magic nature of  $^{22}\text{O}$ . The negative parity states in  $^{22}\text{O}$  rooted in the neutron  $pf$  orbitals are not experimentally known. The knowledge of nuclear structure in  $^{23}\text{F}$ , which has the structure of a single proton outside the doubly magic  $^{22}\text{O}$ , is also important as it should be sensitive to the proton  $s$  and  $d$  orbital splitting. The present work focused on the beta-delayed neutron and gamma-ray spectroscopies from  $^{22}\text{N}$  and  $^{23}\text{O}$  beta decay.

The measurements of  $^{22}\text{N}$  and  $^{23}\text{O}$  were carried out at the NSCL using fragments from the reaction of  $^{48}\text{Ca}$  beam in a Be target. The desired isotopes were stopped in the implantation detector and then monitored for beta-delayed neutrons and gamma-rays using a neutron spectroscopic array and eight detectors from SeGA, respectively. The half-lives and the total neutron emission probabilities were determined to be 20(2) and 97(8) ms, and 57(5)% and 7(2)%, respectively, for  $^{22}\text{N}$  and  $^{23}\text{O}$ . Single and two beta-delayed neutron decay of  $^{22}\text{N}$  was observed and five new negative parity states identified in  $^{22}\text{O}$ . The measurement also revealed three gamma-ray transitions in  $^{22}\text{O}$  and a single gamma-ray for each in  $^{21}\text{O}$  and  $^{20}\text{O}$  associated with the beta-delayed neutron decay of  $^{22}\text{N}$ . Ten gamma-ray decays in  $^{23}\text{F}$  and a single gamma-ray in  $^{22}\text{F}$  were observed from  $^{23}\text{O}$  beta decay. The tentative decay schemes of  $^{22}\text{N}$  and

$^{23}\text{O}$  were established and compared with shell model calculations. The beta decays of the major contaminants in the beam from the fragment separator  $^{25}\text{F}$ ,  $^{24}\text{O}$  and  $^{26}\text{Ne}$  have been investigated to establish decay schemes as well.

The observation of a relatively high energy for the first  $2^+$  state in  $^{22}\text{O}$  supports the shell closure at  $N = 14$ . The observation of large beta decay strength at high excitation energies in  $^{22}\text{O}$  indicates the indirect evidence for the halo structure of  $^{22}\text{N}$ . The experimental results of the  $^{22}\text{N}$  beta decay are in poor agreement with the shell model calculations suggesting the evolution of single particle structure in this region. However, the overall beta decay results of  $^{23}\text{O}$  are in reasonable agreement with shell model calculations. The excitation energies of the first  $1/2^+$  and  $3/2^+$  states in  $^{23}\text{F}$  have been determined at 2243 and 3866 keV and show a widening of the  $5/2^+ - 1/2^+$  state gap indicating the appearance of the  $N=14$  shell closure in the fluorine isotopes.

*To*  
*my mother, my wife Indikani, my daughter Manekya*  
*all my teachers*  
*and friends*

## ACKNOWLEDGMENTS

It is impossible in words to really express the gratitude that I have to the people who I have worked with and met along this road. Without the support, patience and guidance of the following people, this study would not have been completed. First I owe my deepest gratitude to my advisor, Professor Dave J. Morrissey, for his guidance, supervision, and encouragement during this work. His patience, sense of humor, and understanding has been greatly appreciated and are acknowledged. I must especially thank him for his efforts during my experiment, for the experience I gained from working alongside him and allowing me to work independently, while always being available to help. I thank Professor Paul Mantica for being my second reader and giving additional guidance. His support during experiment and suggestions to complete this work have been especially acknowledged. The contributions of my committee to my education will always be remembered. I would like to thank Professors Michael Thoennesen and Hendrik Schatz for working as members of my dissertation committee and for giving advice through this work. The NSCL technical staff is totally outstanding and helped make the project real. I really need to thank Mr. Len Morris for his design work, the NSCL Machine Shop for producing parts for our setup and all cyclotron operators. I wish to thank Dr. Mauricio Portillo for support through A1900 work and Professor Thomas Glasmacher and the gamma group for providing the support in use of SeGA. I am grateful to Professor Alex Brown for providing shell model calculations for this work.

There are multiple people I would like to acknowledge for their contributions during the experiment. I would like to thank Andrew, Debbie, Elaine, Josh, Weerasiri, Dr. Fancina and Dr. Shimbara giving support thorough the experiment. I especially want to thank Elain Kwan for all her help. Our long discussions were inspiring to me. I have appreciated your friendship and willingness to help along the way. I wish to thank the Morrissey group members, Dr. Folden and Greg Pang for discussions

about various projects. My fellow graduate students at the lab were also invaluable during my time at the lab. I offer special thanks to my officemates Wes, Greg, Josh and Philip, to great friends from the accelerator group, Susan and from the theory group, Jeremy and former graduate students Bryan, Sean and Tao for the interesting conversations to make time in graduate school enjoyable. I wish to thank Jeremy for reading this.

I am grateful to the Department of Chemistry, Michigan State University and the National Science Foundation for their financial support during this work. I wish to thank especially the Chemistry Graduate Office, Lisa and Debbie for their kind help throughout my studies.

The people that heard me grip the most over the past three years have been my family. I cannot imagine being where I am today without them, and I am blessed to have had their unconditional love and support throughout my academic career and my life. Ariyawathej Sumithrarachchi, my mother, who has always supported, encouraged and believed in me, in all my endeavors. Inikani, my wife, without whom this effort would have been worth nothing. Your love, support and constant patience have taught me so much about sacrifice, discipline and compromise. I want to mention here about my loving daughter, Manekya. She is everything for me. Her love is always a gripe to my life.

# Contents

<b>1</b>	<b>Introduction</b>	<b>1</b>
1.1	Location of The Neutron Drip Line . . . . .	5
1.2	Disappearance of Traditional Magic Numbers . . . . .	6
1.3	Shell closure at $N = 14$ and $N = 16$ . . . . .	7
1.4	Halo structures near neutron drip line . . . . .	9
1.5	Motivation . . . . .	11
1.5.1	Knowledge of the Structure of $^{22}\text{O}$ and $^{22}\text{N}$ . . . . .	11
1.5.2	Knowledge on the Structure of $^{23}\text{F}$ and $^{23}\text{O}$ . . . . .	14
1.6	Present Work . . . . .	16
<b>2</b>	<b>Overview of Beta Decay</b>	<b>17</b>
2.1	Theory of Beta Decay . . . . .	18
2.1.1	Selection Rules . . . . .	21
2.2	Beta-delayed Neutron Decay . . . . .	23
2.3	Gamma-ray decay . . . . .	23
2.4	Gamow-Teller Transition strength . . . . .	24
2.5	Application . . . . .	26
<b>3</b>	<b>Experimental Setup</b>	<b>28</b>
3.1	Fragment Production . . . . .	28
3.2	Implantation Detector System . . . . .	31
3.2.1	Data Acquisition System . . . . .	33
3.3	Neutron Spectroscopic Array . . . . .	36
3.3.1	Detail of the Neutron Spectroscopic Array . . . . .	36
3.3.2	Neutron Energy Calibration . . . . .	38
3.3.3	Neutron Peak Shape and The Background . . . . .	44
3.3.4	Time Walk Correction . . . . .	46
3.3.5	Neutron Efficiency Calibration . . . . .	48
3.4	Segmented Germanium Detector Array . . . . .	51
3.4.1	SeGA detectors . . . . .	51
3.4.2	SeGA Energy Calibration . . . . .	52
3.4.3	SeGA Efficiency Calibration . . . . .	54
<b>4</b>	<b>Data Analysis and Results</b>	<b>59</b>
4.1	Anaysis of The $^{22}\text{N}$ Beta Decay Experiment . . . . .	59
4.1.1	Total Number of Beta Decay Events . . . . .	61

4.1.2	The analysis of the neutron time-of-flight spectrum from $^{22}\text{N}$ cocktail beam . . . . .	64
4.1.3	Gamma-ray Identification . . . . .	66
4.1.4	Beta Decay Scheme of $^{22}\text{N}$ . . . . .	71
4.2	Beta Decay of $^{25}\text{F}$ . . . . .	76
4.3	Beta Decay of $^{24}\text{O}$ . . . . .	83
4.4	Analysis of $^{23}\text{O}$ Beta Decay Experiment . . . . .	89
4.4.1	Total Number of Beta Decay Events . . . . .	92
4.4.2	Beta-delayed neutron time-of-flight measurement . . . . .	94
4.4.3	Beta-delayed gamma-ray measurement . . . . .	97
4.4.4	Beta Decay Scheme of $^{23}\text{O}$ . . . . .	99
4.5	Beta Decay of $^{26}\text{Ne}$ . . . . .	102
<b>5</b>	<b>Discussion</b> . . . . .	<b>108</b>
5.1	Beta Decay of $^{22}\text{N}$ . . . . .	108
5.2	Beta Decay of $^{23}\text{O}$ and Energy States in $^{23}\text{F}$ . . . . .	112
5.3	The $1^+$ Excited States in $^{26}\text{Na}$ . . . . .	117
5.4	The Half-lives and Total Neutron Emission Probabilities of Neutron-rich Light Nuclei . . . . .	119
5.5	Conclusion and Summary . . . . .	120
<b>A</b>	<b>Beta Decay Fitting Model</b> . . . . .	<b>122</b>
<b>B</b>	<b>Gamma-ray Spectrum Analysis</b> . . . . .	<b>128</b>
	<i>Bibliography</i> . . . . .	135

# List of Figures

1.1	The differential single neutron separation energy . . . . .	1
1.2	Schematic diagram of the single-particle states . . . . .	3
1.3	Part of the chart of nuclides . . . . .	4
1.4	Single neutron separation energies for nuclides of different isospin . . . . .	6
1.5	The excitation energy of the lowest $2^+$ states of even-even oxygen isotopes . . . . .	8
1.6	Beta decay of the halo nuclei $^{11}\text{Li}$ and $^{11}\text{Be}$ . . . . .	10
1.7	Level scheme of $^{22}\text{O}$ . . . . .	12
1.8	Beta decay chain of $^{22}\text{N}$ . . . . .	13
1.9	Beta decay chain of $^{23}\text{O}$ . . . . .	14
1.10	Experimentally known energy levels in $^{23}\text{F}$ . . . . .	15
2.1	Schematic diagram of Beta-delayed Neutron Decay . . . . .	23
3.1	Schematic diagram of the NSCL Coupled Cyclotron Facility and the A1900 fragment separator . . . . .	29
3.2	Experimental setup with the neutron and SeGA array . . . . .	31
3.3	Implantation detector system . . . . .	32
3.4	Electronic setup for the implantation detector . . . . .	35
3.5	Schematic electronic diagram for the neutron bar array . . . . .	37
3.6	The time calibration spectrum for the neutron detector . . . . .	38
3.7	Total neutron time-of-flight spectra of $^{16}\text{C}$ and $^{17}\text{N}$ . . . . .	42
3.8	Energy calibration of the neutron array . . . . .	43
3.9	Peak shape calibration . . . . .	45
3.10	Study of neutron background shape . . . . .	46
3.11	A scatter-plot of time vs. energy from a PMT . . . . .	47
3.12	Beta decay curves of $^{16}\text{C}$ and $^{17}\text{N}$ . . . . .	49
3.13	Neutron efficiency calibration . . . . .	50
3.14	Schematic diagram of the implantation detector and SeGA array . . . . .	52
3.15	Schematic electronic diagram for SeGA array . . . . .	53
3.16	Residuals of the energy calibration for seGA detectors . . . . .	54
3.17	Coincidence efficiency calibration for SeGA: $^{22}\text{N}$ experiment . . . . .	57
3.18	Coincidence efficiency calibration for SeGA: $^{23}\text{O}$ experiment . . . . .	57
4.1	Identification of nuclides produced in $^{22}\text{N}$ experiment . . . . .	59
4.2	Growth and decay curves for the $^{22}\text{N}$ decay series . . . . .	62
4.3	Ungated beta decay curve of the $^{22}\text{N}$ experiment . . . . .	63

4.4	Neutron time-of-flight spectrum from the $^{22}\text{N}$ experiment . . . . .	65
4.5	Neutron gated decay curves from the $^{22}\text{N}$ experiment . . . . .	67
4.6	Total beta-gamma coincidence spectrum from the $^{22}\text{N}$ experiment: Part I . . . . .	68
4.7	Total beta-gamma coincidence spectrum from the $^{22}\text{N}$ experiment: Part II . . . . .	69
4.8	Two gamma gated half-lives from the $^{22}\text{N}$ beta decay . . . . .	71
4.9	Beta decay scheme of $^{22}\text{N}$ . . . . .	72
4.10	The $^{25}\text{F}$ beta decay chain . . . . .	78
4.11	Growth and decay curves for the $^{25}\text{F}$ decay series . . . . .	79
4.12	Gamma gated half-lives for the $^{25}\text{F}$ beta decay . . . . .	80
4.13	Beta decay scheme of $^{25}\text{F}$ . . . . .	82
4.14	$^{24}\text{O}$ beta decay chain . . . . .	84
4.15	Growth and decay curves for the $^{24}\text{O}$ decay series . . . . .	85
4.16	Gamma gated decay curves of the $^{24}\text{O}$ beta decay . . . . .	86
4.17	Beta decay scheme of $^{24}\text{O}$ . . . . .	88
4.18	The identification of implanted nuclides . . . . .	89
4.19	Growth and decay curves for the $^{23}\text{O}$ decay series . . . . .	91
4.20	Ungated beta decay curve for the $^{23}\text{O}$ . . . . .	92
4.21	Neutron time-of-flight spectrum: the $^{23}\text{O}$ experiment . . . . .	94
4.22	Beta-gamma coincidence spectrum for $^{23}\text{O}$ experiment: Part I . . . . .	95
4.23	Beta-gamma coincidence spectrum for $^{23}\text{O}$ experiment: Part II . . . . .	96
4.24	Gamma gated beta decay curve of $^{23}\text{O}$ . . . . .	98
4.25	Beta decay scheme of $^{23}\text{O}$ . . . . .	100
4.26	Known level scheme of $^{26}\text{Na}$ . . . . .	102
4.27	$^{26}\text{Ne}$ beta decay chain . . . . .	103
4.28	Gamma gated half-lives of $^{26}\text{Ne}$ beta decay . . . . .	104
4.29	Beta decay scheme of $^{26}\text{Ne}$ . . . . .	106
5.1	Comparison of half-life and neutron emission probability of $^{22}\text{N}$ . . . . .	109
5.2	Theoretical beta decay scheme of $^{22}\text{N}$ . . . . .	110
5.3	Comparison of the su22O energy levels . . . . .	111
5.4	Comparison of Gamow-Teller strengths B(GT) for the beta decay of $^{22}\text{N}$ . . . . .	113
5.5	Theoretical decay scheme of $^{23}\text{O}$ . . . . .	114
5.6	Comparison of $^{23}\text{F}$ levels . . . . .	115
5.7	Comparison of beta decay branching and Gamow-Teller strengths for the beta decay of $^{23}\text{O}$ . . . . .	116
5.8	The location of experimental energy states in odd-mass fluorine isotopes . . . . .	117
5.9	Theoretical beta decay scheme of $^{26}\text{Ne}$ . . . . .	118
5.10	Variation of half-lives and neutron emission probabilities with neutron number . . . . .	119
A.1	The growth and decay of the parent nucleus . . . . .	123

# List of Tables

2.1	Classification of beta decay	22
3.1	A1900 magnet settings and beam purity at the A1900	30
3.2	Calculated and actual degrader thickness	32
3.3	Beam-on/off period, half-life and production rates	33
3.4	Time calibration results for neutron detectors	39
3.5	Energy calibration results for neutron detectors	41
3.6	Fitting data from $^{16}\text{C}$ and $^{17}\text{N}$ neutron time-of-flight spectra	42
3.7	Energy calibration of neutron array	43
3.8	Neutron peak shape calibration	44
3.9	Time walk correction functions	48
3.10	Efficiency calibration of neutron array	51
3.11	Off-line coincidence efficiency calibration data for SeGA	55
3.12	On-line coincidence efficiency calibration data for SeGA: $^{22}\text{N}$ experiment	56
3.13	On-line coincidence efficiency calibration data for SeGA: $^{23}\text{O}$ experiment	58
4.1	Beam composition of $^{22}\text{N}$ experiment after the A1900 and at the im- plantation detector	61
4.2	Detected beta decay events from the $^{22}\text{N}$ experiment	64
4.3	$^{22}\text{N}$ neutron time-of-flight fitting data, neutron energies and gated half- lives	66
4.4	Assignments of gamma-ray and neutron energies for beta decay of $^{22}\text{N}$	75
4.5	Properties of the $^{22}\text{N}$ beta decay	76
4.6	Gamma-ray and neutron energies assignments for the $^{25}\text{F}$ beta decay	81
4.7	Properties of the $^{25}\text{F}$ beta decay	83
4.8	Gamma-ray and neutron energies assignments for the beta decay of $^{24}\text{O}$	87
4.9	Properties of the $^{24}\text{O}$ beta decay	89
4.10	Beam purity of the $^{23}\text{O}$ experiment from the A1900 and the implanta- tion detector	90
4.11	Detected beta decay events from the $^{23}\text{O}$ experiment	93
4.12	Gamma-ray assignment for the beta decay of $^{23}\text{O}$	99
4.13	Properties of the $^{23}\text{O}$ beta decay	101
4.14	Gamma-ray assignment for the beta decay of $^{26}\text{Ne}$	105
4.15	Properties of the $^{26}\text{Ne}$ beta decay	107
A.1	Decay curve fitting parameters	127

B.1	Gamma-ray measurements and literature data for $^{22}\text{N}$ (I) . . . . .	128
B.2	Gamma-ray measurements and literature data for $^{22}\text{N}$ (II) . . . . .	129
B.3	Gamma-ray measurements and literature data for $^{22}\text{N}$ (III) . . . . .	130
B.4	Gamma-ray measurements and literature data for $^{22}\text{N}$ (IV) . . . . .	131
B.5	Gamma-ray measurements and literature data for $^{22}\text{N}$ (V) . . . . .	132
B.6	Gamma-ray measurements and literature data for $^{23}\text{O}$ (I) . . . . .	133
B.7	Gamma-ray measurements and literature data for $^{23}\text{O}$ (II) . . . . .	134

# Chapter 1

## Introduction

Quantum mechanical shell structure is a very important aspect of nuclear structure. The most simple study of bulk properties of nuclei close to the valley of stability shows evidence for the existence of shell structure in the nucleus. As an example, Fig. 1.1 shows the difference between single neutron separation energies of neighboring isotopes as a function of neutron number(N). The peaks suggest that nuclear systems with certain nucleon numbers called magic numbers have extra stability. The known magic nucleon numbers are 2, 8, 20, 28, 50, 82, and 126, which are seen from the

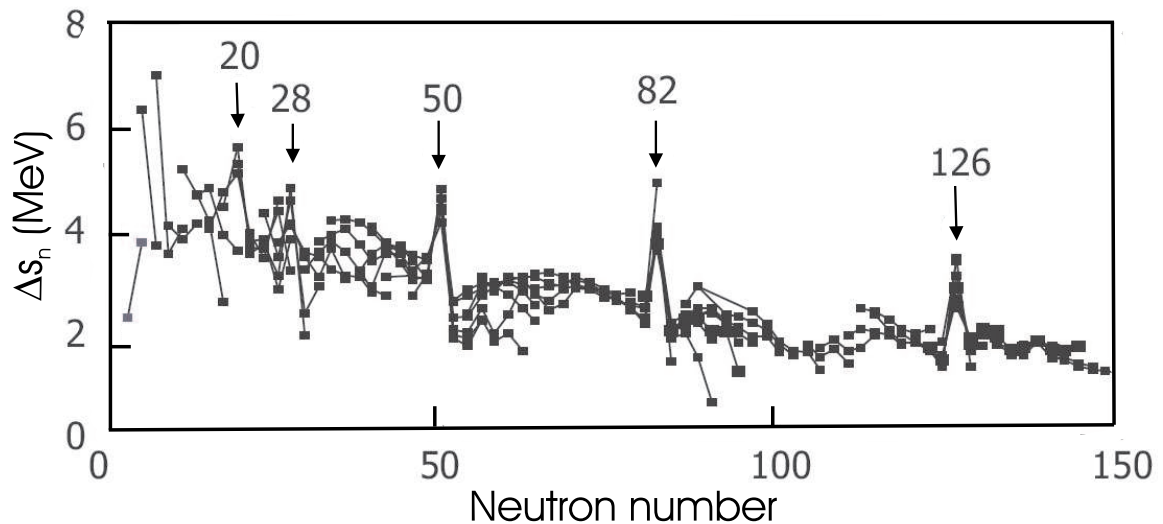


Figure 1.1: The difference between single neutron separation energies of neighboring isotopes as a function of neutron number [1]. The magic nucleon numbers are shown. Series of isotopes are connected by lines.

properties of nuclei close to the valley of stability [2]. Over time several descriptions have been used in the shell model to represent a nuclear system in terms of neutrons and protons, and their underlying interactions in order to explain nuclear properties including magic numbers. In the simple shell model, the motion of each nucleon is governed by the attractive force of all other nucleons resulting in the formation of a average potential well and individual orbitals. Several types of potentials were introduced to the shell model to represent the attractive force and to reproduce the experimental observations. The most realistic approximation is a Woods-Saxon potential as compared to other potentials such as the harmonic oscillator and the square well. The Woods-Saxon potential form is written as:

$$V_0(r) = \frac{V_0}{1 + \text{Exp}[(r - R)/a]} \quad (1.1)$$

where  $R$  is the nuclear radius defined by  $r_0 A^{1/3}$  ( $r_0 = 1.27$  fm and  $A =$  mass),  $V_0$  is the well depth the nuclear potential, and  $a$  is the nuclear skin thickness or diffuseness. However, the model with this potential was unable to reproduce the magic numbers above 20. The spin-orbital potential ( $V_{so}(r)$ ), given in Equation 1.2, was introduced in the model to improve the prediction for heavy nuclei.

$$V_{so}(r) = \frac{0.44V_0}{r_0^2 r} \frac{d}{dr} \left[ \frac{1}{1 + \text{Exp}[(r - R)/a]} \right] \quad (1.2)$$

The higher magic numbers were reproduced with this modification. Therefore, the spin-orbit force is thought to be responsible for the major shell closures that occur near the valley of stability. The shell structure generated by the Woods-Saxon potential with a spin-orbit force up to nucleon number 50 is shown in Fig. 1.2. The magic numbers are those that correspond to filling groups of orbitals that lie below large gaps in energy. The ordering of the single-particle states generated by the Wood-Saxon potential (left) and spin orbit forces (right) is shown in the figure. The maximum number of nucleons in each single-particle state  $(2j+1)$  is given on the right side of

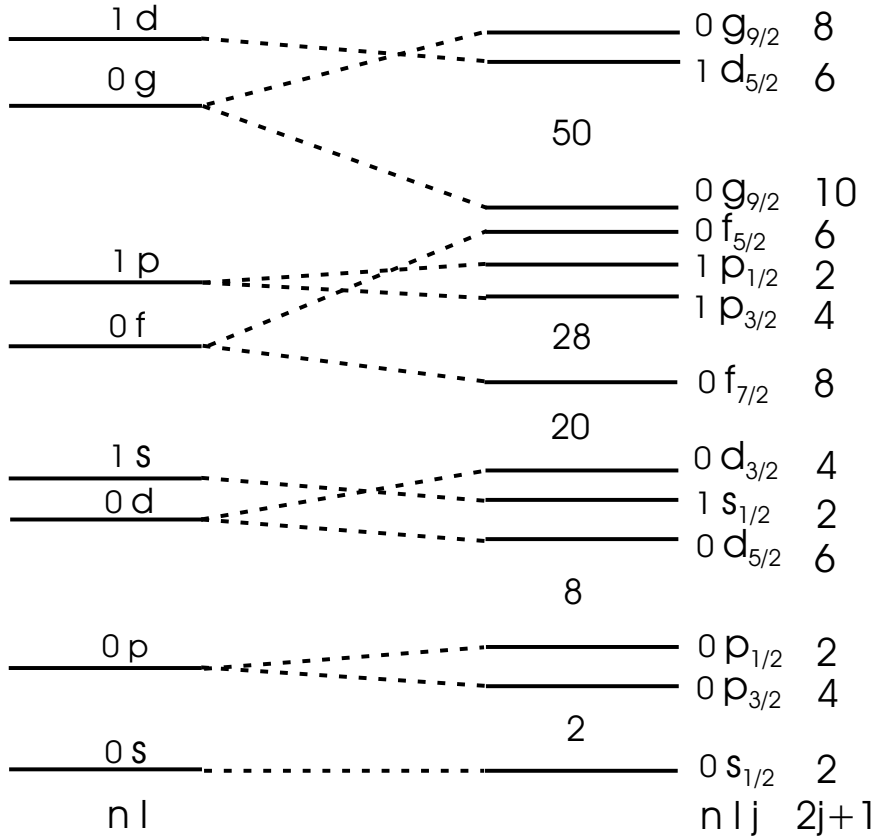


Figure 1.2: Schematic diagram of the single-particle states with two potential models, shown up to the  $1d_{5/2}$  state. On the left is shown the single particle spectrum produced by the Woods-Saxon potential. On the right is the single particle spectrum obtained by the Woods-Saxon potential with a spin orbit force.  $n$  is the principle quantum number. The angular momentum  $l$  is represented by the labels s, p, d, f, g and h corresponding to  $l = 0, 1, 2, 3, 4, 5$ , respectively. The projection of the total spin of the shell is  $j$ . The magic numbers are indicated between each major shell gap [1].

the figure.

At present the model space is so large that shell model calculations start with the assumption that the low-lying nucleons make an inert core and the higher lying nucleons (valence nucleons) can be treated separately from the core. In general, the experimental single-particle energies and binding energies are used in the calculations, if they are available. For example, USD (Universal  $sd$ ) calculations are available for light nuclei based on a least square fit of 447 binding energies in the mass region  $A=16-40$  and under the constraints coming from the excited states in  $^{18-20}\text{O}$  [3]. This version of the shell model is very successful in reproducing and predicting the

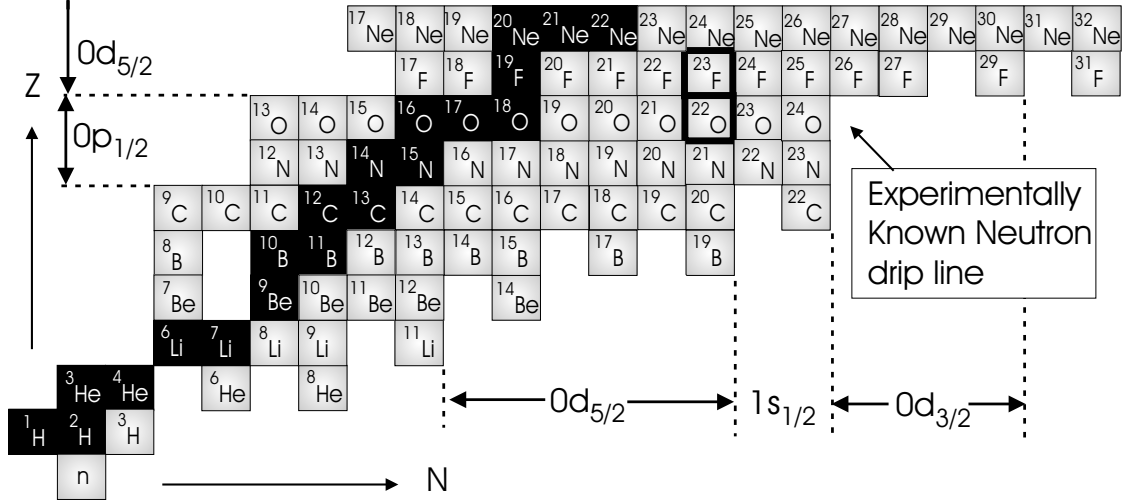


Figure 1.3: Part of the chart of nuclides, the experimentally known neutron drip line up to fluorine isotopes is shown. The solid black squares represent beta stable nuclei. The last proton and neutron arrangements in the shell orbitals are shown for oxygen and fluorine isotopes. The isotopes ( $^{22}\text{O}$  and  $^{23}\text{F}$ ) that present study focused on are highlighted.

nuclear properties close to the valley of stability [2]. The nuclei near to the drip lines have been described reasonably well using the USD shell model but the extrapolation of the single particle energies using mean field models are generally not good. It is important to observe the trends of single-particle energies from the experimentally known nuclei and in particular to study nuclei near to the drip line. One of the primary objectives of the exotic beam facilities is to study the structure of nuclei close to the neutron-rich drip line. Recent experiments with exotic nuclei near and at the drip line have indicated changes of the nuclear structure, for example, the significant change in the neutron drip line location at the region of O and F isotopes [4], the disappearance of traditional magic numbers and appearance of new magic numbers when approaching to the drip line [5, 6], and halo structures near the neutron drip line [7]. These features will be discussed in the following sections as an outline of the motivation for the present work.

## 1.1 Location of The Neutron Drip Line

The existence of a given nucleus is one of the interesting phenomena to be explored in nuclear physics. The recent development of rare isotope beams (RIB) allows searching for the existence of a nucleus when increasing proton or neutron number and access to the more exotic drip line isotopes. A number of experiments have shown that the neutron drip line has been reached for all isotopes up to oxygen as shown in Fig. 1.3. The last oxygen nucleus is  $^{24}\text{O}$ , which was first observed by Artukh et al. [8]. Several theoretical groups had predicted that the next particle stable oxygen isotopes would be  $^{26}\text{O}$  and  $^{28}\text{O}$ , and the latter would be a doubly magic nucleus [9]. However, the particle instability of  $^{25,26}\text{O}$ , has been clearly shown by two experiments [10, 11] and more recent attempt to observe  $^{26}\text{O}$  by Schiller et al. [12] also failed. Although the stability of  $^{28}\text{O}$  as a closed shell nucleus has been predicted by several mass models, Sakurai et al. [13] have shown the particle instability of  $^{28}\text{O}$  from an extrapolation of the experimental yields of nuclei in this region. The heaviest known fluorine isotope,  $^{31}\text{F}$ , was observed for the first time by the same group. Thus, it has been confirmed that the heaviest nitrogen and oxygen isotopes are  $^{23}\text{N}$  and  $^{24}\text{O}$  with the same neutron number  $N = 16$ , while the heaviest isotope of fluorine has been extended up to  $^{31}\text{F}$  with  $N = 22$ . It is interesting to note that at least six additional neutrons can be bound by adding one proton and moving from oxygen to fluorine. There are theoretical attempts to explain the drip line locations for O and F isotopes by modification to the mean field in this region [4, 14]. The theory predicts that the empty  $d_{3/2}$  orbit in  $^{24}\text{O}$  is unbound to neutron decay and neutrons in the nuclei beyond  $^{24}\text{O}$  would have to occupy this unbound orbit. This makes isotopes beyond  $^{24}\text{O}$  unstable and leads to the drip line location at  $^{24}\text{O}$ . A very recent experiment at NSCL measured the neutron-unbound first excited state at 4.2 MeV in  $^{24}\text{O}$  supporting the predictions [15]. The theoretical explanation for the large range of fluorine isotopes is that the monopole interaction between the occupied  $d_{5/2}$  proton and  $d_{3/2}$  neutron

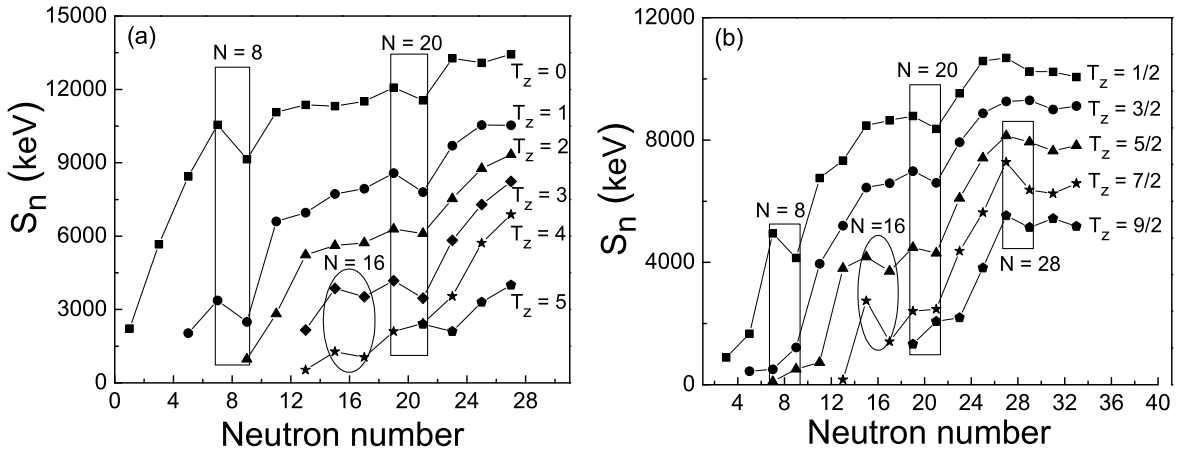


Figure 1.4: Single neutron separation energies for nuclides of different isospin. a)  $S_n$  for odd-odd nuclides. b)  $S_n$  for even-odd nuclides. Isospin values are given at the right side of each graph. The traditional magic numbers are shown by boxes and the appearance of a new magic number at  $N = 16$  is highlighted by ovals.

orbitals lowers the  $d_{3/2}$  single-particle energy, allowing extra binding energy for heavy fluorine isotopes [16]. Thus, the extension of the drip line location to  $^{31}\text{F}$  indicates that one of the  $pf$ -shell orbits must be bound. Measurements that determine the  $pf$ -shell orbits are specially important to understand the large number of the fluorine isotopes.

## 1.2 Disappearance of Traditional Magic Numbers

It has been predicted that an increasing thickness of the nuclear skin will reduce the strength of the spin-orbit force when approaching the drip line [17]. The attenuation of the spin-orbit force may result in the modification or collapse of the shell closures in the region near to the drip line since the positions of the single-particle levels depends on the spin-orbit force.

One of the best ways to identify a magic number is the presence of a discontinuity in the single and two nucleon separation energies as a function of mass number [6]. Fig.1.4 shows the neutron number dependence of the experimental  $S_n$  values for nuclei

with odd neutron number ( $N$ ) and even proton number ( $Z$ ), and odd  $N$  and odd  $Z$  at constant isospin projection values. The isospin values are shown at the sides of graphs. Note that the isospin value for a set of nuclei increases toward the neutron drip line. The signature of a magic number in the neutron separation energies is a sudden decrease of  $S_n$  with the increase of neutron number by one at constant isospin value. These drops at the traditional magic numbers are highlighted with boxes in the figure. At low isospin values, such as  $T = 0, 1/2$  and  $1$ , it is clearly seen that there are discontinuities at  $N = 8$  and  $20$  emphasizing the existence of traditional magic numbers near to the valley of beta stability. When approaching the drip line with high isospin values ( $T_z$ ) of  $3/2, 2, 5/2, 3$  and  $7/2$ , the signature of the magic number  $N = 20$  still survives while the magic number at  $N = 8$  appears to vanish for those nuclei with  $3/2$  and  $5/2$  isospin values. The nuclei with isospin values at  $T_z = 4, 9/2$  and  $5$  show the disappearance of the signature of the magic number  $N = 20$ . In addition, a discontinuity becomes significant at  $N = 16$  with nuclei having  $T_z = 5/2, 3, 7/2$  and  $4$ , and may signal new magic number at  $N = 16$ . Shell model calculations also provide supporting evidence about changing shell structure closer to the neutron drip line [3]. However, the understanding of the nuclear structure evolution near the neutron drip line is poor due to the limited access to those nuclei.

### 1.3 Shell closure at $N = 14$ and $N = 16$

Another experimental signature of magic numbers is the presence of a relatively high energy for the first  $2^+$  excited state of an even-even nucleus [20]. Fig. 1.5 shows both the experimental and calculated excitation energies of the lowest  $2^+$  states of the neutron-rich even-even oxygen isotopes. The first  $2^+$  state of  $^{22}\text{O}$  has an energy of 3199 keV [21], which is 1562 keV higher than that of  $^{20}\text{O}$ . The shell model results suggest that the  $N = 14$  shell closure results from the filling of the  $d_{5/2}$  neutron shell in  $^{22}\text{O}$ . In addition, the presence of a small electromagnetic matrix element  $[B(E2)]$  value

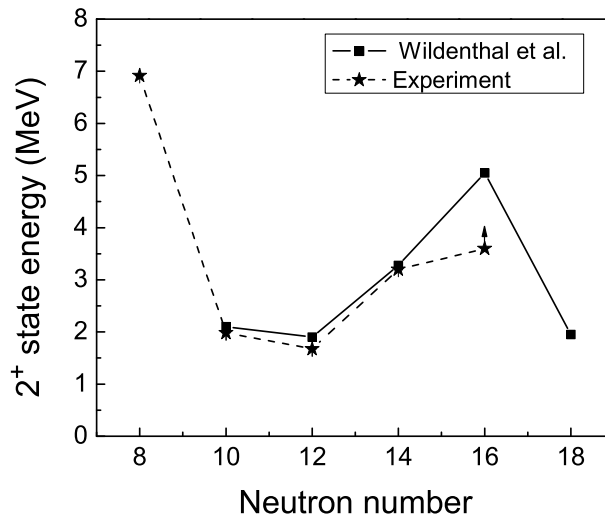


Figure 1.5: The excitation energy of the  $2^+$  states of even-even oxygen isotopes. The calculated and experimental  $2^+$  state energies are taken from Refs. [18] and [19], respectively.

of  $21(8) e^2\text{fm}^4$ ] for the  $2^+$  state in  $^{22}\text{O}$  from an inelastic scattering experiment [22] supports the  $N = 14$  shell closure argument. The same trend in  $B(E2)$  values is also seen with the sd-shell model calculations with USD interactions [20](see Fig. 1.5). The recent observation of the  $2^+$  state in  $^{22}\text{O}$  using elastic and inelastic scattering found that the ratio of neutron to proton contributions to the transition in this state was  $2.5(10)$ , which is similar to  $N/Z$  value of 1.75, indicating that the excitation is carried by both protons and neutrons in the valance shells [23, 24]. In contrast, the excitation of the  $2^+$  state in  $^{20}\text{O}$  was found to be carried mostly by neutrons [25]. The indication that both particle types contribute to the transition in  $^{22}\text{O}$  demonstrate the shell closure at  $N = 14$  is just as good as the  $Z = 8$  shell closure. With this experimental and theoretical evidence,  $^{22}\text{O}$  appears to be a doubly magic nucleus.

$^{24}\text{O}$  has been predicted by shell model calculations to be another doubly magic nucleus with a high  $2^+$  state energy as shown in Fig. 1.5. The absence of any gamma-ray decay from the excited states in  $^{24}\text{O}$  in a recent GANIL experiment [21] indicates that the first excited state may be neutron unbound. A lower limit of  $3.6(3)$  MeV

(neutron separation energy) was set for the  $2^+$  state. Fig. 1.5 shows the lower limit for the first excited state in  $^{24}\text{O}$ . A recent experiment carried at NSCL has found positive evidence for a 4.2(3) MeV excitation energy of the first excited state in  $^{24}\text{O}$ , which is neutron unbound [15]. These results with theoretical predictions strongly support the idea of a shell closure at  $N = 16$  for the neutron-rich nuclei.

## 1.4 Halo structures near neutron drip line

When approaching the neutron drip line the neutron separation energy decreases gradually and the bound states come close to the continuum region of the nuclear potential. The combination of the short range of the nuclear force and the low neutron separation energy allows in some cases the special structure called a nuclear halo, where valence nucleons behave very differently from the core nucleons. The very weakly bound nucleons can tunnel into the classically forbidden region outside the range of the nuclear force and form a “halo” [7]. The halo nuclei have a large radius compared to the stable nuclei (the root-mean-square(RMS) radius does not follow the  $R=R_0A^{1/3}$  law). One and two-neutron halo nuclei have been found in the neutron-rich light nuclei, namely,  $^{11}\text{Be}$ ,  $^{11}\text{Li}$ ,  $^{14}\text{Be}$  and  $^{19}\text{C}$  [7]. In addition to the characteristic properties of the halo structure, one and two beta-delayed neutron decays were observed for two of these nuclei. For example, one and two neutron modes of the  $^{14}\text{Be}$  beta decay are known to be 81(4)% and 5(2)%, respectively [26]. Cluster-core model [27] calculations predict many halo nuclei in the light region including  $^{22}\text{N}$  and  $^{23}\text{O}$  [28]. In particular,  $^{23}\text{O}$  has been suggested as a likely candidate for a one-neutron halo nucleus with the experimental observation of a narrow momentum distribution for the  $^{22}\text{O}$  fragments produced from the one-neutron removal reaction from  $^{23}\text{O}$  and the large reaction cross-section of  $^{23}\text{O}$  [29].

The halo structure may have a direct influence on the beta decay in several ways. One way is that the overlap between parent ground state and low-lying states in the

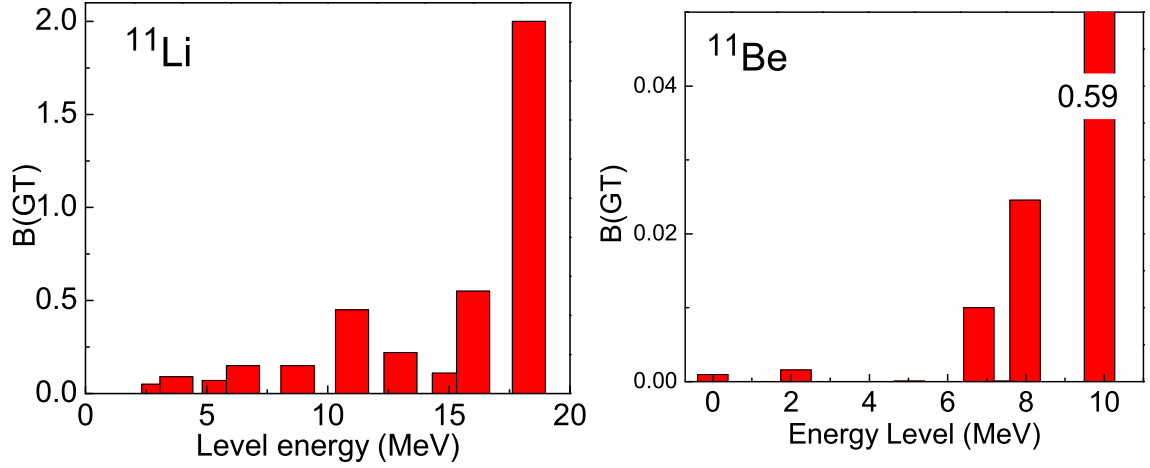


Figure 1.6: Beta decay of the halo nuclei  $^{11}\text{Li}$  and  $^{11}\text{Be}$ . The experimental Gamow-Teller strength distribution of  $^{11}\text{Li}$  (left) and  $^{11}\text{Be}$  (right) as a function of excitation energy of the daughter [19, 30, 7].

daughter may be reduced to due the large spatial extension of halo states resulting a general reduction of beta decay strength to such states [17]. Another possibility is the valence neutron may decay separately from the core neutrons producing an unusual pattern for the beta decay. The characteristic feature that has been observed in beta decay of a halo nucleus is the transitions with large Gamow-Teller strength [B(GT)] go to states at high excitation energy in the daughter nucleus. Figure 1.6 shows the experimental B(GT) distribution as a function of the excitation energy for beta decay of  $^{11}\text{Li}$  and  $^{11}\text{Be}$  that are known as two and one neutron halo nuclei, respectively. In both cases, the relatively high B(GT) values are associated with high excitation energies. Therefore, beta decay provides a signature of halo structure. The determination of beta decay to the high excitation energies in a nucleus near the drip line is much harder, since branching ratios would be lower and more decay channels are open due to high Q-value. Thus, one can expect the complicated beta decay with nuclei near to neutron drip line.

## 1.5 Motivation

Very little spectroscopic information on neutron-rich light nuclei is available at present to investigate nuclear structure in the region. Systematic studies using beta-delayed neutron spectroscopy on nuclei, especially in the region of oxygen isotopes, have been carried out during the past [31, 32, 33, 34]. The present study is focused mainly on the nuclear structure of the isotopes  $^{22}\text{O}$  and  $^{23}\text{F}$ , produced via beta decay of  $^{22}\text{N}$  and  $^{23}\text{O}$ . The isotopes are located in the chart of nuclides between the  $N = 8$  and  $N = 20$  closed neutron shells. The position in the chart of nuclides including the surrounding isotopes can be seen in Fig. 1.3. The last two protons in oxygen fill the  $p_{1/2}$  orbit forming the  $Z = 8$  shell closure. In  $^{22}\text{O}$ , the last six neutrons fill the  $d_{5/2}$  orbital reaching the maximum occupancy of the orbital. In the case of  $^{23}\text{F}$ , the 14 neutrons occupy the same orbitals as  $^{22}\text{O}$  and the last single proton goes into a  $d_{5/2}$  orbital. The current knowledge of the nuclear structure of  $^{22}\text{O}$  and  $^{23}\text{F}$  are presented in following sections.

### 1.5.1 Knowledge of the Structure of $^{22}\text{O}$ and $^{22}\text{N}$

The study of the single particle structure of  $^{22}\text{O}$  particularly has been important for the understanding of nuclear structure near to the neutron drip line. The gamma decay for  $^{22}\text{O}$  was reported by F. Azaiez. [36] and Belleguic et al. [37] from an in-beam fragmentation experiment at GANIL. They reported gamma-ray transitions at 1370 and 3200 keV and assigned the 3200 keV gamma-ray to the  $2_1^+ \rightarrow 0_{gs}^+$  transition in  $^{22}\text{O}$ , and the other to the decay from a 4510 keV excited state to the  $2^+$  state. The excitation energy for the first  $2^+$  state was confirmed by a radioactive beam coulomb excitation experiment at the NSCL, where a  $2_1^+$  state was measured to be 3.17 MeV [22]. The gamma-ray at 1370 keV was not observed in this latter work. The energy level scheme for  $^{22}\text{O}$  with positive parity states has been extended by Stanoiu et al. recently using single and double step fragment reactions at GANIL [21]. This

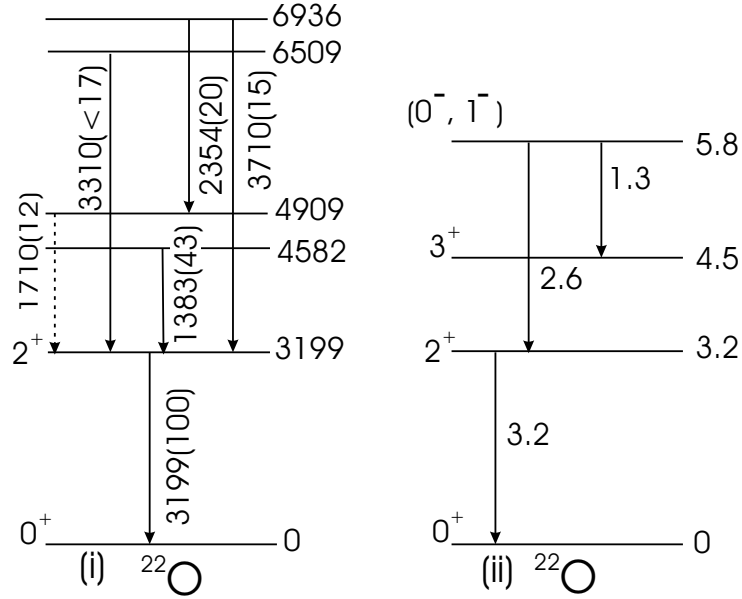


Figure 1.7: Level scheme of  $^{22}\text{O}$ . (left) The level scheme was deduced from an in-beam gamma-ray spectroscopic experiment [21]. The transition energies are in keV with their relative intensities in parentheses. The 3199 keV energy level is assigned to be  $2^+$ . (right) The level scheme was produced using a knockout reaction by Cortina-Gil et al. [35]

work reported five excited states with their gamma-ray decays and relative intensities, as given in Fig. 1.7. The spins and parities of states were not assigned except for the first excited state. A one-neutron knockout experiment carried at GSI to measure the longitudinal momentum distribution for neutron-rich oxygen isotopes reported a spectrum with three gamma-rays at 1.3, 2.6 and 3.2 MeV from the deexcitation of  $^{22}\text{O}$  [35] (see Fig. 1.7). The first two gamma-ray energies were assigned to the negative parity state  $(0^-, 1^-)$  at 5.8 MeV, which deexcited into  $2^+$  and  $3^+$  states at 3.2 and 4.5 MeV, respectively. This negative parity assignment was based on arguments by Brown et al. from calculations of the spectroscopic factors in the  $^{12}\text{C}(^{23}\text{O}, ^{22}\text{O})\text{X}$  reaction [14]. The first excited and ground states of  $^{22}\text{O}$  have also been studied using the  $^{22}\text{O}(p, p')$  reaction and reconfirmed the  $N = 14$  magicity in  $^{22}\text{O}$  by probing the proton and neutron contribution to the  $2^+$  excitation [23] mentioned above.

The negative parity states in  $^{22}\text{O}$  are not experimentally known except for the only tentative state at 5.8 MeV. The beta decay of  $^{22}\text{N}$  should provide information

predominately on the negative parity states in  $^{22}\text{O}$ , which are favored by the beta decay of the negative parity ground state of  $^{22}\text{N}$ . The ground state of  $^{22}\text{N}$  is experimentally unknown at present but simple shell model calculations predict the ground state as  $0^-$ . The beta decay of  $^{22}\text{N}$  leads mainly to the mass(A) = 22 decay chain with the subsequent decays of  $^{22}\text{O}$  and  $^{22}\text{F}$ . The A = 21 decay chain with decays of  $^{21}\text{O}$  and  $^{21}\text{F}$  is expected to be observed as a result of beta-delayed neutron decay. The  $^{22}\text{N}$  beta decay series is shown in Fig. 1.8, where black squares represent beta stable isotopes.

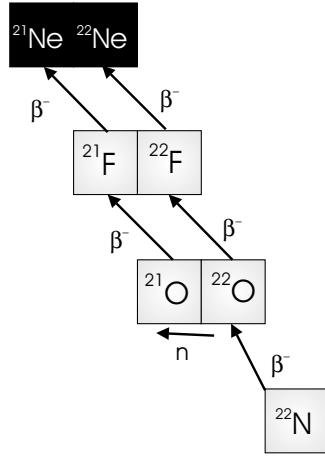


Figure 1.8: Beta decay chain of  $^{23}\text{O}$ . Beta decay chains produced from the beta decay to the bound states and from the beta-delayed neutron decay are shown with the stable isotopes in black squares.

Mueller et al. [38] reported the beta decay half-life of  $^{22}\text{N}$  to be  $24_{-6}^{+7}$  ms and Reeder's group reported a shorter half-life of 14(6) ms [39], that is just within the error bars. The total neutron emission probability ( $P_n$ ) was found to be 35(5)% for  $^{22}\text{N}$  beta decay [38,39]. A more recent beta decay study done by Yoneda et al. reported the beta-delayed neutron multiplicities for  $^{22}\text{N}$  to be  $P_{1n} = 41(+12-10)\%$  and  $P_{2n} < 13\%$  with a half-life of 16.5(+8.5-4.8) ms [40]. Although the half-lives and ( $P_n$ ) values agree within errors, the uncertainties are large. There is no spectroscopic information for the beta decay of  $^{22}\text{N}$ .

## 1.5.2 Knowledge on the Structure of $^{23}\text{F}$ and $^{23}\text{O}$

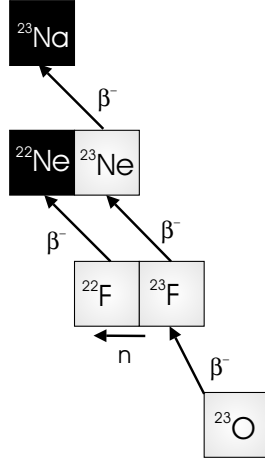


Figure 1.9: Beta decay chain of  $^{23}\text{O}$ . Beta decay chains produced from the beta decay to the bound states and from the beta-delayed neutron decay are shown with the stable isotopes in black squares.

$^{23}\text{F}$  should have the structure of a single proton outside the proposed doubly magic  $^{22}\text{O}$ . The ground state of  $^{23}\text{O}$  is known to be  $1/2^+$  [35, 41] so that one can expect beta feeding predominately to excited states in  $^{23}\text{F}$  as direct feeding to the ground state of  $^{23}\text{F}$ , which was confirmed to be  $5/2^+$  by Sauvan et al. and Cortina-Gil et al. [41, 35], would be a first forbidden decay. The beta decay chain of  $^{23}\text{O}$ , shown in Fig. 1.9, includes the decays of  $^{23}\text{F}$  and  $^{23}\text{Ne}$  from beta decay to the bound states, and decay of  $^{22}\text{F}$  from beta-delayed neutron decay. All beta decay paths shown in the figure are expected to be observed with the  $^{23}\text{O}$  beta decay experiment.

Mueller et al. reported a total neutron emission probability ( $P_n$ ) of 31(7)% for beta decay of  $^{23}\text{O}$  with a half-life of 82(37) ms, which is the only measurement for the half-life [38]. An upper limit for the  $P_n$  value was published later by Reeder et al. as  $< 29\%$  [39]. There are several theoretical estimations for the half-life of  $^{23}\text{O}$ , which range from 12.8 to 196 ms [38, 44, 45]. The predicted  $P_n$  values for  $^{23}\text{O}$  beta decay were close to 30% and agreed with the experimental values except for the value of 2% predicted by Wildenthal et al. [18]. The energy levels in  $^{23}\text{F}$ , the beta decay daughter of  $^{23}\text{O}$ , have been measured using the heavy-ion transfer reaction

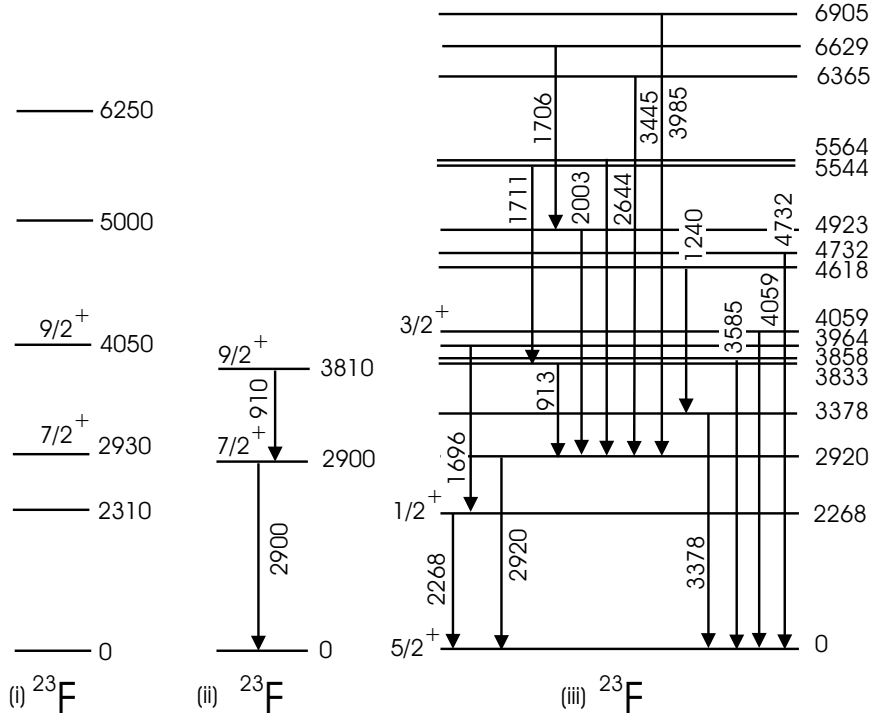


Figure 1.10: Experimentally known energy levels in  $^{23}\text{F}$ . (left) The level scheme was produced using a heavy-ion transfer reaction by Orr et al [42]. The gamma-ray decay schemes produced using a fragmentation reaction by Belleguic et al. [37] (middle) and using a proton transfer reactions by Michimasa et al. [43] (right) are shown. The energies are given in keV .

$^{22}\text{Ne}(^{18}\text{O}, ^{17}\text{F})^{23}\text{F}$  by Orr et al. [42]. Six levels at 2.31, 2.93, 4.05, 5.00, 6.25, and 8.18 MeV were observed in  $^{23}\text{F}$ . The ground state, the second and third excited states were assigned spins and parities of  $5/2^+$ ,  $7/2^+$  and  $9/2^+$ , respectively, based on shell model calculations. Two excited states at 3810 and 2900 keV that deexcite by a cascade of gamma-rays at 910 and 2900 keV in  $^{23}\text{F}$  have been reported by Belleguic et al. [37] in  $^{36}\text{S}$  fragmentation reactions. These two states were assigned as  $7/2^+$  and  $9/2^+$ , respectively, by comparison to the shell model. Michimasa et al. recently reported studies of the excited states in  $^{23}\text{F}$  using three kinds of reactions, namely  $^4\text{He}(^{22}\text{O}, ^{23}\text{F}\gamma)$ ,  $^4\text{He}(^{23}\text{F}, ^{23}\text{F}\gamma)$  and  $^4\text{He}(^{24}\text{F}, ^{23}\text{F}\gamma)$  [43]. The resulting gamma-ray decay scheme, shown in Fig. 1.10, was established up to 7 MeV based on gamma-gamma coincidence measurements. In the most recent work, the 2268 and 4059 keV energy levels were assigned to spins and parities of  $1/2^+$  and  $3/2^+$ , respectively. The

spin assignment for the state at 4.05 MeV is inconsistent with Orr et al. work. The spin and parity for other states are unknown and no negative parity states in  $^{23}\text{F}$  have been observed at present.

## 1.6 Present Work

The present work focused on the beta-delayed neutrons and gamma-rays from  $^{22}\text{N}$  and  $^{23}\text{O}$  to establish the neutron unbound and bound energy states in  $^{22}\text{O}$  and  $^{23}\text{F}$ , respectively, at particular interest were the negative parity states in doubly magic  $^{22}\text{O}$  nucleus. These states were not experimentally known but were measured in this work due to the highly selective beta decay. The beta decay schemes for  $^{22}\text{N}$  and  $^{23}\text{O}$  have been established and compared with shell model calculations. The accuracy and precision of the half-lives and total neutron emission probabilities were significantly improved.

This dissertation presents the study of the beta decay of  $^{22}\text{N}$  and  $^{23}\text{O}$  using neutron and gamma-ray spectroscopic arrays. The theory of beta decay is discussed in Chapter 2 explaining the decay modes. The beta decay selection rules are introduced to assign spins and parities of the observed states. The isotope production technique and the details of instrumentation utilized to monitor beta particles, neutrons and gamma-ray events are presented in Chapter 3 including the electronic setup and calibrations. The details of the analysis of neutron time-of-flight system are described including the peak shape and energy. In Chapter 4, data analysis and results are reported with a detailed discussion of the assignments of transitions and decay schemes. Finally, The experimental beta decay properties of desired isotopes are compared with shell model calculations in Chapter 5.

# Chapter 2

## Overview of Beta Decay

The primary objective of this study was to measure the neutron unbound and bound states of nuclei near the neutron drip line to understand the structural changes of those nuclei. The techniques to obtain information on states in neutron-rich nuclei involve Coulomb excitation, direct and transfer reactions, inelastic scattering and beta decay. In the present study, beta decay was chosen as the method to populate states in neutron-rich light nuclei. In light nuclei, the level density is low and high efficiency neutron and gamma-ray detectors with good energy resolution can provide information on energy level structure of nuclei. The decay of these nuclei is also characterized by large Q-values opening a large energy window to populate a significant number of states. As one approaches the neutron drip line, the neutron separation energies decrease while the Q-values are large so that a large fraction of the beta-decay strength can lead to neutron unbound states. Measuring the beta decay, and delayed neutrons and gamma-rays from a nuclide thus provides information on the levels, which are populated during the beta decay. This also allows one to calculate transition strengths, known as the branching ratios, for the particular transitions. The transition energy coupled with the transition strength can be utilized to calculate the  $\log(ft)$  value on the beta decay branch. This in turn can be used as criteria for assigning the properties (spin and parity) of the energy levels of the daughter nuclide.

The following sections will include discussions on the theories of beta decay, including beta-delayed neutron and gamma-ray decay and calculations of Gamow-Teller transition strength.

## 2.1 Theory of Beta Decay

Beta decay is a radioactive decay process in which a neutron is converted into a proton or vice versa by emitting an fast electron (beta particle) or a positron, respectively. There are three kinds of beta decay process, which are given below:

$$\beta^- \text{ decay : } \frac{A}{Z}X_N \rightarrow \frac{A}{Z+1}Y_{N-1}^+ + \beta^- + \bar{\nu} + Q_\beta \quad (2.1)$$

$$\beta^+ \text{ decay : } \frac{A}{Z}X_N \rightarrow \frac{A}{Z-1}Y_{N+1}^- + \beta^+ + \nu + Q_\beta \quad (2.2)$$

$$\text{Electron Capture : } \frac{A}{Z}X_N \rightarrow \frac{A}{Z-1}Y_{N+1} + \nu + Q_\beta \quad (2.3)$$

where A, Z, N,  $\beta^-$ ,  $\beta^+$ ,  $\bar{\nu}$  and  $\nu$  are mass, proton and neutron numbers of parent(X) or daughter(Y) nuclei, fast electron, positron, anti-neutrino, and neutrino, respectively.  $Q_\beta$  value is the energy released from the decay process, which is calculated from the mass difference between parent and daughter nuclei. In  $\beta^-$  decay, a neutron is converted into a proton while emitting an electron and anti-neutrino. When the binding energy of the daughter nucleus is 1.022 Mev ( $2m_e c^2$ ) higher than the parent nucleus,  $\beta^+$  decay may occur by converting a proton into a neutron with an emission of a positron and a neutrino. If their energy condition is not satisfied by the system, the alternative process of electron capture can occur. Here an atomic electron is captured to convert a proton into a neutron.

Fermi related the beta decay transition rate ( $\lambda_{fi}$ ) to the interaction ( $V_{fi}$ ) that causes the transition between the initial and the final states, and the density ( $\rho(E_f)$ ) of final energy states. The assumption of the theory is that the interaction which causes beta decay is a weak perturbation relative to the strong nuclear and coulomb

forces in the nucleus [5,10]. This relationship for the transition rate can be formulated as:

$$\lambda_{fi} = \frac{2\pi}{\hbar} |\langle V_{fi} \rangle|^2 \rho(E_f) \quad (2.4)$$

For the beta decay, the interaction matrix element ( $\langle V_{fi} \rangle$ ) in Equation 2.4 can be written as;

$$\langle V_{fi} \rangle = g \langle \psi_f \phi_e \phi_v | \hat{O} | \psi_i \rangle \quad (2.5)$$

where  $\psi_i$  and  $\psi_f$  are the wavefunctions for the initial and final nuclear states, respectively;  $\phi_e$  and  $\phi_v$  are the wavefunctions of the emitted electron and neutrino, respectively; and  $g$  is a parameter which describes the strength of the interaction (coupling constant). The symmetry properties of beta decay observed in experiments require that the operator  $\hat{O}$  in Equation 2.5 be a linear combination of a polar vector and an axial vector operator.

The emitted electron and neutrino are taken to be free-particle plane wave functions:

$$\phi_e(\vec{r}) = C e^{i\vec{p}\cdot\vec{r}/\hbar} \quad (2.6)$$

$$\phi_v(\vec{r}) = C e^{i\vec{q}\cdot\vec{r}/\hbar} \quad (2.7)$$

where  $C$  is a normalization constant and  $p$  and  $q$  are their momenta. A series of approximations can be made using the expansions of Equations 2.6 and 2.7 based on the selection rules of decay to simplify the interaction matrix element. Finally, the interaction matrix element can be written as Equation 2.8, where  $\langle M_{fi} \rangle$  is the nuclear matrix element for allowed beta decay.

$$\langle V_{fi} \rangle = g \langle \psi_f | \hat{O} | \psi_i \rangle = g \langle M_{fi} \rangle \quad (2.8)$$

The total beta decay rate  $\lambda$  is obtained by integrating over the density of states

in the range of energies available to the electron and neutrino, and is given in the Equation 2.9.

$$\lambda = \frac{g^2 m_e^5 c^4 |\langle M_{fi} \rangle|^2}{2\pi^2 \hbar^7} \int_0^{p_{max}} F(Z', p) p^2 (Q - T_e)^2 dp \quad (2.9)$$

where  $p$ ,  $m_e$ ,  $T_e$  and  $c$  are the momentum, mass and energy of the emitted electron, and speed of light, respectively.  $Q$  is the energy released in the beta decay which is shared between electron and neutrino, and  $F(Z', p)$  is the Fermi function which describes the shapes of the emitted  $\beta^-$  and  $\beta^+$  spectra. This function includes the effects of the Coulomb field of the nucleus on the electron.

The types of beta decay can be classified by the angular momentum carried away by the electron and neutrino. The most prevalent are those for  $\Delta l=0$ , which are referred to as “allowed” beta decays. The emitted particles have spin of 1/2 and therefore, they can be in a singlet ( $S = 0$ ) or triplet ( $S = 1$ ) state. The two types of allowed beta decay are called Fermi (F) decay (singlet) and Gamow Teller (GT) decay (triplet). The spin relationship for the angular momenta of the nuclei for both decays can be written as,

$$J_i = J_f + l \quad \text{for Fermi decay} \quad (2.10)$$

$$J_i = J_f + l + 1 \quad \text{for Gamow - Teller decay} \quad (2.11)$$

where  $J_i$  is initial nuclear spin,  $J_f$  is final nuclear spin and  $l$  is the orbital angular momentum carried by the electron and the neutrino. The term  $g^2 |\langle M_{fi} \rangle|^2$  in Equation 2.9 can be replaced with two nuclear matrix elements and two coupling constants corresponding to the two types of beta decay types:

$$g^2 |\langle M_{fi} \rangle|^2 \rightarrow g_V^2 |\langle M_{fi} F \rangle|^2 + g_A^2 |\langle M_{fi} (GT) \rangle|^2 \quad (2.12)$$

The weak interaction polar vector (V) and axial vector (A) coupling constants for the decay of neutron into proton are denoted by  $g_V$  and  $g_A$  respectively. The nuclear

matrix elements in the Equation 2.12,  $M_{fi}(F)$  and  $M_{fi}(GT)$ , can be defined with Fermi and Gamow-Teller beta decay operators as follows

$$\langle M_{fi}(F) \rangle = \langle \psi_f | \Sigma \hat{t}_k | \psi_i \rangle \quad (2.13)$$

$$\langle M_{fi}(GT) \rangle = \langle \psi_f | \Sigma \hat{\sigma}_k \hat{t}_k | \psi_i \rangle \quad (2.14)$$

where  $\hat{t}$  is an operator which transforms a proton into a neutron and  $\hat{\sigma}$  is the usual Pauli spin operator, the sum being taken over all nucleons in the nucleus. By replacing Equation 2.9 with two nuclear matrix elements, the total beta decay rate can be written as

$$\lambda = \frac{m_e^5 c^4 f}{2\pi^2 \hbar^7} \{g_V^2 |\langle M_{fi}(F) \rangle|^2 + g_A^2 |\langle M_{fi}(GT) \rangle|^2\} \quad (2.15)$$

where  $f$  is the phase space integral

$$f = \int_0^{p^{max}} F(Z', p) p^2 (Q - T_e)^2 dp \quad (2.16)$$

The Fermi integral  $f$  can be numerically determined by using the atomic number of daughter ( $Z'$ ) and beta decay energy ( $Q$ ) for particular beta decay.

### 2.1.1 Selection Rules

Beta decay is a process which happens only between selective states governed by the set of rules known as the selection rules. These rules are deduced based on the principle that the total angular momentum and the parity of the angular momentum must be conserved during the transition between the initial and final states in the beta decay process. The selection rules for Fermi and Gamow-Teller beta decay will be discussed below.

The beta particle and neutrino emitted in both beta decay process have zero orbital angular momentums under the allowed beta decay classification. In Fermi

decay, the spins of the beta particle and neutrino are anti-parallel ( $S=0$ ), and the total change in nuclear spin ( $\Delta J$ ) between the initial and final states in the transition must be zero ( $\Delta J = 0$ ). In Gamow-Teller decay, the beta particle and neutrino are emitted with their parallel spins ( $S=1$ ) resulting the total change in nuclear spin zero or one ( $\Delta J = 0$  or  $1$ ). The parity change of the system is defined by  $\Delta\pi = (-1)^l$ , where  $\pi$  is the parity of the system. Since  $l = 0$  for the allowed beta decay, the parity of the initial and final states should be same for both types of decays.

Table 2.1: Classification of beta decay

Beta decay type	Fermi $\Delta J$	Gamow-Teller $\Delta J$	$\Delta\pi$	$\log(ft)$
Supperallowed	0	0	No	2.9 -3.7
Allowed	0	0,1	No	4.4 - 6.0
First Forbidden	0,1	0,1,2	Yes	6 - 10
Second Forbidden	1,2	1,2,3	No	10 - 13
Third Forbidden	2,3	2,3,4	Yes	>15

When the beta particle and neutrino are emitted with  $l \neq 0$ , the decay by an allowed transition cannot occur. However, this kind of decay does occur, but with a much smaller probability compare to the allowed decay. Such decays are known as “forbidden” decays and are classified in order of forbiddenness based on  $l$  value. For example, the first and second forbidden beta decays result from the beta particle and neutrino emitted with  $l = 1$  and  $2$ , respectively. The classification of beta decay transitions based on spin and parities are summerized in Table 2.1. The transitions can also be categorized with their experimental  $\log(ft)$  values, shown in Table 2.1, where  $f$  is Fermi integral and  $t$  is a partial half-life of the transition (see section 2.4). If the  $\log(ft)$  value is in the range 2.9 to 3.7 for a beta transition it is generally called as superallowed beta decay.

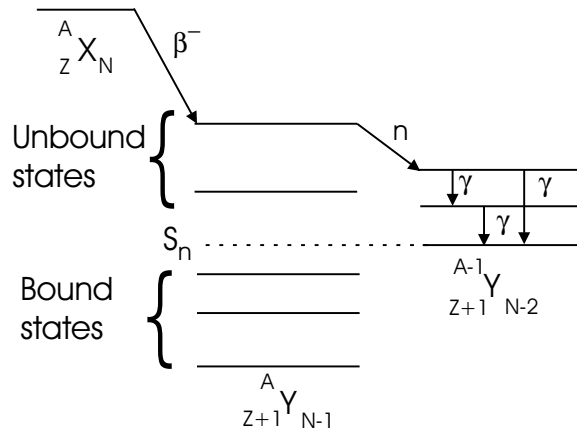


Figure 2.1: Schematic diagram of Beta-delayed Neutron Decay

## 2.2 Beta-delayed Neutron Decay

In particular, the  $\beta^-$  decay of nuclei far from the valley of beta stability can have a high tendency to populate neutron unbound states that are above the neutron separation energy, since they are characterized by large  $Q$  value and low neutron separation energy. Neutron emission subsequent to the beta decay is called beta-delayed neutron decay. This decay process finally populates the states in the neighboring daughter ( ${}^{A-1}Y$ ), which has a mass number less than one mass unit of the parent. Fig. 2.1 shows beta-delayed neutron decay from parent ( ${}^A X$ ) to the single beta-delayed neutron daughter ( ${}^{A-1}Y$ ). In this case, the parent  ${}^A X$  beta decays to one of the unbound state in the daughter  ${}^A Y$  and emits a neutron subsequently to feed into the excited state in the neutron daughter  ${}^{A-1}Y$ , which undergoes gamma-ray decay. The neutron will have a kinetic energy that is characteristic of the energy difference between the initial and final states. Spectroscopic measurements of the neutrons can therefore provide information on the structure of the two nuclei.

## 2.3 Gamma-ray decay

Neutron bound states, except for the ground state, in the daughter populated by the beta decay deexcite through an emission of electromagnetic radiation, called gamma-

ray decay. This decay process can only occur when the nucleus is in the excited state. The excess energy in the nucleus is released as photons (gamma-rays) to relax to the relatively low energy state or ground state. Based on the conservation of angular momentum, a photon connecting two nuclear states should carry at least one unit of angular momentum and must satisfy the following relationship

$$|(I_i - I_f)| \leq l \leq (I_i + I_f) \quad (2.17)$$

where  $I_i$  and  $I_f$  are angular momenta of initial and final states and  $l$  is the multipolarity, which is defined as the number of angular momentum units carried by the photon. Note that  $l = 0$  is a forbidden transition for photon emission.

The change in the distribution of matter and charge during the gamma-ray decay leads to a change in the electric and magnetic properties of the nucleus. Therefore, gamma-ray transitions can be categorized based on the effective electric and magnetic character. The multipolarity of the photon depends on both the angular momentum and the type of transition, which can be represented by following relationships;

$$\Delta\pi(El) = (-1)^l \quad (2.18)$$

$$\Delta\pi(Ml) = (-1)^{l+1} \quad (2.19)$$

where  $\Delta\pi$  is the parity change between states and, E, M and  $l$  represent the electric and magnetic characters and the multipolarity of the transition.

## 2.4 Gamow-Teller Transition strength

The operator associated with Fermi decay is proportional to the isospin raising and lowering operators ( $\hat{t}$  in equations 2.13, 2.14). As such, Fermi decay can only connect analog states and it provides a test of isospin conservation in the nucleus. The operator

associated with Gamow-Teller decay also contains the nucleon spin operator ( $\hat{\sigma}$  in equation 2.14). In general, this decay goes to many final states as it produces a mixture of relative spins, and provides a sensitive test of shell-model configuration mixing in the nucleus using the beta decay transition strength.

The total decay rate for a given initial state can also be written by summing the partial beta decay rates ( $\lambda_{fi}$ ) over the total number of final states:

$$\lambda = \sum_f \lambda_{fi} \quad (2.20)$$

with the branching fraction ( $b_{fi}$ ) to a specific final state:

$$b_{fi} = \frac{\lambda_{fi}}{\lambda} \quad (2.21)$$

The partial half-life for a particular final state will be denoted by:

$$t_{1/2} = \frac{T_{1/2}}{b_{fi}} \quad (2.22)$$

where the beta decay half-life is  $T_{1/2}$ . The partial half-life for a particular decay with the calculated Fermi integral ( $f$ ) is used to obtain  $\log(ft)$  that can be used to characterize the transition type. The relationship between Fermi integral and the partial half-life is given by:

$$ft_{1/2} = \frac{K}{|\langle M_{fi}^F \rangle|^2 + (g_A^2/g_V^2)|\langle M_{fi}^{(GT)} \rangle|^2} \quad (2.23)$$

where  $K$  is defined as:

$$K = \frac{2\pi^3 \hbar^7 \ln(2)}{m_e^5 c^4 g_V} \quad (2.24)$$

Equation 2.25 is derived by the partial beta decay rate defined in the same form of Equation 2.15 and introduced the partial half-life relationship to the partial beta decay rate. For  $0^+ \rightarrow 0^+$  nuclear transitions,  $\langle M_{fi}^{(GT)} \rangle = 0$  and for a transition

between (isospin)  $T = 1$  analogue states  $\langle M_{fi}(F) \rangle = 2$ . Equation 2.25 is then reduced to  $K = 2ft_{1/2}$ . By fitting the experimental partial half-lives and  $Q$  values for  $0^+ \rightarrow 0^+$  transitions of 20 well known nuclei, the “K” constant was found to be 6170(4) s [18, 46]. The Gamow-Teller beta decay strength  $[B(GT)]$  for a particular transition is defined as  $|\langle M_{fi}(GT) \rangle|^2$ . For the  $\beta^-$  decay of the neutron-rich nuclei, the relationship between Gamow-Teller strength and the partial half-life of the final state is expressed as:

$$ft_{1/2} = \frac{6170 \text{ s}}{(g_A/g_V)^2 B(GT)} \quad (2.25)$$

where  $g_A/g_V$  is known to be 1.259(4) [47].

This equation will be used in Chapters 4 and 5 to calculate Gamow-Teller strengths for the desired beta decay transitions along with Fermi integrals ( $f$ ) calculated from an empirical equation given in Ref. [18]:

$$\log(f) = 4.0\log E + 0.78 + 0.02Z - 0.005(Z - 1)\log E \quad (2.26)$$

where  $E$  (keV) and  $Z$  are the  $\beta^-$  decay end point energy for the transition and the atomic number of the daughter nuclide, respectively.

## 2.5 Application

The measurement of beta decay with delayed neutrons and gamma-rays allows the study of the beta decay strengths to excited states and ground state of the daughter nuclide. In the case of  $^{22}\text{N}$  allowed beta decay, the negative parity states in  $^{22}\text{O}$  are expected to be populated as the ground state of  $^{22}\text{N}$  is predicted to be  $0^-$  [48] and the ground state of the even-even  $^{22}\text{O}$  was found to be  $0^+$  [41]. This means the feeding to the ground state of  $^{22}\text{O}$  could be less probable as it is a forbidden transition. The ground state of  $^{23}\text{O}$  is known to be  $1/2^+$  [41] so that one can expect

beta feeding predominately to excited states as direct feeding to the ground state of  $^{23}\text{F}$  with known  $J^\pi = 5/2^+$  would be at least a first forbidden decay. Beta-delayed neutron time-of-flight spectroscopy has been utilized to observe neutron unbound states. Particle bound states in the daughter nuclide had observed by employing traditional gamma-ray spectroscopy. The beta decay events has been measured with a plastic scintillation detector and time stamped to generate a decay curve, from which the half-life was deduced. The branching ratios were determined based on the observed neutron and gamma-ray intensities considering the feeding into the state and deexciting from the state. The partial half-lives and decay energies to a state can be used to deduce  $\log(ft)$  values, which in turn can be used to infer spin-parities of final states. The beta decay schemes for  $^{22}\text{N}$  and  $^{23}\text{O}$  have been established with information on decay energies, spins and parities, and branching ratios states. The next chapter will explain the technical details of the measurements including the isotope production, beta, gamma-ray and neutron detection.

# Chapter 3

## Experimental Setup

Radioactive beams of  $^{22}\text{N}$  and  $^{23}\text{O}$  were produced using projectile fragmentation at the National Superconducting Cyclotron Laboratory's (NSCL) Coupled Cyclotron Facility (CCF). The interesting isotopes were stopped in an implantation detector to observe beta-delayed neutron and gamma-ray decay events. A neutron spectroscopic array with sixteen scintillation detectors and a gamma-ray array with eight segmented germanium detectors were employed to measure the neutron and photon energies, respectively. Radioactive beams of  $^{16}\text{C}$  and  $^{17}\text{N}$  were also produced and used to calibrate the neutron detectors. The production of fragments, and the experimental techniques and equipment used to measure the beta decay of  $^{22}\text{N}$  and  $^{23}\text{O}$  are described in the following sections.

### 3.1 Fragment Production

The stable isotope,  $^{48}\text{Ca}$ , was accelerated to produce the radioactive beams of interest.  $^{48}\text{Ca}$  vapor was introduced into a Electron Cyclotron Resonance (ECR) ion source and  $^{48}\text{Ca}^{8+}$  ions were extracted and guided to the K500 cyclotron. These ions were accelerated to 12.3 MeV/A, and then injected into the K1200 cyclotron. A thin carbon foil was used prior to acceleration in the K1200 cyclotron to strip

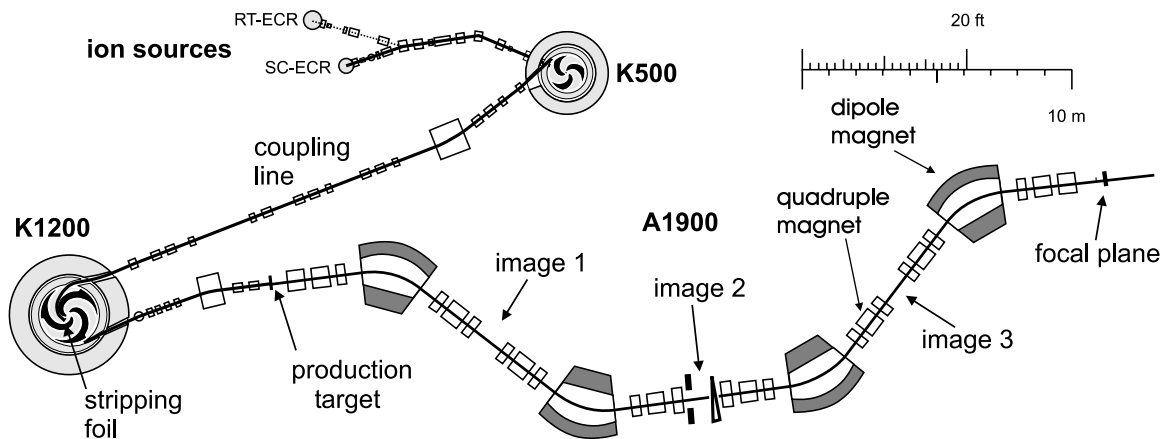


Figure 3.1: Schematic diagram of the NSCL Coupled Cyclotron Facility and the A1900 fragment separator.

the remaining electrons to produce  $^{48}\text{Ca}^{20+}$  ions. The ions were accelerated to 140 MeV/A within the K1200. The full-energy ions were extracted and guided onto a 846 mg/cm<sup>2</sup> beryllium target at the object position of the A1900 spectrometer as shown in Figure 3.1. The thickness of the target was selected to maximize the production rate of the  $^{22}\text{N}$  isotope based on the LISE code [49]. The fragmentation reactions occurred inside the target, usually producing nuclides lighter than  $^{48}\text{Ca}$ . The mechanism of fragment production can be explained as the removal of nucleons from the projectile by collisions with target atoms. The projectile-like fragments are emitted with approximately the same velocity as the primary beam after de-excitation via emitting neutrons charged particles and gamma-rays [50]. The produced fragments were directed to the A1900 fragment separator [51] where the desired isotope was separated from the projectile like fragment cocktail beam by means of two magnetic bends along with a 825 mg/cm<sup>2</sup> aluminum wedge placed at the Image 2 position of the separator. The A1900 separator consists of four superconducting dipole magnets and eight superconducting quadrupole triplet magnets as shown in Figure 3.1. The dipoles separate ions based on their momentum to charge ratio.

The isotopic separation was obtained in three stages. An initial selection of fragments with a specific momentum to charge ratio (mv/q) was accomplished using the first two dipole magnets of the A1900 separator. Fragments with a desired mv/q

Table 3.1: A1900 magnet settings and beam purity at the A1900 focal plane.

Secondary beam	$^{22}\text{N}$	$^{23}\text{O}$	$^{16}\text{C}$	$^{17}\text{N}$
$B_{\rho_{1,2}}$ (Tm)	4.9477	4.4967	4.1730	3.7205
$B_{\rho_{3,4}}$ (Tm)	4.6970	4.2100	3.9660	3.4635
Beam purity (%)	58.6	16.8	72.7	75.1
Major impurities	$^{25}\text{F}$ , $^{24}\text{O}$ , $^{21}\text{N}$	$^{26}\text{Ne}$ , $^{24}\text{F}$	$^{17}\text{N}$	$^{18}\text{O}$

passed through the dipoles while others with the incorrect  $mv/q$  were filtered out and deposited in a catcher bar located inside magnets. The forward moving fragments with the same  $mv/q$  needed to be further separated to produce a beam with a higher concentration of the desired isotope. This was achieved by introducing a  $Z$  (proton number) dependent momentum shift using a wedge degrader. The fragments passing through the wedge lose energy based on the  $Z$  and velocity ( $V$ ) as given in the following equation:

$$-\frac{dE}{dX} \propto \frac{Z^2}{V^2} \propto \frac{AZ^2}{E} \quad (3.1)$$

where  $E$  and  $X$  are energy and thickness, respectively. In the present case, the atomic charge  $Q$  is equal to the nuclear charge  $Z$ . The fragment of interest was finally selected from the fragments that exited the wedge using the last two dipole magnets of the A1900 separator. The magnetic rigidities ( $B\rho$ ) of all magnets for the produced beams are given in Table 3.1 with the beam purities and major impurities.

Each nuclide in the secondary beam was individually identified at the experimental end station by energy-loss and time-of-flight measurements. The secondary beam, optimized for the desired nuclide, was sent to the N4 vault where the desired nuclide was stopped in an implantation detector. A schematic diagram of the experimental setup at the end station, is shown in Figure 3.2. The setup consisted of the implantation detector system, the neutron spectroscopic array and detectors from the MSU segmented germanium array (SeGA). Each component of the setup will be explained in the following sections.

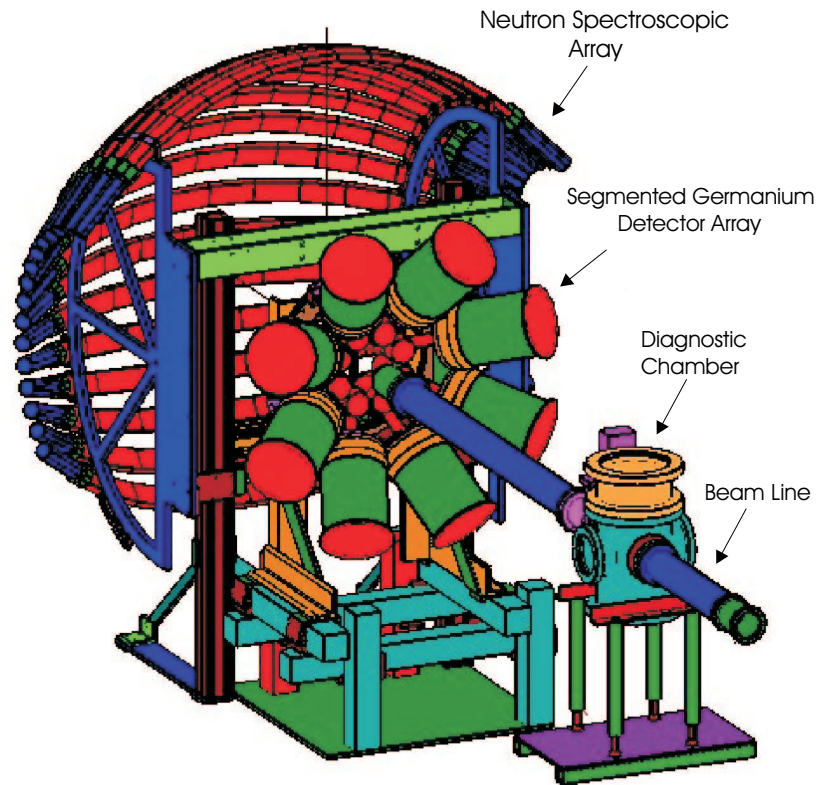


Figure 3.2: Experimental setup with the neutron and SeGA array

### 3.2 Implantation Detector System

Secondary beam exited vacuum beam line in N4 vault passed into air through a kapton window, which had thickness of 0.03 mm. The beam then traveled 135 cm in air before reaching the implantation detector system. The implantation detector system consisted of four components: a dE detector, an Al degrader, an implantation detector, and a veto detector. The secondary beam passed through the dE detector, which was a silicon surface barrier detector with thickness  $200\ \mu\text{m}$  and area  $300\ \text{mm}^2$ , for isotope identification. The energy loss in the dE detector in combination with a time-of-flight measurement (TOF) derived from the cyclotron resonance frequency and the time signal of the dE detector allowed particles to be identified on an event-by-event basis. The isotopes of interest were stopped in the implantation detector in order to observe the beta decay. The incoming ions were properly ranged by introducing an aluminum degrader before the implantation detector, as shown in Figure 3.3. The

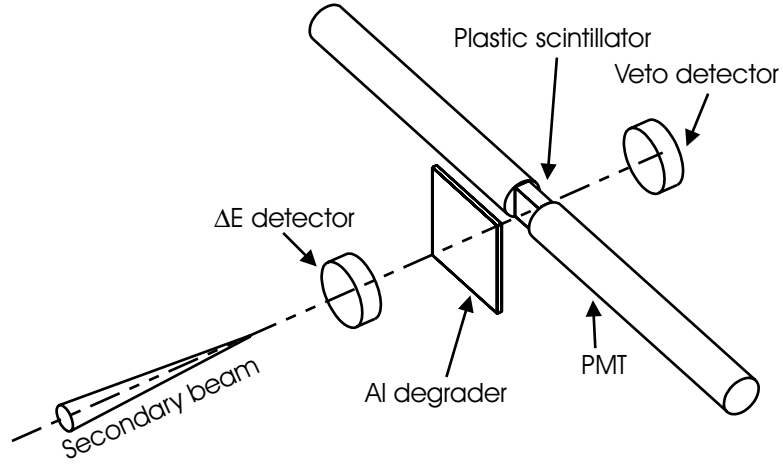


Figure 3.3: Implantation detector system.

Table 3.2: Calculated and actual degrader thickness used to stop the ions.

Secondary beam	SRIM predicted thickness (mm)	Actual thickness (mm)
$^{16}\text{C}$	15.845	15.506
$^{17}\text{N}$	10.100	9.704
$^{22}\text{N}$	16.052	15.704
$^{23}\text{O}$	11.536	11.412

thickness of the degrader was adjusted so that the isotope of interest was fully stopped in the implantation detector. The initial estimates of the degrader thickness were made based on results from the program SRIM (Stopping and Range of Ions in Matter) [52] by modeling the all material through the beam path. The thickness of all objects in the beam path, material types and isotope with its energy were used as input parameters to the program. Table 3.2 shows the calculated and actual degrader thickness used to stop the secondary beams. The second silicon surface barrier detector, served as a veto detector. It was placed after the implantation detector to detect ions that were not stopped in the implantation detector. The veto detector specifications were similar to the first detector. The implantation detector was a thin plastic scintillator (3 mm thick) attached to two Photo-Multiplier Tubes (PMT) and located at the center of an array of neutron detectors.

Data were collected in a beam-on/beam-off cycle mode. The beam was pulsed on for a fixed time period to collect nuclides in the implantation detector and the

Table 3.3: Beam-on/off periods for each beam, the literature half-life and the production rate of the important isotope in the beam.

Nuclide	Beam-on/off	Half-life	Production rate (pps)
$^{16}\text{C}$	2.5 s	0.747(8) s	27
$^{17}\text{N}$	6.5 s	4.173(4) s	86
$^{22}\text{N}$	100 mm	24(5) ms	0.3
$^{23}\text{O}$	300 ms	82(37) ms	7

beta decay was monitored during the subsequent beam-off period. The time intervals were controlled by VME Dual Timer. The beam was interrupted during the beam-off period by applying a TTL logical gate signal to the r.f.-transmitter on one of the dees of the K500 cyclotron. At the beginning of each beam-off period, a real-time clock was started and beta decay events were time stamped to produce decay curves. The time signal for the time stamp was deduced from two ortect RC014 Real Time Clock modules operated in parallel with conjunction to CAEN V993 VME Dual Timer (see Figure 3.4). The length of time for beam-on/beam-off cycle was decided based on the literature half-lives of the implanted nuclides. Table 3.3 shows the beam on and off time intervals for each radioactive beam along with their reported half-lives and isotope production rates. The beam-on and beam-off periods was set to approximately three times the literature half-life of the isotope of interest.

### 3.2.1 Data Acquisition System

The Data Acquisition System (DAQ) consisted of separate components for the dE, veto and implantation detectors, the neutron spectroscopic array and detectors from SeGA. The system consisted of various NIM, CAMAC and VME models. Data were recorded by mapping the CAMAC addresses into the VME domain controlled by a DAQ computer. The neutron spectroscopic array and the SeGA array electronics used VME and CAMAC modules for digital readout, which will be described in subsections related to each device. NIM modules handled the trigger logic with the implantation detector system electronics. A complete diagram of the electronics setup

of the implantation detector, including the trigger logic, is shown in Figure 3.4. The output from each PMT of the implantation detector was split into two signals to obtain energy and time information. One of the signals was fed to a CAMAC Charge-to-Digital Converter (QDC) in order to store the energy, while the other was used as input to a Tennelec TC-455 Constant Fraction Discriminator (CFD), which was used to produce a logic signal. The QDC used was a CAEN Model V792 QDC, which has 32 channels that integrate the charge deposited within a selected time window. The time signal from the CFD was recorded by a TDC upon the start signal from the master gate and also used in trigger logic. The time signals from the two PMTs of the implantation detector were logically ANDed to discriminate against false events from the implantation detector or noise in PMTs. The AND signal of was split using a Fan-In and Fan-Out (FIFO) to produce two trigger signals, which were again ANDed separately with beam-on and beam-off gate signals produced by the VME dual timer model. The two ANDed logic signals were again Ored to produce the master gate signal. Then, the master gate signal was ANDed with a computer NOT-busy signal to define the master live signal, which triggered the computer acquisition to read all detectors.

The software used to read the data from the electronic modules was based on the NSCL-DAQ readout program [53]. This program was responsible for responding to master triggers and reading out the output information from the digitizers. Separate sub-modules were included to the main readout code to read the digitizers of the neutron array and SEGA. The data events were analyzed to produce the graphical histograms and to apply other analytical operations using the standard SpecTcl software [53].

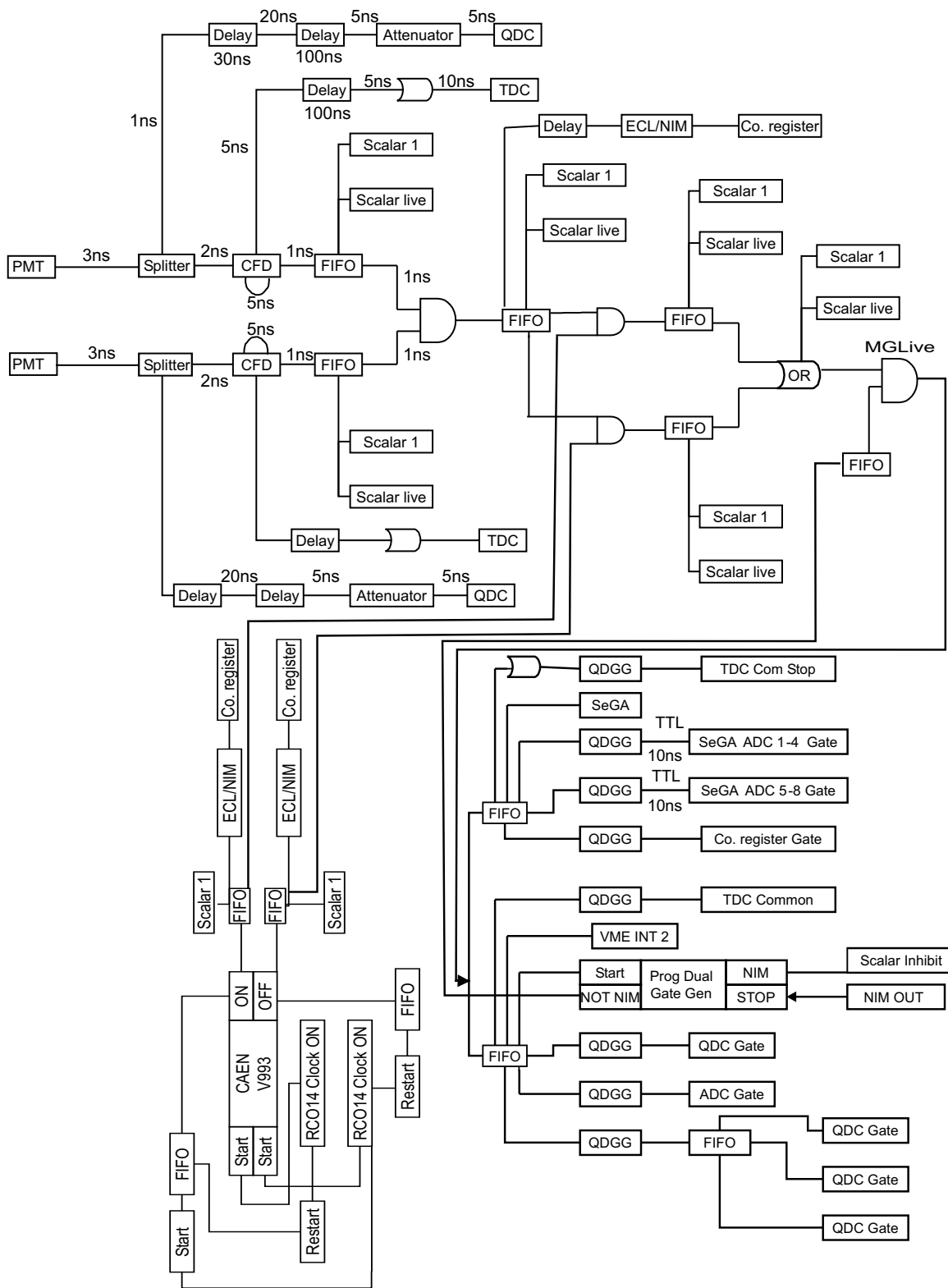


Figure 3.4: Electronic setup for the implantation detector. CFD- Constant Fraction Discriminator, QCD- Charge-to-Digital Converter, FIFO- Fan In and Fan Out, and PMT- Photo-Multiplier Tube.

### 3.3 Neutron Spectroscopic Array

Beta-delayed neutron decay is associated with the neutron unbound states in the beta decay daughter. The energies of the delayed neutrons are measured by means of time-of-flight measurements using a neutron spectroscopic array. The detailed specifications, energy and efficiency calibrations of the neutron spectroscopic array will be discussed in following sub-sections.

#### 3.3.1 Detail of the Neutron Spectroscopic Array

The neutron array consisted of sixteen BC412 plastic scintillator bars with the approximate dimensions of  $157 \text{ cm} \times 7.3 \text{ cm} \times 2.54 \text{ cm}$  bent in an arc with a one-meter radius. The detector design provides an equal flight path for all neutrons leaving a central implantation detector. This array covered a total solid angle of 1.9 steradians and had a surface area of array approximately  $800 \text{ cm}^2$ . Detailed information about the neutron array is available in Ref. [54]. The neutron bars were supported by an aluminum frame work so the implantation detector was at the center of each neutron bar. The time signal originating from the detection of a beta decay event in the implantation detector served as the start of a neutron time-of-flight measurement for any of the neutron detectors. Each scintillator bar had a photomultiplier tube (PMT) at each end of the bar to detect photons resulting from neutron interactions with the scintillator material. The mean time signal from two PMTs attached to any of the neutron bars served as the stop for the neutron time-of-flight (TOF) measurements. The time difference between the start and stop signals was used to deduce the neutron time-of-flight and thus determine the neutron energy.

The schematic electronic diagram for the neutron spectroscopic array is given in Figure 3.5. The delayed output signal of each PMT was split into two signals. One signal was processed through a QDC, which was gated by the master gate trigger to get energy information. The other signal was used to produce the time signal.

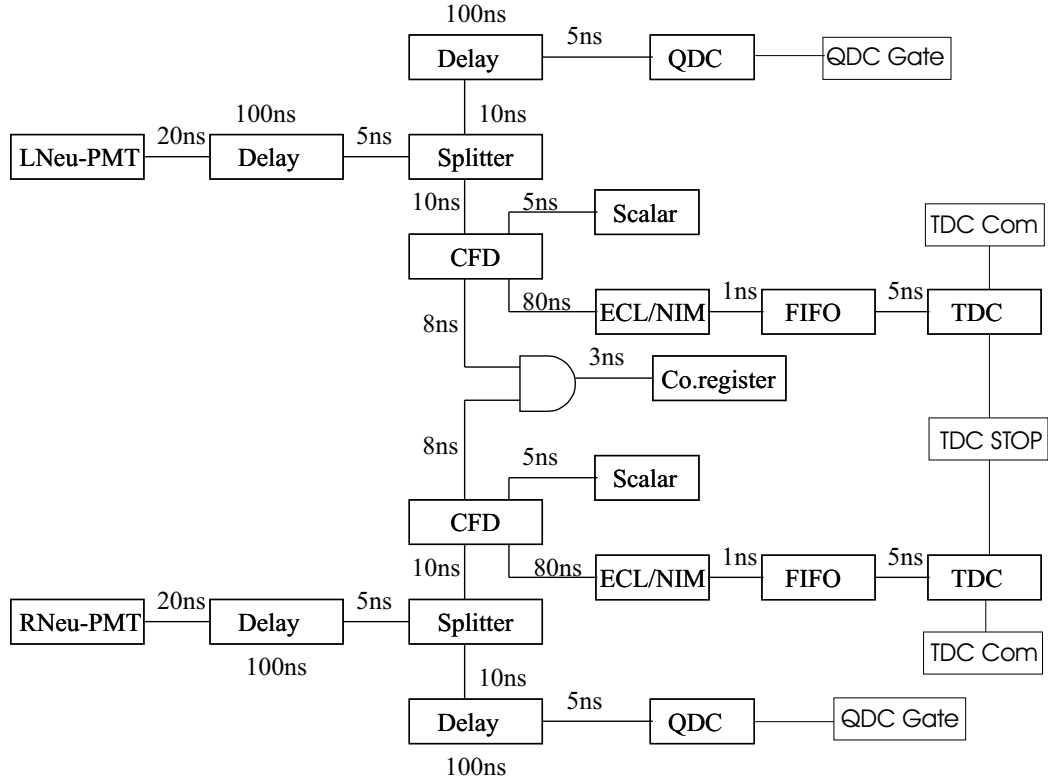


Figure 3.5: Schematic electronic diagram for the neutron bar array. CFD- Constant Fraction Discriminator, QCD- Charge-to-Digital Converter, FIFO- Fan In and Fan Out, and PMT -Photo Multiplier Tube.

As shown in Figure 3.5, both logic signals processed by the CFDs of both sides of neutron detector were ANDed to eliminate false neutron events or noise from PMTs. The ANDed signals from each neutron detector were combined with an OR logical gate and used in trigger logic. The second logic signal from CFD was processed by the TDC, which was stopped by the master gate.

The neutron spectroscopic array was used to determine the energy of beta-delayed neutrons as well as the number of neutrons emitted with the beta decay of desired isotope. Therefore, the individual neutron detectors required calibration for both neutron energy and efficiency. The neutron energy calibration was achieved by calibrating the TDC modules for their time slopes using a time calibrator (ORTEC 462). The offsets were determined from the known beta-delayed neutrons of  $^{16}\text{C}$  and  $^{17}\text{N}$  taken as calibration beams. Data from beta-delayed neutron decay of these isotopes were

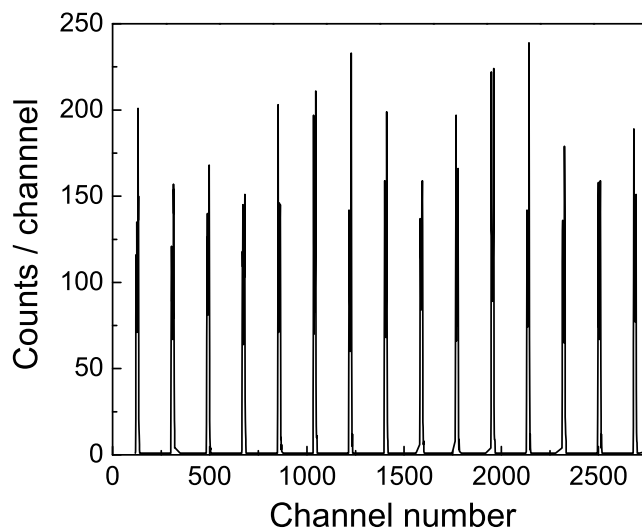


Figure 3.6: The time calibration spectrum for the neutron detector.

also used for the efficiency calibration. A Monte Carlo simulation was used to extend the efficiency calibration to higher energy. The detail procedure of both calibrations will be discussed in the following sections separately.

### 3.3.2 Neutron Energy Calibration

#### Time calibration of the neutron array

The determination of neutron energy using the time-of-flight technique requires two type of calibrations: calibration of the TDC response of each PMT channel, and the on-line calibration, which includes the intrinsic response of neutron detectors. The time-slope calibration of each TDC channel was obtained using an ORTEC-462 time calibrator. The start signal of the calibrator was split and used as an input to the CFDs of the implantation detector. The stop signal to the calibrator was also split and used as an input to the CFDs of each PMT of a neutron detector. The period and range of the time calibrator were set to 10 ns and 32  $\mu$ s, respectively. The TDC time response for each PMT channel was measured independently. An example spectrum

Table 3.4: Time calibration results for neutron detectors.

Neutron detector	Time slope (ns/channel)	Beta-prompt peak centroid	Neutron detector	Time slope (ns/channel)	Beta-prompt peak centroid
01	25.296	45.4	09	25.232	45.4
02	25.256	45.4	10	25.267	45.5
03	25.271	45.5	11	25.253	45.6
04	25.259	45.4	12	25.286	45.5
05	25.262	45.5	13	25.289	45.5
06	25.239	45.5	14	25.312	45.6
07	25.262	45.5	15	25.273	45.5
08	25.260	45.6	16	25.185	45.5

from one of the neutron detector calibration is given in Figure 3.6. Calibration plots (time vs. channel number) were made to derive the time slope (ns/channel) for each neutron bar, and the results are given in Table 3.4.

The time slopes were used in the SpecTcl code as parameters for time calibration. SpecTcl produced a histogram (spectrum) for each neutron detector based on recorded time events and the time calibration. It was essential that the spectra of all neutron detectors were aligned, since the individual spectra were summed to improve statistics. The initial time alignment was done by using a gamma-gamma prompt peak position in  $^{60}\text{Co}$  spectra from each neutron detector. These spectra were obtained by replacing the implantation detector by a  $\text{BaF}_2$  detector with a  $^{60}\text{Co}$  source. The final position adjustments were done using the on-line calibration spectra generated from beta-delayed neutrons of  $^{16}\text{C}$  and  $^{17}\text{N}$ .

The beta-delayed energies and emission probabilities of the neutrons of  $^{16}\text{C}$  and  $^{17}\text{N}$  are known with high precision. The beta decay of  $^{16}\text{C}$  produces neutrons with energies of 810, 1714 and 3290 keV [55, 56] and  $^{17}\text{N}$  beta decays with neutrons of energies 382.8, 1170.9 and 1700.3 keV [55, 57]. In addition, both beta-delayed neutron time-of-flight spectra produced prompt peaks which can be used as calibration points. Secondary beams of  $^{16}\text{C}$  and  $^{17}\text{N}$  were produced in similar manner to that explained in Section 3.1 with appropriate Al degrader thicknesses (see Table 3.2) to implant the desired isotope. The beam-on and -off time intervals were adjusted according to their

half-lives. The details of beam purity, beam-on\off and degrader thicknesses are given in Tables 3.1, 3.2 and 3.3. Beta-gamma prompt peaks of beta-delayed neutron time-of-flight spectra of  $^{16}\text{C}$  and  $^{17}\text{N}$  from all detectors were aligned to channel number 45.5 by introducing offset parameters to the SpecTcl code. The average channel number for beta-gamma prompt peak from both spectra is given in Table 3.4 for each detector.

### On-line neutron energy calibration

On-line time calibration was carried out as follows. The neutron kinetic energy,  $E_n$  can be written in terms of the velocity of the neutron ( $V_n$ ) with no relativistic corrections (since the neutron energy is low enough to treat classically)

$$E_n = \frac{1}{2}mV_n^2. \quad (3.2)$$

This equation can be rearranged as shown in Equation 3.3 by substituting the mass of neutron for m:

$$V_n = \sqrt{\frac{E_n}{5227.083}} \quad (3.3)$$

where  $E_n$  is in MeV and  $V_n$  is in m/ns. The velocity of the neutron can be obtained from the time-of-flight of the neutron and the flight path (d), which is defined as the distance between the point where beta decay occurred and the point where the neutron interacts in the neutron detector. The time-of-flight comes from the peak centroid (c) of the time-of-flight spectrum, which is calibrated. Finally, the reciprocal of velocity of the neutron can be written as:

$$\frac{1}{V_n} = \left[\frac{1}{d}\right]c + \frac{p}{d} \quad (3.4)$$

where p is the TDC offset. According to equation 3.4, the flight path (d) and the TDC offset (p) for the neutron array can be determined under the given experimental conditions based on known neutron energies from beta decay of  $^{16}\text{C}$  and  $^{17}\text{N}$ . In

Table 3.5: Energy calibration results for neutron detectors.

Neutron detector	Energy slope (1/m)	Average distance (m)	Neutron detector	Energy slope (1/m)	Average distance (m)
01	0.9896	1.011	09	0.9926	1.007
02	0.9908	1.009	10	0.9932	1.007
03	0.9857	1.015	11	0.9891	1.011
04	0.9898	1.010	12	0.9881	1.012
05	0.9848	1.015	13	0.9896	1.011
06	0.9870	1.013	14	0.9905	1.010
07	0.9946	1.005	15	0.9805	1.020
08	0.9935	1.007	16	0.9800	1.020

addition, the centroid of the prompt peak was used as part of the neutron energy calibration. The most probable beta energies (KE) were calculated by taking 0.33 of the beta decay energies for a particular decay as:

$$V_{\beta} = C \sqrt{1 - \left( \frac{m_e C^2}{KE + m_e C^2} \right)^2} \quad (3.5)$$

where  $m_e$  is the mass of electron and  $C$  is the speed of light.

The spectra recorded from the beta decay of  $^{16}\text{C}$  and  $^{17}\text{N}$  for each neutron detector were analyzed to determine the peak centroids using the code DAMM (Display, Analysis and Manipulation Mode) developed at Oak Ridge National Lab [58]. The peaks were fitted with asymmetric gaussian peaks and a third order polynomial background. The energy slope for each detector and the flight path ( $d$ ) calculated from their slope are given in Table 3.5.

The calibrated time-of-flight spectra were added after aligning the prompt peak to channel number 45.5 to generate the total spectrum from the neutron array. The total beta-delayed neutron time-of-flight spectra of  $^{16}\text{C}$  and  $^{17}\text{N}$ , shown in Figure 3.7, were fitted using the DAMM code. The peaks were fitted with asymmetric Gaussian peaks and a third order polynomial background. The FWHM values, asymmetric parameters and the coefficients of the background were treated as variables throughout the fitting procedure to establish neutron peak and background shapes. Figure 3.7.(a) shows the

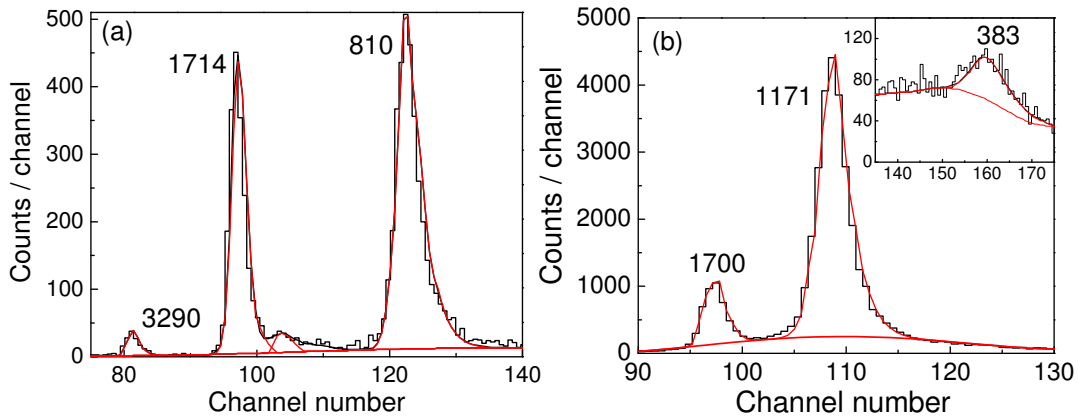


Figure 3.7: Total neutron time-of-flight spectra of  $^{16}\text{C}$  and  $^{17}\text{N}$ . Neutron TOF spectra of (a).  $^{16}\text{C}$  and (b).  $^{17}\text{N}$  with fitted neutron peaks and the background are shown. The energies are marked close to the peak in keV.

Table 3.6: Fitting data from  $^{16}\text{C}$  and  $^{17}\text{N}$  neutron time-of-flight spectra.

$^{16}\text{C}$ data				$^{17}\text{N}$ data			
Peak position	Area	Error	FWHM	Peak position	Area	Error	FWHM
81.5	108	9.2	2.28	97.5	3556	4.4	3.11
97.3	1847	3.6	3.68	108.9	23243	1.6	4.83
122.8	3247	2.8	5.98	160.0	648	11.8	12.0

beta-delayed neutron peaks of  $^{16}\text{C}$  with their energies labeled. The peak without an energy label is unknown from the beta decay of  $^{16}\text{C}$  at present. The fitted beta-delayed neutron time-of-flight spectrum of  $^{17}\text{N}$  is shown in Figure 3.7.(b) with labeled neutron energies. The fitting results for both decays are given in Table 3.6 and were used to establish neutron energy and peak shape calibrations, and to study the background shape of the neutron time-flight spectrum for the neutron spectroscopic array under the present experimental conditions.

The total neutron time-of-flight spectrum was calibrated for energy by establishing a relationship between the neutron peak centroid and the reciprocal of the neutron velocity, as in Equation 3.4. The second column of Table 3.7 shows the literature values for neutron energies from beta decay of  $^{16}\text{C}$  and  $^{17}\text{N}$ . The energies were converted to velocities using Equation 3.3. In addition, the prompt peaks were translated into

Table 3.7:  $^{16}\text{C}$  and  $^{17}\text{N}$  data for the energy calibration of neutron array

Nuclide	Energy (keV)	1/Velocity (ns/m)	Peak position
$^{17}\text{N}$	1700.3(17)	55.4(3)	97.5(19)
	1170.9(8)	66.8(2)	108.9(27)
$^{16}\text{C}$	382.8(9)	116.9(14)	160.0(59)
	3290(30)	39.9(2)	81.5(13)
	1714(5)	55.22(8)	97.3(21)
	810(5)	80.3(2)	122.8(33)
Nuclide	Q-values (keV)	1/Velocity (ns/m)	Peak position
$^{17}\text{N}$	8012	3.380(1)	45.5(3)
$^{16}\text{C}$	8680	3.374(1)	45.4(4)

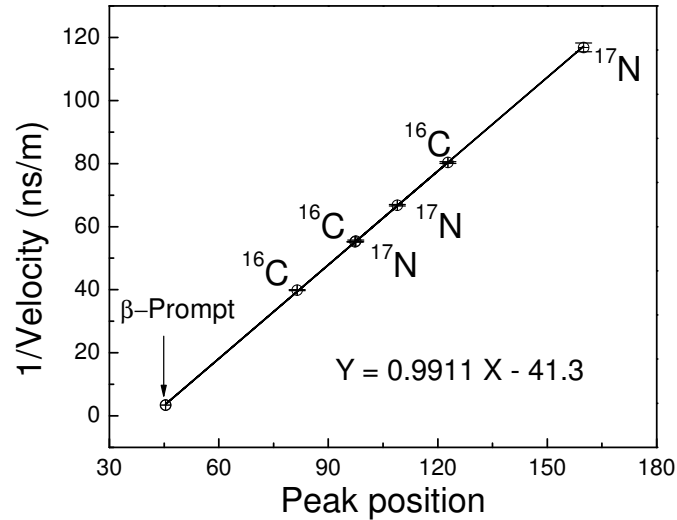


Figure 3.8: Energy calibration of the neutron array using  $^{16}\text{C}$  and  $^{17}\text{N}$  neutron decay.

the reciprocal of velocity by using Equation 3.5 with substituting KE value as 0.33 of Q-value corresponding beta decay. The neutron energy calibration was established by plotting the reciprocal of velocity vs peak position (centroid) as given in Figure 3.8. The energy calibration equation used to derive unknown neutron energies is given in the figure. The error associated with the calculated neutron energy included the fitting uncertainties of the calibration and the error from the peak position.

Table 3.8: Neutron peak shape calibration

Nuclide	Peak position	(Peak position) <sup>1/2</sup>	FWHM	Asymmetric factor
<sup>16</sup> C	81.5	9.03	2.28	0.2
	97.3	9.87	3.68	0.3
	122.8	11.08	5.98	0.5
<sup>17</sup> N	97.5	9.88	3.11	0.3
	108.9	10.44	4.83	0.5
	160.0	12.65	12.0	0.8

### 3.3.3 Neutron Peak Shape and The Background

It is important to establish a standard procedure to define peak shapes and the background when analyzing a neutron time-of-flight spectrum. A study of such was carried out using the <sup>16</sup>C and <sup>17</sup>N beta-delayed neutron time-of-flight spectra. As mention above, neutron peaks were fitted with asymmetric Gaussian functions having exponential tails which extended to higher time-of-flight values. The fit functions are given in Equation 3.6

$$\begin{aligned}
 X < X_0 \quad Y_L &= A * Exp\left(\frac{-(X - X_0)^2}{\sigma^2}\right) \\
 X \geq X_0 \quad Y_R &= A * Exp\left(\frac{-(X - X_0)^2}{\sigma^2(1 + S(X - X_0)\sigma)}\right)
 \end{aligned} \tag{3.6}$$

where  $Y_L$  and  $Y_R$  are left and right parts of the peak with centroid  $X_0$ , and  $\sigma$  and  $S$  are the FWHM and the asymmetric factor of the peak, respectively.

It is reasonable to add an exponential part to the pure Gaussian peak to produce neutron peak shape. The neutron response of the detector has a tail principally due to a delayed light emission in the plastic in the case of low charge deposited in the scintillator bar. The size of the exponential tail was controlled by the FWHM and the asymmetric factor. The calibration spectra were fitted using the DAMM program by minimizing the reduced  $\chi^2$  values, which were found to be in the range of 0.8 - 1.7. Table 3.8 shows the peak centroid, with the corresponding FWHM and asymmetric

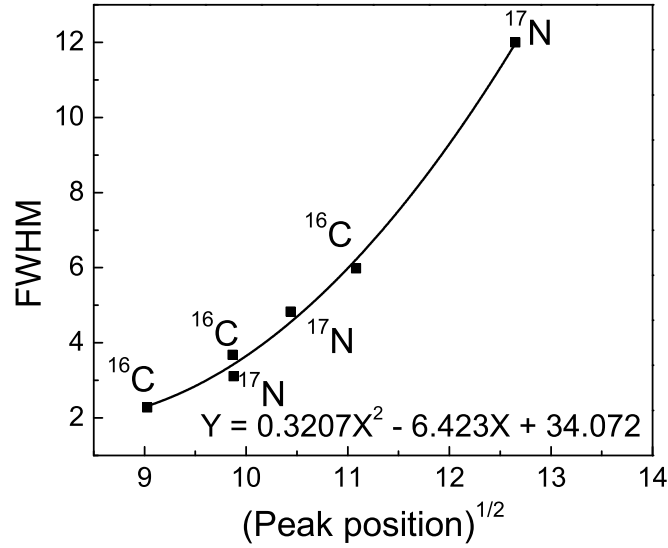


Figure 3.9: Peak shape calibration

factors obtained from the DAMM fits. The peak shape calibration was determined for the FWHM as a function of the square root of the peak centroid in the total time-of-flight spectrum. Figure 3.9 shows the peak shape calibration plot with the equation, which was used to define the FWHM used for fitting in new time-of-flight spectra. The equation was included to the DAMM program to determine FWHM when analyzing a new spectrum.

The shape of the background is an important factor in the neutron time-of-flight spectrum, since it affects the peak area. A study was carried out to establish a reasonable shape for the background based on the time-of-flight spectra collected from <sup>16</sup>C, <sup>17</sup>N, <sup>19</sup>N and <sup>20</sup>N delayed neutrons. The time-of-flight spectra for <sup>19</sup>N and <sup>20</sup>N were taken from the previous experiment that used the same neutron spectroscopic array [34]. The spectra were fitted using the DAMM program as explained above with various functions for the background and the reduced  $\chi^2$  values of the fits were compared. A third-order polynomial function, as shown in Figure 3.10, was selected as the best match to all backgrounds of the time-of-flight spectra. The high backgrounds under the strong neutron peaks were attributed to the neutron backscattering. The

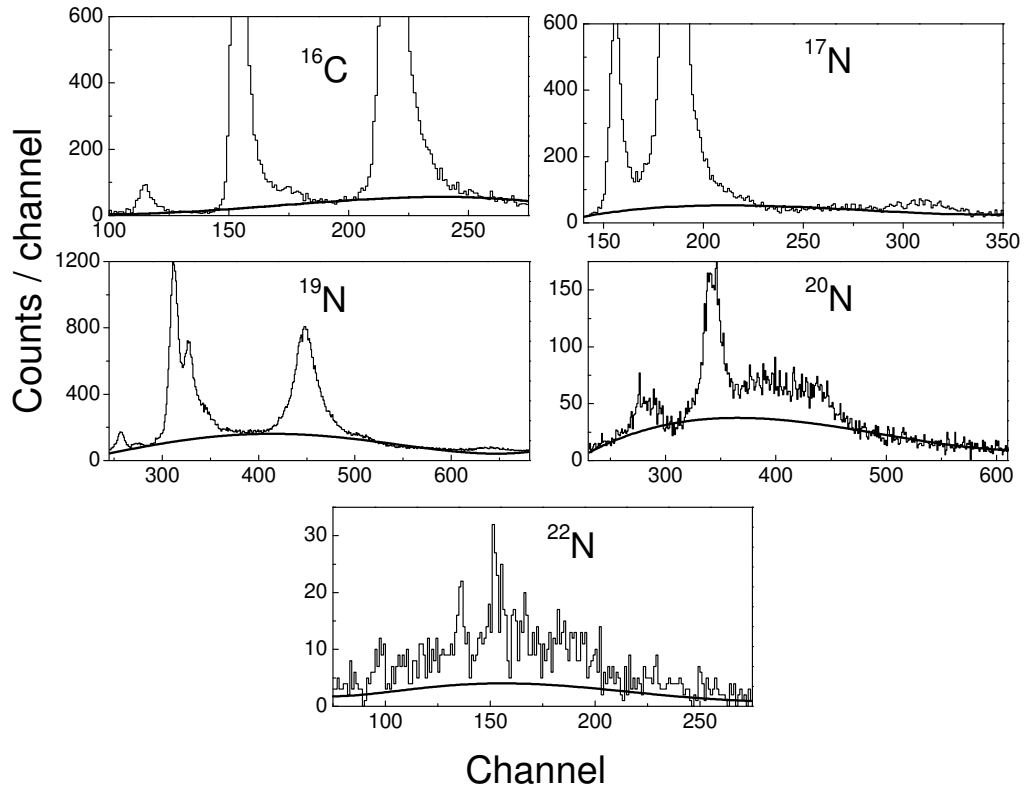


Figure 3.10: Study of neutron background shape. Third-order polynomial background was fitted for the delayed neutron spectra from  $^{16}\text{C}$ ,  $^{17}\text{N}$ ,  $^{19,20}\text{N}$  and  $^{22}\text{N}$ .

neutron time-of-flight spectrum of  $^{22}\text{N}$ , where the background was fitted with a third-order polynomial is shown in Figure 3.10.

### 3.3.4 Time Walk Correction

Good time resolution of the neutron array is important especially when low energy neutrons need to be detected. The resolution is inversely proportional to the pulse height of the signal [FWHM  $\propto$  rise-time / (signal to noise ratio)], so that the resolution of a low pulse-height signal will be poorer. In addition, constant fraction discriminators tend to have a delayed output for low pulse height signals, which is called “walk”. The typical correlation of pulse-height with time is shown in Figure 3.11, obtained using a Am-Be neutron source. If there is no walk the plot should show a straight

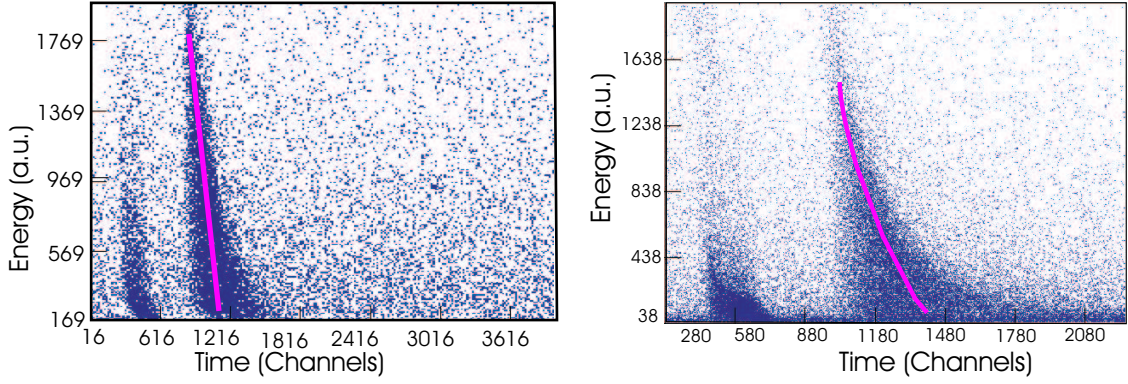


Figure 3.11: A scatter-plot of time.vs.energy obtained using an Am-Be neutron source. (left) The plot deduced with another PMT did not require a correction. (right) The plot deduced with one of the PMT that required a time walk correction.

vertical line, corresponding to a constant time for all energy neutrons, which is illustrated by Figure 3.11(left). The walk is seen as a long tailing at the lower neutron energies in Figure 3.11(right). The walk was treated by adding a correction to the raw time measurement for each PMT. Corrections were derived by fitting the plot of time versus energy from each PMT as a function of energy pulse height. The line showed in Figure 3.11 represents data points having the maximum counts. Those points were used to derive correction functions. The correction functions were applied in SpecTcl code for all neutron time-of-flight meantime measurements to produce the mean time of each event:

$$t_{mean} = \{[t_L - f_L(PH)] + [t_R - f_R(PH)]\}/2 \quad (3.7)$$

where  $t_L, t_R, f_L(PH), f_R(PH)$  are left and right time measurements, and the correction functions, respectively. The different types of functions were tried to get minimum FWHM for the beta prompt peak. The functions for the PMTs that needed a correction are given in Table 3.9.

Table 3.9: Time walk correction functions

Left-PMT number	Function	Right-PMT number	Function
01	33.0*Exp(-PH/20.1)+15.1	01	24.2-0.382*PH
02	-	02	22.4*Exp(-PH/14.0)+29.3
03	54.8*Exp(-PH/9.0)+20.5	03	14.2*Exp(-PH/18.3)+27.3
04	19.6*Exp(-PH/12.6)+12.1	04	18.0*Exp(-PH/17.8)+26.9
05	75.1*Exp(-PH/9.6)+19.8	05	19.7*Exp(-PH/17.3)+28.9
06	34.0*Exp(-PH/12.1)+18.8	06	28.1*Exp(-PH/15.7)+24.2
07	38.1-0.310*PH	07	18.0*Exp(-PH/17.8)+26.9
08	-	08	-
09	20.1*Exp(-PH/12.0)+12.7	09	-
10	18.8*Exp(-PH/11.4)+13.3	10	40.1-0.234*PH
11	41.7-0.467*PH	11	18.3*Exp(-PH/14.6)+30.1
12	14.2-0.415*PH	12	-
13	14.53-0.176*PH	13	12.1-0.1*PH
14	99.5*Exp(-PH/7.9)+16.0	14	14.0-0.256*PH
15	103.1*Exp(-PH/3.6)+30.0	15	25.6*Exp(-PH/8.3)+24.7
16	34.8-0.176*PH	16	26.7*Exp(-PH/6.4)+19.2

### 3.3.5 Neutron Efficiency Calibration

The neutron efficiency at a particular energy was defined as:

$$\epsilon_n = \frac{A}{P_n * C_{tot}} \quad (3.8)$$

where A,  $P_n$  and  $C_{tot}$  are the area under the neutron peak, neutron emission probability and the total number of beta decay events registered at the implantation detector, respectively. The total number of decay events for particular isotope observed in the implantation detector was determined by integrating the individual decay curve throughout the beam off period. The decay curve contained not only the decay of the implanted isotopes but also the decay of their daughters and granddaughters. Therefore, it was necessary to find the contribution from each isotope to the total decay curve. This was achieved by fitting the decay curve with an appropriate decay model. Decay models were developed for the  $^{16}\text{C}$  and  $^{17}\text{N}$  implantations, as explained in Appendix A, by incorporating the decay of implanted parents ( $^{16}\text{C}$  and  $^{17}\text{N}$ ), the

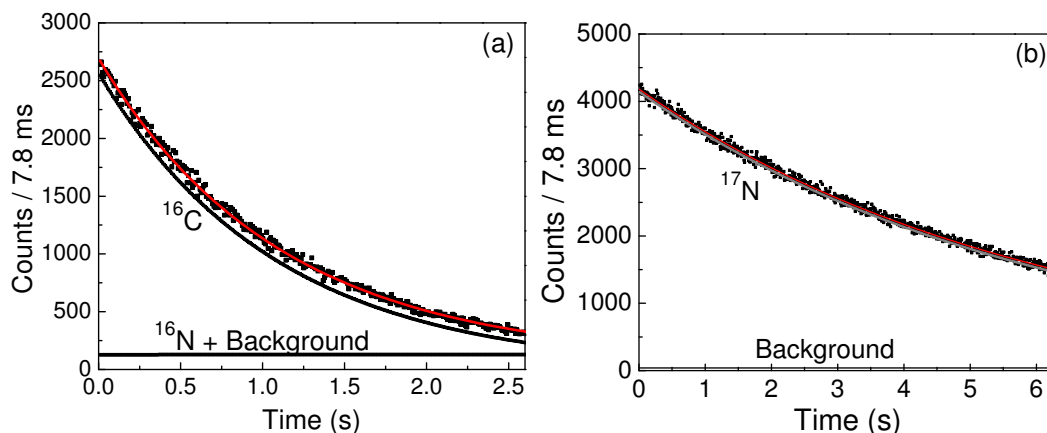


Figure 3.12: Beta decay curves of  $^{16}\text{C}$  and  $^{17}\text{N}$ . (a). The fitted beta decay curve of  $^{17}\text{N}$  with the background are shown. (b). Neutron TOF spectrum obtained in the  $^{17}\text{N}$  experiment is shown with fitted neutron peaks and the background. The neutron peak energies are given close to the peak in keV.

growth and decay of daughter ( $^{16}\text{N}$ ), and a flat background. The growth and decay contributions during the beam on period were taken into account and the fraction of isotope that was not decayed within the particular cycle was added to the next cycle. Figure 3.12 shows the fitted decay curves for (a)  $^{16}\text{C}$  and (b)  $^{17}\text{N}$  with their daughter and background contributions. The half-lives of  $^{16}\text{C}$  and  $^{17}\text{N}$  and the neutron emission probabilities were free parameters in the fitting procedure and the half-life of  $^{16}\text{N}$ , the daughter of  $^{16}\text{C}$ , was kept fixed ( $T_{1/2} = 1.8$  s). The individual decay curves of  $^{16}\text{C}$  and  $^{17}\text{N}$  were integrated and total number of decay events were found to be  $3.337(6) \times 10^5$  and  $2.0572(14) \times 10^6$  with half-lives of 755(4) ms and 4.17(7) s, respectively, which have a good agreement with literature [19](see Table 3.3). The total number of  $^{16}\text{C}$  and  $^{17}\text{N}$  beta decay events with the number of detected neutrons and their neutron emission probabilities were used to generate neutron efficiency function for the neutron spectroscopic array.

The number of neutrons that had been registered in the neutron array (peak area) was determined by fitting the total time-of-flight spectra from  $^{16}\text{C}$  and  $^{17}\text{N}$  beta decay (see Figure 3.7). The neutron peak areas from the fits and corresponding neutron

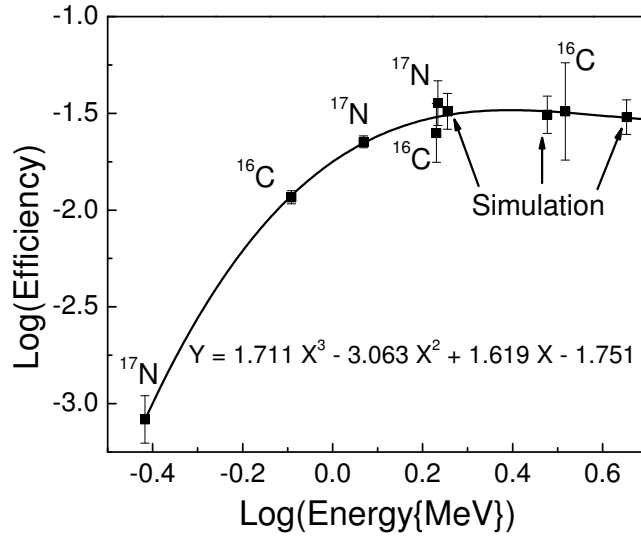


Figure 3.13: Neutron efficiency calibration

emission probabilities with their energies from the literature are given in Tables 3.6 and 3.10, respectively. The neutron detection efficiencies calculated using Equation 3.8 are given in Table 3.10 were used to generate the neutron efficiency function for the neutron spectroscopic array. The function shown in Figure 3.13 used the six experimental data points in the range of 382 - 3290 keV from beta-delayed neutrons of  $^{16}\text{C}$  and  $^{17}\text{N}$  and three data points at 1800, 3000 and 4000 keV obtained from a Monte Carlo simulation using the KSUEFF program [59,60]. The function in the high-energy region had a small slope as seen from the experimental data points in Figure 3.13. Therefore, the simulated data points were moved to match the experimental data points in flat region while keeping the slope generated by connecting three points constant. The logarithmic values of neutron energy vs efficiency were fitted to a third order polynomial, given in Figure 3.13, which was used to determine the neutron efficiencies. The lowest detection limit for energy was determined to be approximately 360 keV by extrapolating the low energy part of the efficiency function to the energy axis. The right side shoulder of the prompt peak in the time-of-flight spectrum forms the limit for the detection of high-energy neutrons, and was estimated to be 8000

Table 3.10: Efficiency calibration of neutron array using  $^{16}\text{C}$  and  $^{17}\text{N}$  beta decay.

Nuclide	Energy (keV)	Emission probability (%)	Area (Error%)	Efficiency
$^{16}\text{C}$	1714(5)	15.5(17)	1847(3.6)	0.035(4)
	810(5)	83.5(17)	3247(2.8)	0.0117(4)
	3290(30)	1.0(2)	108(9.2)	0.032(7)
$^{17}\text{N}$	1700.3(17)	6.9(1)	3556(4.4)	0.025(4)
	1170.9(8)	50.1(13)	23243(1.6)	0.0226(7)
	382.8(9)	38.0(13)	648(11.7)	0.0008(1)

keV.

## 3.4 Segmented Germanium Detector Array

Beta-delayed gamma transitions are particularly important to establish the neutron bound states in a level scheme. The detection of beta-delayed gamma-rays required high resolution and efficient gamma-ray detectors in a close geometry to the implantation detector. The beta-delayed gamma-rays were detected using eight n-type high-purity germanium (HpGe) detectors from the MSU Segmented Germanium Array (SeGA) [61]. The detail geometrical arrangement of SeGA with their energy and efficiency calibration will be discussed in following sections.

### 3.4.1 SeGA detectors

Each HpGe SeGA detector has a cylindrical shaped germanium crystal with a length of 8 cm and a diameter of 7 cm. The crystal is a closed-end coaxial crystal with a lithium-diffused central contact to produce the full energy signal. The outer surface of the crystal is doped with p-type contact to make four azimuthal and eight longitudinal segments, giving a total of 32 segments. Only the central contact output from each detector was used for this experiment. The cryostat of the crystal is mounted at a  $45^\circ$  angle to the liquid nitrogen dewar. Eight HpGe detectors (75% relative efficiency) from NSCL-SeGA were placed in a ring structure with the detector crystals parallel to the beam axis and made a distance of 14 cm from the beam axis to each detector

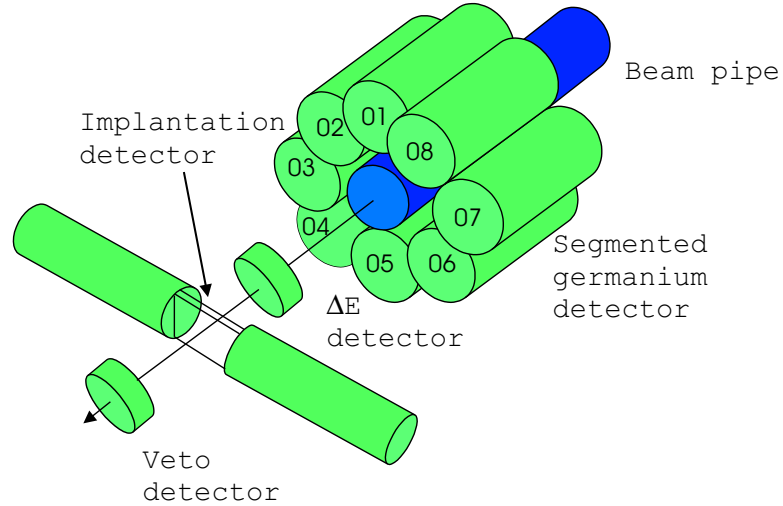


Figure 3.14: Schematic diagram of the implantation detector and SeGA array.

crystal surface. The distance from the implantation detector to the front surface of the detector crystal along the beam axis was 19.2 cm. A schematic view of the HpGe detector array setup is shown in Figure 3.14.

Each HpGe detector has two outputs from the central contact, which were used for an energy and a timing signal. The timing signal output from each detector was sent to a TC-455 NIM CFD module and subsequent outputs were used as an input to a LeCroy 380A Multiplicity logical unit to combine all signals. The electronic diagram for the HpGe detectors is shown in Figure 3.15. The combined signal (OR signal) was used for the master gate logic. The second output signal from the CFDs was the stop for a Phillips 7186 TDC. The TDC was started by the master trigger. The energy signals from the central contact were amplified using ORTEC 572 amplifiers and digitized using ORTEC 413A ADCs.

### 3.4.2 SeGA Energy Calibration

All HpGe detectors were calibrated for energy using spectra obtained with a Standard Reference Material (SRM) 4275C source, containing  $^{125}\text{Sb}$ ,  $^{154}\text{Eu}$  and  $^{155}\text{Eu}$ , along with single sources of  $^{60}\text{Co}$ ,  $^{152}\text{Eu}$ ,  $^{241}\text{Am}$  and  $^{207}\text{Bi}$ . In addition, the gamma-ray energies from known daughter decays from the implanted isotopes and the natural

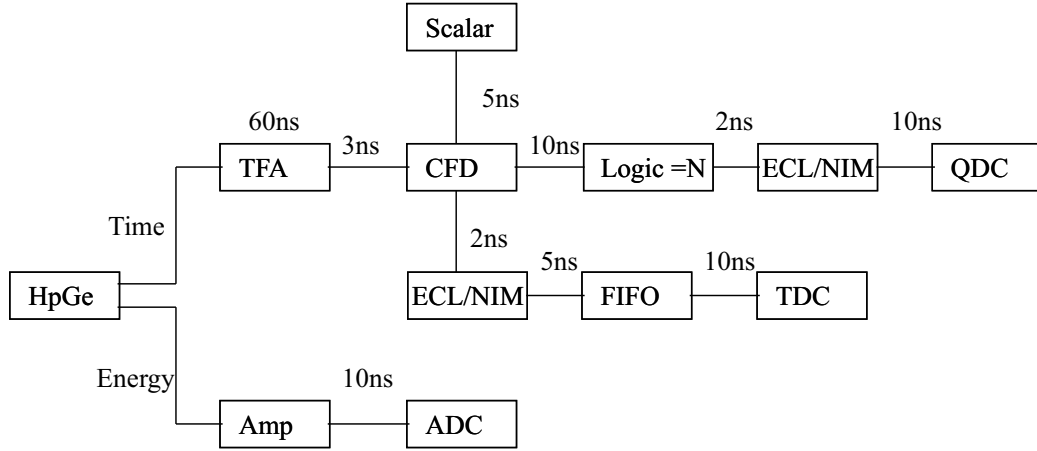


Figure 3.15: Schematic electronic diagram for SeGA array.

background gamma-ray peaks from  $^{40}\text{K}$  and  $^{208}\text{Tl}$  were used to extend the energy calibration up to 6200 keV. The sources were placed at the location of implantation detector and gamma-ray spectra were collected for all detectors. The gamma-ray peaks were fitted with Gaussian functions using the DAMM program. Two energy calibrations for low and high gamma-ray energy ranges were established by weighted fitting the photopeak centroid versus the known gamma-ray energy for each detector. The low and high energy ranges were chosen as 60 - 1500 and 1500 - 6200 keV, respectively, to achieve the best fit to the experimental data. Energy data points at 1275, 1298, 1333, 1406, 1460, 1596, 1633 and 1770 keV were used in both calibrations to obtain a smooth transition between two calibrations. The low-energy range calibrations were fitted to second order polynomials and the high energy range calibrations were fitted to straight lines for all detectors. The residuals, which were defined as the difference between the literature energy and the calibrated energy, are given in Figure 3.16 and were within  $\pm 0.6$  keV for all detectors. Energy calibrated spectra from all detectors were added to produce the total gamma-ray spectrum, which was used for further analysis. The errors for gamma-ray energy were estimated by accounting for the errors from the calibration fit and the errors in the peak position given by DAMM code.

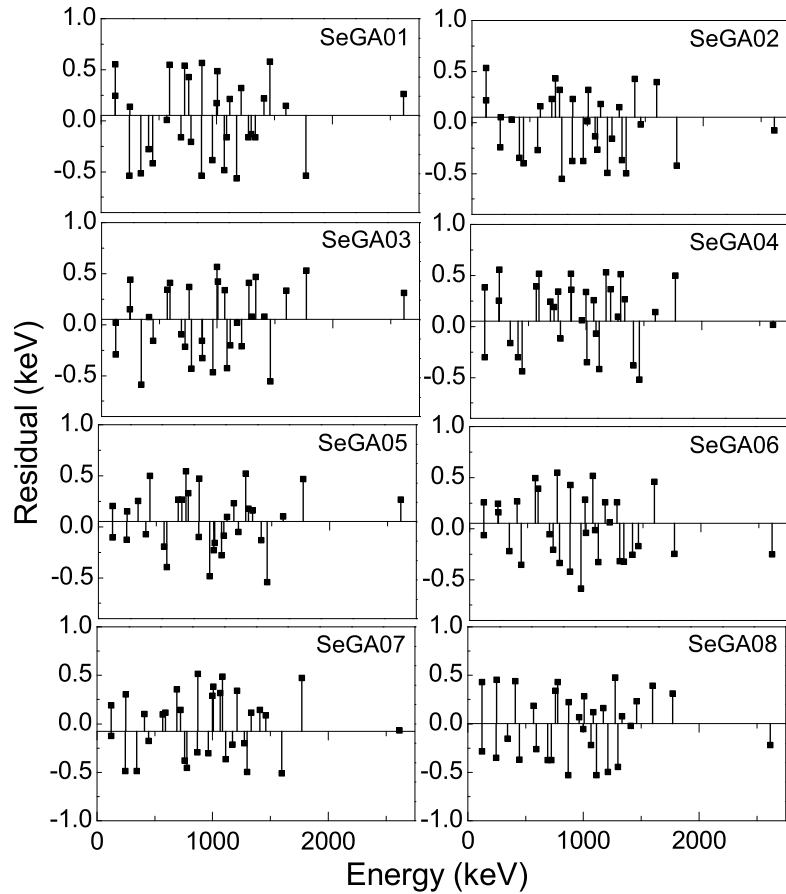


Figure 3.16: Residuals of the energy calibration for seGA detectors

### 3.4.3 SeGA Efficiency Calibration

The gamma-ray coincidence efficiency measurements for the full energy peak were carried out using the radioactive sources off-line as well as with the beta decay of well-known daughters from the on-line measurement. For the off-line measurements, a NaI scintillation detector was used as a trigger with same electronic setup replacing the implantation detector signal. The  $^{60}\text{Co}$ ,  $^{152}\text{Eu}$  and  $^{204}\text{Bi}$  sources were placed both in front and in back of the implantation detector to minimize the effect coming from the implantation detector thickness for off-line efficiency calibration. The energies of the photons from each source are given in Table 3.11. The aluminum degrader

Table 3.11: Off-line coincidence efficiency calibration data for SeGA.

Source	NaI gate (keV)	NaI Count	Energy (keV)	Coincidence fraction	Peak area	Efficiency
$^{152}\text{Eu}$	1408	2.46E+5	122	1	6673	2.7(3)E-2
$^{152}\text{Eu}$	867	1.28E+5	241.2	0.427	2078	3.81(5)E-2
$^{152}\text{Eu}$	344	1.89E+6	268.2	0.00287	216	3.9(3)E-2
$^{152}\text{Eu}$	779	4.92E+5	341	0.65	11906	3.72(3)E-2
$^{152}\text{Eu}$	344	1.71E+6	364.4	0.0315	1901	3.52(4)E-2
$^{152}\text{Eu}$	344	1.75E+6	407.8	0.083	5420	3.74(3)E-2
$^{152}\text{Eu}$	122	1.20E+5	441.2	0.0458	203	3.69(1)E-2
$^{204}\text{Bi}$	1064	4.51E+5	570	1	14001	3.11(2)E-2
$^{152}\text{Eu}$	344	1.45E+6	583.4	0.0171	767	3.09(4)E-2
$^{152}\text{Eu}$	344	1.41E+6	675.7	0.0172	689	2.8(4)E-2
$^{152}\text{Eu}$	344	1.41E+6	710	0.0034	139	2.9(14)E-2
$^{152}\text{Eu}$	344	1.36E+6	776.4	0.4703	16553	2.6(2)E-2
$^{204}\text{Bi}$	570	1.03E+6	1064	0.8412	19579	2.3(2)E-2
$^{152}\text{Eu}$	344	1.27E+6	1086.3	0.0628	1757	2.2(4)E-2
$^{152}\text{Eu}$	122	8.57E+4	1112.1	0.2204	388	2.1(7)E-2
$^{60}\text{Co}$	1333	1.24E+5	1174	0.9992	2770	2.2(2)E-2
$^{152}\text{Eu}$	122	8.50E+4	1210	0.0229	39	2.0(5)E-2
$^{152}\text{Eu}$	344	1.22E+5	1298.3	0.059	1429	1.9(2)E-2
$^{60}\text{Co}$	1174	1.49E+5	1333	1	2937	1.9(2)E-2
$^{152}\text{Eu}$	122	8.56E+4	1406	0.3389	594	2.0(7)E-2
$^{204}\text{Bi}$	570	8.86E+5	1770	0.0691	932	1.5(1)E-2

thickness of 15.704 mm, which was used in the  $^{22}\text{N}$  experiment, was placed in to perform the calibration under the same geometry.

The off-line coincidence efficiency was established by measuring gamma-ray events registered in the HpGe detectors triggered by the NaI detector. A software gate was placed on one of the peaks detected in the NaI detector and applied to the total gamma-ray spectrum to generate the coincidence spectrum for the sum of all SeGA detectors from a particular source. The peak areas of this gated spectrum were obtained by a Gaussian fit. The total number of triggered events in the NaI detector was determined by integrating the background subtracted area under the gated region of the peak. The gamma-gamma coincidence emission probability for a particular gamma-ray pair was calculated by considering the gamma-ray cascade properties of the decay scheme. Table 3.11 shows data from the coincidence measurements using

Table 3.12: On-line coincidence efficiency calibration data for SeGA:<sup>22</sup>N experiment.

Beta Decay nuclide	Energy (keV)	Emission probability (%)	Beta decay events	Peak area	Efficiency
<sup>22</sup> F	1274.537	100	28573	576	2.0(1)E-2
<sup>22</sup> F	2082.6	81.9	28573	348	1.5(1)E-2
<sup>22</sup> F	2166.1	61.6	28573	230	1.3(1)E-2
<sup>21</sup> F	350.725	89.55	18598	635	3.8(2)E-2
<sup>20</sup> F	1633.602	99.9995	9955	168	1.7(2)E-2
<sup>25</sup> Na	974.72	14.95	34545	123	2.3(6)E-2
<sup>16</sup> N	6125.41	67.2	10622	49	6.9(5)E-3

off-line sources and the coincidence efficiencies calculated by the division of the SeGA peak area by the total number of triggered events and the corresponding gamma-gamma coincidence emission probability.

In addition to the off-line efficiencies, the well-known daughter/granddaughter decay of implanted isotopes provided a set of efficiency data points measured under the experimental conditions. The beta decay of <sup>22</sup>F, <sup>21</sup>F, <sup>20</sup>F and <sup>25</sup>Na provided strong gamma-ray peaks with well-known gamma-ray emission probabilities, given in Table 3.12, from the <sup>22</sup>N implantation. The decay of <sup>16</sup>N also provided a gamma-ray peak at 6125.41 keV from the <sup>16</sup>C implantation, which was used to extend the gamma-ray efficiency to high energy. Aluminum degrader thickness of 15.506 mm (0.198 mm thinner than used in the <sup>22</sup>N experiment) used in the <sup>16</sup>C experiment did not make a significant difference to the efficiency as the attenuation is small at high energies. The on-line efficiencies given in Table 3.12 were calculated using the peak area, the total number of beta decay events derived from the decay curve fitting and the gamma-ray emission probability. The on-line and off-line efficiencies were used to establish the coincidence efficiency curve, shown in Figure 3.17, for the <sup>22</sup>N experiment analysis. The efficiency function for the <sup>22</sup>N experiment was fitted to the fourth order polynomial given in the same figure.

The low energy part of the efficiency function is highly sensitive to the absorber thickness that blocked some of the incoming gamma-rays. In <sup>23</sup>O experiment, an Al

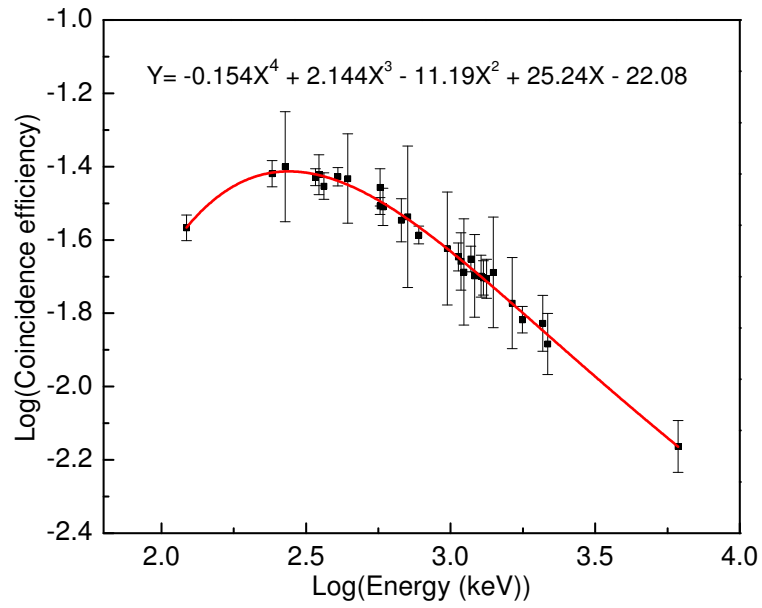


Figure 3.17: Coincidence efficiency calibration for SeGA:<sup>22</sup>N experiment.

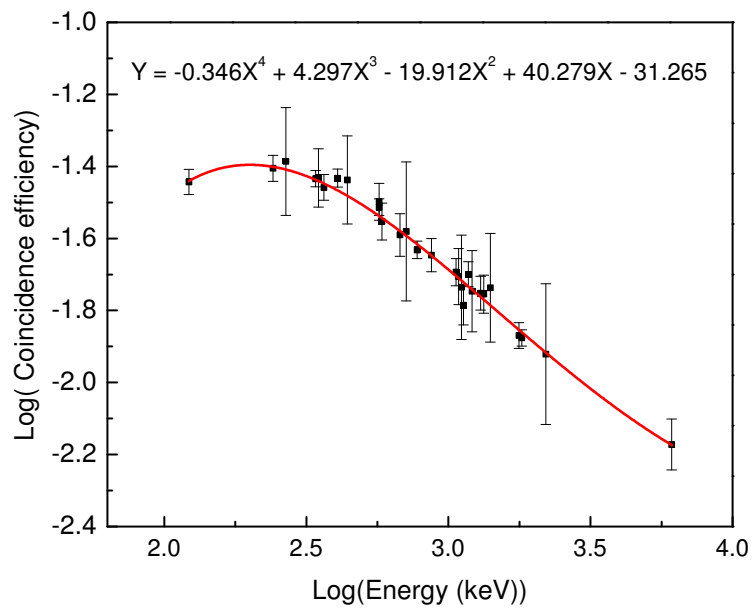


Figure 3.18: Coincidence efficiency calibration for SeGA:<sup>23</sup>O experiment.

Table 3.13: On-line coincidence efficiency calibration data for SeGA: $^{23}\text{O}$  experiment.

Beta Decay nuclide	Energy (keV)	Emission probability (%)	Beta decay events	Peak area	Efficiency
$^{17}\text{N}$	870.71	3.3	2085015	1553	2.3(1)E-2
$^{17}\text{N}$	2184.48	0.34	2085015	72	1.0(2)E-2
$^{26}\text{Na}$	1128.6	5.8754	840089	795	1.64(9)E-2
$^{26}\text{Na}$	1811	99.08	840089	10816	1.33(3)E-2
$^{23}\text{Ne}$	438.3	32.9	171285	1885	2.41(9)E-2
$^{21}\text{F}$	348.8	89.55	10775	355	3.7(3)E-2

degrader thickness of 11.412 mm (4.292 mm thinner than the thickness used in the previous calibration process) was used to ensure implantation into proper detector. Another efficiency calibration was established using the on-line efficiency data points to analyze  $^{23}\text{O}$  experimental data. The peak efficiencies of gamma-rays associated with beta decay of  $^{26}\text{Na}$ ,  $^{23}\text{Ne}$  and  $^{21}\text{F}$ , shown in Table 3.13, were used along with the efficiency data measured from the beta decay of  $^{17}\text{N}$  and  $^{16}\text{N}$ , to produce the efficiency function, which had a similar shape of the function generated with the off-line efficiency data points. The coincidence efficiency calibration for the  $^{23}\text{O}$  experiment is shown in Figure 3.18 with its calibration function.

# Chapter 4

## Data Analysis and Results

### 4.1 Analysis of The $^{22}\text{N}$ Beta Decay Experiment

The  $^{22}\text{N}$  radioactive beam was produced by fragmentation of a 140 MeV/A  $^{48}\text{Ca}$  beam on a 846 mg/cm $^2$   $^9\text{Be}$  target. The purity of the beam was analyzed at two places along the beam path. The beam was analyzed the dE detector just before the implantation detector.  $^{22}\text{N}$  was produced as part of a cocktail beam with impurities of  $^{25}\text{F}$ ,  $^{24}\text{O}$ ,  $^{20}\text{C}$ ,  $^{10,12}\text{Be}$ ,  $^{8,9}\text{Li}$  and  $^6\text{He}$ . Figure 4.1 shows part of the particle identification (the

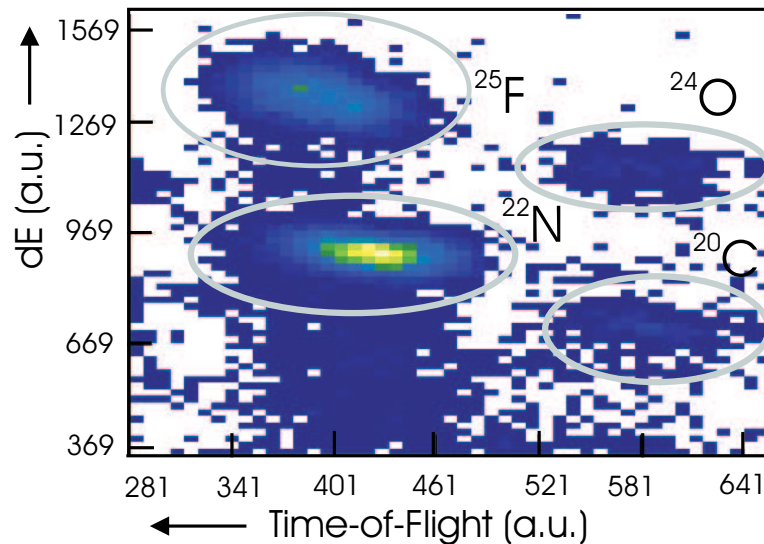


Figure 4.1: Identification of nuclides produced in  $^{22}\text{N}$  experiment. The particle identification was done using the dE detector before implantation and part of the spectrum is shown.

energy loss verses the RF time-of-flight) spectrum obtained from the dE detector and the particles are labeled in the spectrum. Very light particles are not shown in the figure. The composition of the beam was also checked at the focal plane of the A1900 before the implantation runs and is given in Table 4.1. The composition of nuclides stopping in the implantation detector was analyzed with help of the dE and Veto detectors by making appropriate gates on the particle IDs to apply on the Veto detector, and vice versa. The number of particles reaching the Veto detector was used to obtain the number of particles stopped at the implantation detector. The purity of the beam at the implantation detector and literature half-lives of the constituents are summarized in Table 4.1. The analysis of the gated particle ID spectra generated from dE and veto detectors showed approximately equal number of  $^{20}\text{C}$  particles in both spectra. This concluded that the  $^{20}\text{C}$  nuclei passed through the implantation detector with negligible implantation of  $^{20}\text{C}$ .

The beta decay of  $^{22}\text{N}$  produces the beta decay daughter  $^{22}\text{O}$ , the beta-delayed one neutron daughter  $^{21}\text{O}$ , and granddaughters of  $^{22}\text{F}$  and  $^{21}\text{F}$  as was indicated in Figure 1.8. In addition, the beta decay chains of  $^{25}\text{F}$  and  $^{24}\text{O}$ , which were impurities of the beam, were observed in the same experiment and they will be addressed separately. It is important to know whether all daughters and granddaughters produced from the beta decay of the parent have achieved their saturation activities under the experimental conditions, as the activities of the daughter decay chains were used to calculate the beta decay branch to the ground state and total neutron emission probability. Simulations were carried out to demonstrate the saturation of the activities during the experiment.

The  $^{22}\text{N}$  beta decay chain was modeled by using the Bateman equations [64] including beam-on/off mode effects. The simulations were done at a constant implantation rate of 100 pps during the beam-on time. Hence, the activity of the parent grows during the beam-on period and the activity then decays to daughters and subsequently to granddaughters during the beam-off period. The activity that did not

Table 4.1: Beam of composition of  $^{22}\text{N}$  experiment after the A1900 and at the implantation detector.

Nuclide	Purity at A1900 (%) <sup>1</sup>	Purity at implantation detector (%)	Half-life (ms)
$^{22}\text{N}$	49.8	51.8	24(5) <sup>2</sup>
$^{25}\text{F}$	27.6	35.6	90(9) <sup>3</sup>
$^{24}\text{O}$	8.1	12.6	65(5) <sup>4</sup>
$^{20}\text{C}$	3.5	-	14(+6-5) <sup>5</sup>

$^{110,12}\text{Be}$ ,  $^{8,9}\text{Li}$  and  $^6\text{He}$  contributed to the remaining 11%

<sup>2</sup>Average from Refs. [38, 62, 40]

<sup>3</sup>From Ref. [16]

<sup>4</sup>From Ref. [63]

<sup>5</sup>From Ref. [38]

decay during the previous cycles was added to the next cycle in addition to the growth and decay of nuclei produced during the present cycle. For example, the  $n^{\text{th}}$  cycle has the decay contributions from all previous  $(n-1)$  number of cycles in addition to the growth and decay during the  $n^{\text{th}}$  cycle. The activities were added to find the final activity. The relationship between the beta-delayed neutron daughter decay chain and the direct beta decay chain was established based on the literature neutron emission probability. Figure 4.2 shows how the total activity varies with time for all nuclei in the decay chains. The growth and decay of  $^{22}\text{N}$  during the first 4000 ms is shown in Figure 4.2(a) and the decay curves of  $^{22}\text{O}$  and  $^{22}\text{F}$  are shown in Figure 4.2(b) and (c), respectively. The figures indicate that the activities of the daughter and the grand-daughter approach saturation after the first 40 s of the experimental time. One can conclude that the parent and daughter activities in this decay series were saturated given that each data taking run was approximately 30 minutes long.

#### 4.1.1 Total Number of Beta Decay Events

The calculation of the neutron and gamma-ray transition probabilities required knowledge of the total number of beta decay events registered in the implantation detector from a particular decay. In general, the integration of decay curve during the exper-

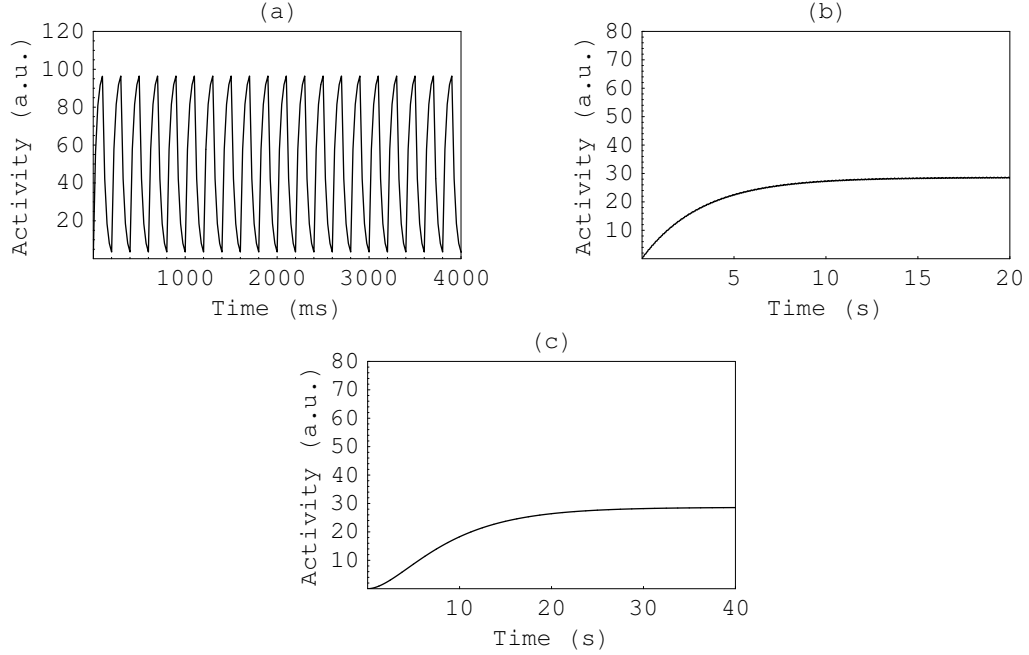


Figure 4.2: Growth and decay curves for the  $^{22}\text{N}$  decay series calculated using a decay model with a production rate of 100 pps for the parent of the decay series. The beam on/off modes were included in the calculation. (a)  $^{22}\text{N}$  activity curve, (b)  $^{22}\text{O}$  activity curve and (c)  $^{22}\text{F}$  activity curve are plotted as a function of time.

imental run time can be used to deduce the total number of beta decay events. The individual decay contribution from a particular nuclide was extracted by fitting a decay model to the decay curve. The decay model was developed as explained above. The Bateman equations were written for all implanted nuclei and their decay chains including the beam-on/off effects to model the beta decay events observed at the implantation detector. The fit to the beta decay curve was performed using this model, where four parameters, namely the half-life, the total neutron emission probability and the initial activity of  $^{22}\text{N}$ , and a flat background, were allowed to vary freely. The ratios of implanted radioactive nuclides measured from the dE and Veto detectors were used to fix the initial activity ratios of the impurity nuclei. The half-lives of all daughters and granddaughters, which are reported in the literature [19] ( values are given in Appendix A), were kept as constant through fitting procedure. The half-lives of  $^{25}\text{F}$  and  $^{24}\text{O}$ , which were deduced in this work to be 73(11) and 53(8) ms, respectively, from the gamma-ray gated decay curves, were included in the model as fixed

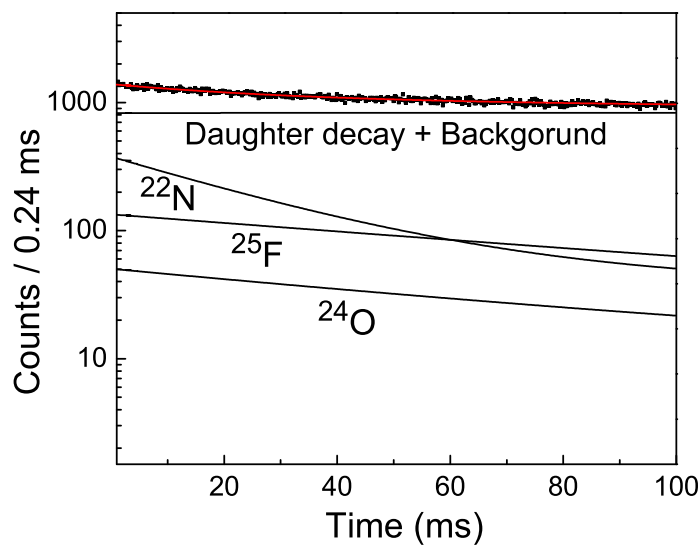


Figure 4.3: Ungated beta decay curve of the  $^{22}\text{N}$  experiment. The individual decay contributions from the implanted nuclei are shown with the total decay contribution from daughters and granddaughters and the background.

values. The reported neutron emission probabilities of 23(5)% [16] and 58(12)% [38] for  $^{25}\text{F}$  and  $^{24}\text{O}$ , respectively, were also used. Figure 4.3 shows the individual decay contributions from each implanted nuclide, their daughters and granddaughters, and the background to the total decay.

The individual components to the total decay curve fitting in Figure 4.3 were integrated through the beam-off period to determine the total number of detected beta decay events, which are given in Table 4.2. The half-life of  $^{22}\text{N}$ , given in the same table, was a result of the fitting procedure, since the other half-lives were taken to be fixed values. The total number of beta decay events corresponding to the individual nuclide decay were used to calculate the beta-delayed neutron and gamma-ray emission probabilities.

Table 4.2: Detected beta decay events from the  $^{22}\text{N}$  experiment

Nuclide	Total number of beta decay events	Half-life (ms)	Literature Half-life (ms)
$^{22}\text{N}$	$5.58(2)\times 10^4$	21(7)	24(5)
$^{25}\text{F}$	$3.84(4)\times 10^4$	73(11)	90(9)
$^{24}\text{O}$	$1.37(4)\times 10^3$	53(8)	65(5)

#### 4.1.2 The analysis of the neutron time-of-flight spectrum from $^{22}\text{N}$ cocktail beam

The analysis of the neutron time-of-flight spectrum included the identification of the beta-delayed neutrons with their energies and emission probabilities. Figure 4.4.(a) shows the beta-delayed neutron time-of-flight spectrum from the  $^{22}\text{N}$  experiment, which was generated by adding individual neutron spectra of all 16 neutron bars. The prompt peak, which results from relativistic electrons from the beta decay and travel from the implantation detector to neutron detectors, was centered at channel 45.4 for all neutron detectors. These electrons traveling at a velocity near the speed of light were used to establish a time reference for the neutron time-of-flight measurements. The small peak marked as ‘‘Cosmic-ray peak’’ is the result cosmic-rays passing through the neutron detectors first and the implantation detector. The peaks to the right of the prompt peak in Figure 4.4.(a), which are expanded in Figure 4.4.(b), are considered to be neutron peaks from the beta decay of the implanted nuclei.

The neutron peak shapes were defined based on the peak shape calibration discussed in Chapter 3. The coefficients of the peak shape calibration, given in Figure 3.9, and appropriate asymmetric factors were used in the DAMM program to define the peak shape at a given peak position. In addition, the channel number regions of 80-95 and 105-120 were tested with giving different positions as initial gaussians for the peak positions and changing the number of peaks for the region to check for other combinations that might fit the spectrum under the given peak shape constraints. A third-order polynomial function was used to fit the background as discussed in

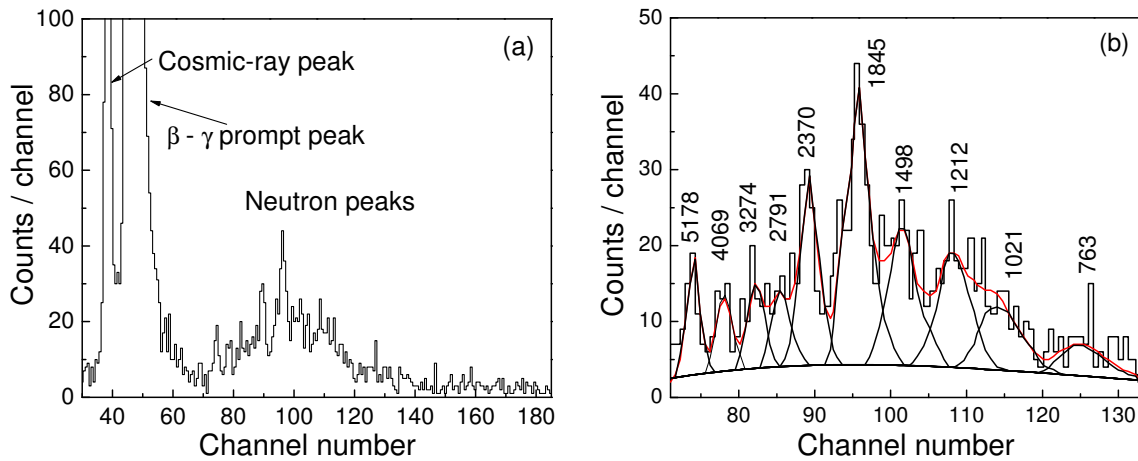


Figure 4.4: Neutron time-of-flight spectrum from the  $^{22}\text{N}$  experiment. The (a) Beta-delayed neutron time-of-flight spectrum shows the prompt, Cosmic-ray and neutron peaks. The (b) Neutron peaks were fitted with ten asymmetric Gaussian functions and a background. The neutron energies are given in keV above the peaks.

Chapter 3. Figure 4.4.(b) shows the fitted neutron time-of-flight spectrum, where the best minimum reduced  $\chi^2$  value was achieved with ten asymmetric Gaussian peaks and the background. The peak fitting results given in Table 4.3 were used along with the neutron energy and efficiency calibrations to determine the neutron energies and the associated number of neutrons originated from the beta decay, respectively. The calculated neutron energies and the number of neutrons for each neutron peak in Figure 4.4(b) are given in Table 4.3 were used to assign the neutron energy groups to the beta decay.

The assignment of a delayed neutron transition to a particular beta decay parent is generally done based on the half-life. The half-life curves gated on neutrons were generated for this purpose. The statistically significant decay curves were fitted with a single decay constant and flat background. The half-life, the initial activity and the background were free parameters of the fit. Figure 4.5 shows the fitted neutron-gated decay curves along with the neutron energies in keV and resulting half-lives in ms. The neutron-gated decay curves generated from the neutron peaks of 2791, 3274 and 4069 keV, which are not well resolved, were not analyzed due to their poor statistics.

Table 4.3: The neutron time-of-flight data from the  $^{22}\text{N}$  beta decay experiment, neutron energies and neutron gated half-lives.

Peak position	Area (Error%) (Error%)	FWHM channels	Energy (keV)	Gated half-life (ms)	Number of neutrons
73.9	53(17)	3.55	5178(24)	18(4)	1808(36)
78.1	44(19)	3.80	4069(15)	-	1437(13)
82.2	55(17)	4.04	3274(11)	-	1621(14)
85.6	51(20)	4.50	2791(8)	-	1762(35)
89.3	121(11)	4.50	2370(6)	22(5)	3688(51)
95.6	223(8)	5.72	1845(4)	22(4)	7127(72)
101.5	144(11)	6.65	1498(3)	16(5)	5130(61)
108.2	148(12)	7.81	1212(2)	68(16)	6400(83)
114.1	98(17)	9.17	1021(2)	20(5)	5341(62)
125.4	68(29)	11.50	763(1)	18(6)	6589(70)

The analysis of these data shows that neutron energy groups of 763, 1021, 1498, 1845, 2370 and 5178 keV originated from the same beta decay as their half-lives are in reasonable agreement. Moreover, these neutrons have been assigned to the beta decay of  $^{22}\text{N}$ , since the average gated half-life of 19(2) ms agreed within uncertainties with the average literature half-life of the  $^{22}\text{N}$  beta decay [19]. The neutron peak at 1212 keV had a gated half-life of 68(16) ms, which is clearly different from the half-lives of the other neutron groups. A comparison of the half-life with the literature half-lives of the implanted nuclei indicated that this neutron group could originate from either  $^{25}\text{F}$  or  $^{24}\text{O}$  beta decay. Further assignments of neutron groups were made based on the intensity requirement by the desired decay scheme and will be discussed below.

### 4.1.3 Gamma-ray Identification

The total beta-gamma coincidence spectrum obtained from the  $^{22}\text{N}$  cocktail radioactive beam, shown in Figures 4.6 and 4.7, contains beta-delayed gamma-rays events from the  $^{22}\text{N}$ ,  $^{25}\text{F}$  and  $^{24}\text{O}$  decay chains observed during the beam-off time period. The identified gamma transitions are labeled based on their parent decay. The gamma-ray assignments were made based on the half-lives obtained from gamma-ray gated

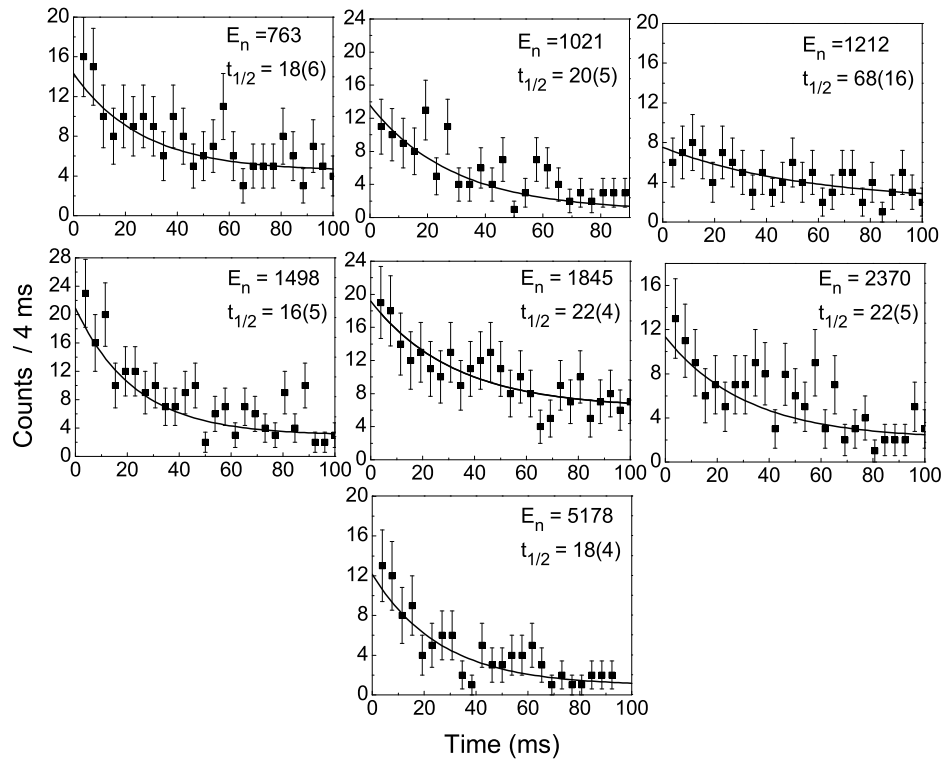


Figure 4.5: Neutron gated decay curves from the  $^{22}\text{N}$  experiment. The neutron energies in keV and half-lives in ms are shown.

decay curves, the experimentally known gamma-ray transitions and intensities, differences between experimentally known energy levels of possible daughters, and the observation of peaks in the beta-gamma-gamma triple coincidence spectra. In addition, the gamma-ray transitions from the beta decay of long lived isotopes such as  $^{60}\text{Co}$ ,  $^{40}\text{K}$  and  $^{208}\text{Tl}$  were also observed in the unshielded detectors and are labeled in Figures 4.6 and 4.7.

The gamma-ray transitions with energies 637, 708, 918, 944, 1863, 1874 and 2501 keV were compared with the observed gamma-ray transitions in the  $^{22}\text{O}$  beta decay studies reported by Hubert et al. [65] and Weissman et al. [66]. The agreement of the gamma-ray energies and their intensities leads to the conclusion that the above gamma-ray transitions can be attributed to the beta decay of  $^{22}\text{O}$ , which is the daughter of the  $^{22}\text{N}$  beta decay. The summary of all observed gamma-rays with their intensities and assignments are given in Appendix B. The known gamma-ray peak at 72 keV from  $^{22}\text{O}$  was not observed in the spectrum reported here due to the

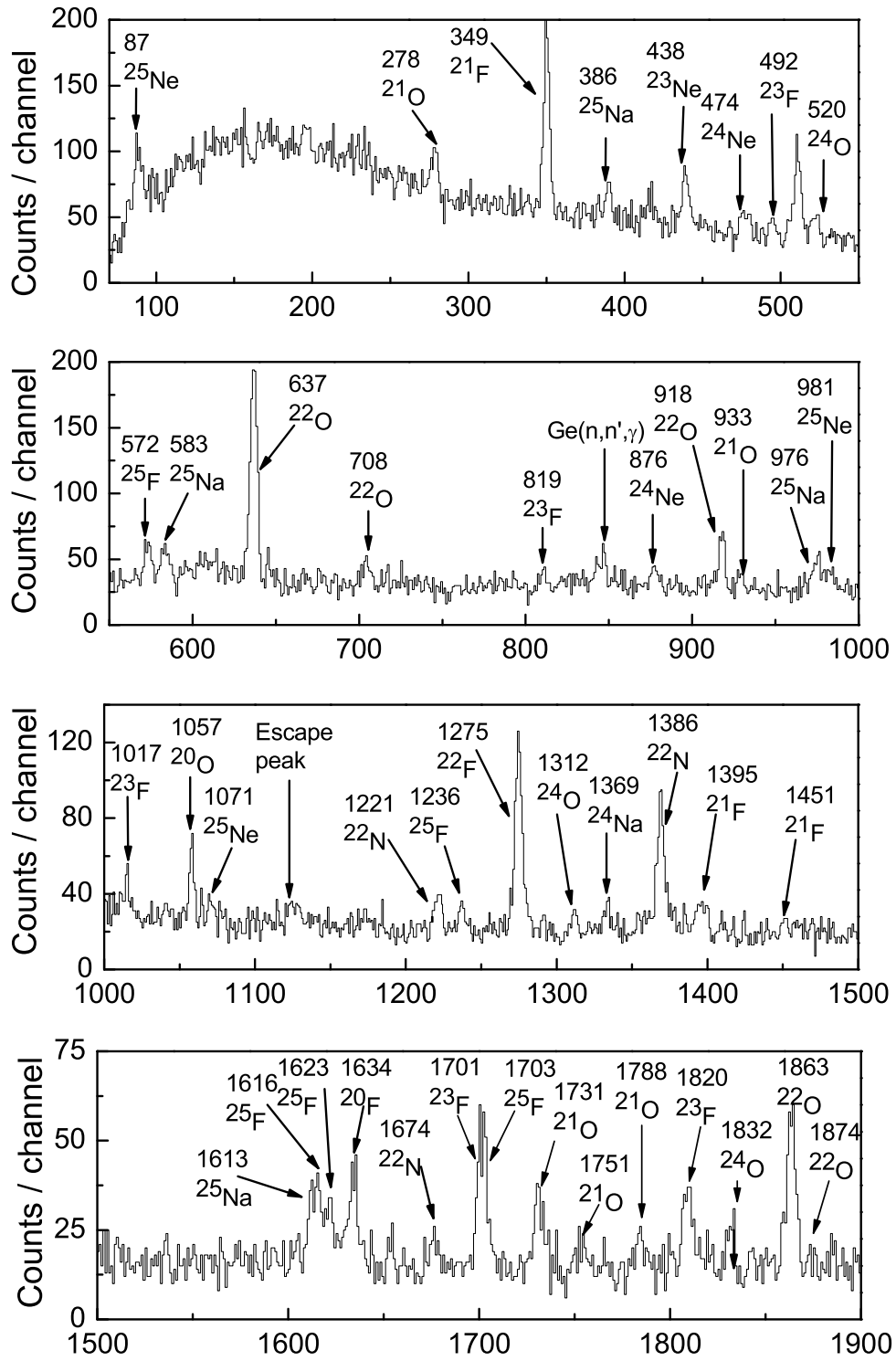


Figure 4.6: Total beta-gamma coincidence spectrum from the  $^{22}\text{N}$  experiment: Part I. Gamma-rays are labeled with their parent nuclei and energies in keV.

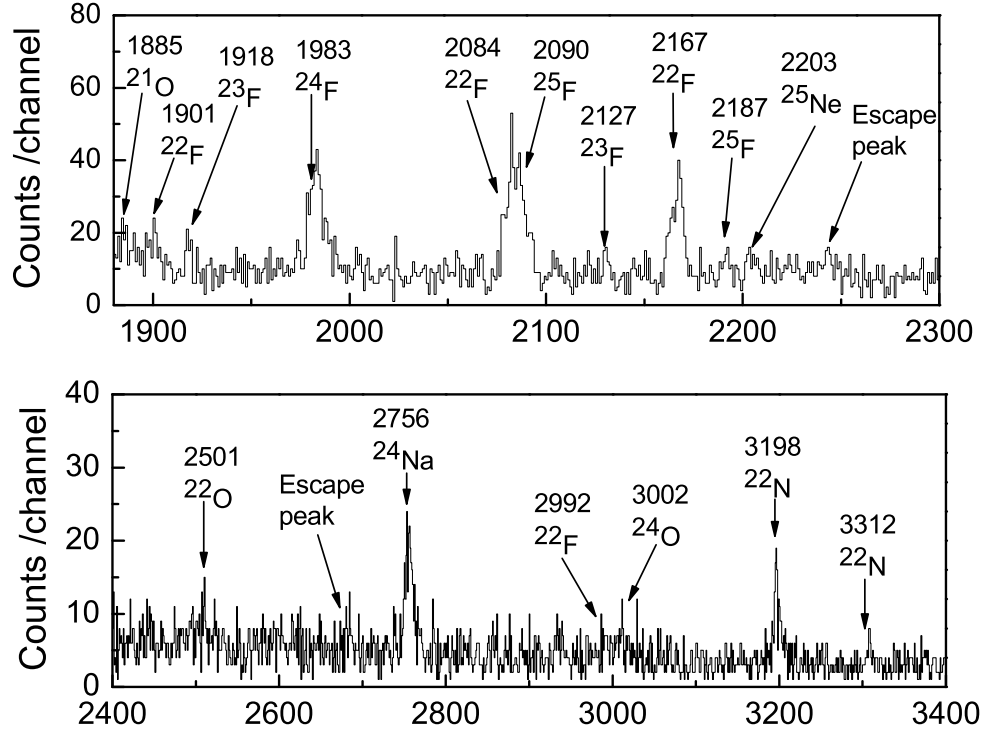


Figure 4.7: Total beta-gamma coincidence spectrum from the  $^{22}\text{N}$  experiment: Part II. Gamma-rays are labeled with their parent nuclei and energies in keV.

low energy threshold limits (about 78 keV) of the SeGA detectors. The gamma-ray transitions from the beta decay of  $^{22}\text{F}$ , the granddaughter of  $^{22}\text{N}$ , reported by Davids et al. [67] were found at energies 1275, 1901, 2084, 2167, 2992 and 4372 keV and their relative intensities agreed with those published in Ref. [67]. The rest of the gamma-ray transitions from the beta decay of  $^{22}\text{F}$  reported by Davids et al. were not observed here due to their low intensities.

A beta decay study of  $^{21}\text{O}$ , the beta-delayed single neutron daughter of  $^{22}\text{N}$ , was reported out by Alburger et al. [68]. They observed gamma-ray transitions at energies 279.92(6), 933.2(3), 1450.5(2), 1729.2, 1730.28(8), 1754.74(8), 1787.16(8), 1884.01(9), 3179.43(10), 3459.38(13), 3517.40(10), 4572.2(4) and 4583.5(3) keV. The highest absolute intensity of 45.6(6)% for the 1730.28 keV gamma-ray transition was reported in the  $^{21}\text{O}$  beta decay. The transitions at 278(3), 933(3), 1451(6),

1731(5), 1751(5), 1788(5) and 1885(4) keV were observed in the present work, shown in Figures 4.6 and 4.7, and assigned to the beta decay of  $^{21}\text{O}$  based on the energies and intensity ratios (given in Appendix B) that match with the reported values within uncertainties. The other known transitions did not have significant intensities to observe in this spectrum. The granddaughter of the  $A = 21$  decay chain is  $^{21}\text{F}$ , which was first studied by Harris et al. [69] and later, by Warburton et al. [70] has fifteen known gamma-ray transitions (see in Appendix B). The most intense gamma-rays with energies at 351 and 1395 keV were observed in this work.

Apart from the gamma-rays associated with the direct beta decay chain and the beta-delayed single neutron daughter decay chain of  $^{22}\text{N}$ , gamma-rays attributed to the  $A = 20$  mass chain, which was not implanted in this experiment, were found in the beta-gamma coincidence spectrum. The only mechanism that leads to the  $A = 20$  mass chain is the emission of two neutrons from the beta decay of  $^{22}\text{N}$ . Note that  $^{21}\text{O}$  is not a delayed neutron emitter to feed the  $A = 20$  mass chain. The gamma-ray transitions observed here with energies at 1057 and 1634 keV agree with those having energies 1056.78(3) and 1633.602(15) keV reported in the beta decay studies of  $^{20}\text{O}$  and  $^{20}\text{F}$ , respectively, shown in Figures 4.6 and 4.7. They are the only major transitions originated from these beta decays and have emission probabilities of 99.975% and 99.9995%, respectively. The consistency of energies and emission probabilities for these respective transitions in this experiment with the corresponding reported values suggests that the above transitions originated from the beta decay of  $^{20}\text{O}$  and  $^{20}\text{F}$ , respectively. The identifications were confirmed by their gated half-lives.

The assignment of the gamma-ray transitions to levels of  $^{22}\text{O}$  following beta decay of  $^{22}\text{N}$  was carried out based on the previous knowledge of gamma-ray decay in the nucleus. The 1386, 3198 and 3312 keV gamma-ray transitions shown in Figures 4.6 and 4.7 and cited in Refs. [21, 35, 23, 22] were also observed in the present study. The rest of the gamma-rays attributed to  $^{22}\text{O}$  were not observed in the present work. In addition, the 1221 keV transition, which was reported by Stanoiu et al. [21] as

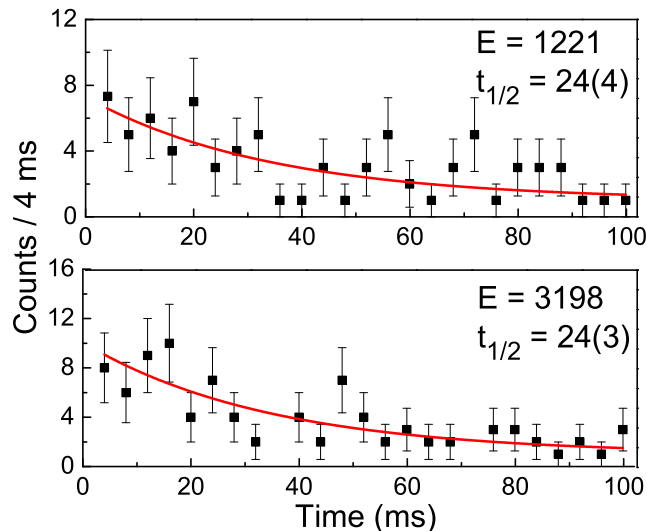


Figure 4.8: Two gamma gated half-lives from the  $^{22}\text{N}$  beta decay with gamma-ray energies in keV and the gated half-life in ms.

belong to the gamma-ray decay in  $^{21}\text{O}$ , was identified in this work. The gamma-rays at 881, 1845, 2133, 3026 and 3070 keV presented in the gamma-ray decay scheme of  $^{21}\text{O}$  [21] were not visible. However, the observed gamma-ray at 2129 keV, which matched with the 2133 keV energy within uncertainties, was assigned to the beta decay of  $^{23}\text{F}$  based on the relative intensity ratios in the same decay. The 1675 keV transition was identified as a gamma-ray in  $^{20}\text{O}$  as reported in Ref. [21, 34]. There were no other reported gamma-rays related to the  $^{20}\text{O}$  gamma-ray decay scheme were observed. Decay curves in coincidence with gamma-rays at 1221 and 3198 keV, given in Figure 4.8, yielded an average half-life of 24(3) ms which is consistent with the literature value for  $^{22}\text{N}$  beta decay [19]. The decay curve gated by the 1675 keV transition could not be evaluated due to poor statistics.

#### 4.1.4 Beta Decay Scheme of $^{22}\text{N}$

The beta decay scheme of  $^{22}\text{N}$  determined from the present work is shown in Figure 4.9. The following presents the neutron and gamma-ray assignments to establish this decay scheme. The gated decay curve analysis on the neutron time-of-flight spectrum showed six neutron peak with energies at 763, 1021, 1498, 1845, 2370 and 5176 keV had half-lives consistent with the beta decay of  $^{22}\text{N}$ . In addition, the gamma-ray

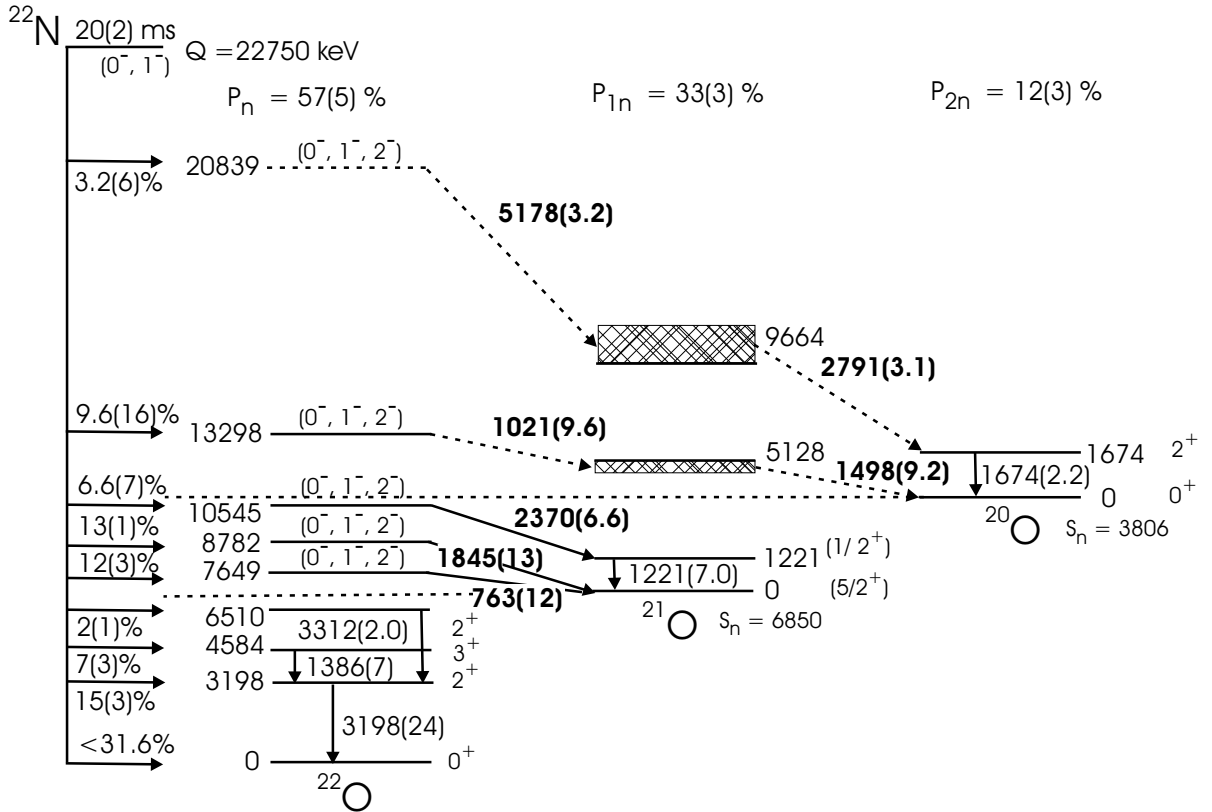


Figure 4.9: Beta decay scheme of  $^{22}\text{N}$ . The average half-life in ms, which was deduced from all neutron and gamma-ray gated half-lives, single and two neutron emission probabilities are given. The neutron transitions shown with dashed arrows have uncertainties in their placements due to the possibility of interchange their assignments. The heights of the shaded boxes in  $^{20}\text{O}$  represents the limits that level can be varied due to the interchange of neutrons. The average energies of these levels are given. The transition probabilities for the neutrons and the gamma-rays are given in parenthesis with their energies in keV.

transitions at 1221, 1386, 1674, 3198 and 3312 keV were identified as belong to the  $^{22}\text{N}$  beta decay. The gamma-ray at 1221 keV, which has been placed to the level at 1221 in  $^{21}\text{O}$ , (see Table 4.4), was based on the knowledge of the gamma-ray decay scheme [21] of particular nucleus. This gamma-ray transition required the feeding of 7.0% from the total  $^{22}\text{N}$  beta decay based on the observed gamma-ray intensity. This requirement could be satisfied by the neutron transition of 2370 keV based on an intensity match, therefore, the 2370 keV neutron transition was tentatively assigned to the state at 10545 keV in  $^{22}\text{O}$  as shown in Figure 4.9. The analysis of the gamma-ray activities of  $^{21}\text{O}$  beta decay showed that the single neutron emission probability is 33(3)% for the  $^{22}\text{N}$  beta decay. This requires feeding of 26(3)% to the ground state of  $^{21}\text{O}$ . Note that the parent and daughter activities in this decay series were saturated during the 30 minute-long runs as showed in the simulation, hence, it was reasonable to determine the absolute emission probabilities from the daughter activity. The neutrons with energies 763 and 1845 keV were placed as depopulating levels at 7649 and 8782 keV in  $^{22}\text{O}$ , respectively. Such placement order is necessary to feed the ground state of  $^{21}\text{O}$  as they cannot fulfill any other intensity requirement of a state in  $^{22}\text{O}$ . The observation of a 1674 keV gamma-ray with an intensity of 2.2% in  $^{20}\text{O}$  suggested beta-delayed neutron decays to neutron unbound states in  $^{21}\text{O}$  which subsequently decay to  $^{20}\text{O}$  as shown in Figure 4.9. Note that the mass chain  $A = 20$  was not implanted. The energy levels of  $^{20}\text{O}$  are well-known from previous experiments [21, 34] and the observed 1674 keV gamma-ray was identified as depopulating the 1674 keV state in  $^{20}\text{O}$ . The difference of 9.8(4)% between the gamma-ray feeding to the ground state of  $^{20}\text{O}$  and the number of  $^{20}\text{O}$  beta decay events derived from daughter gamma-rays suggested some feeding to the ground state of  $^{20}\text{O}$ . Two neutrons with energies of 1021 and 1498 keV emitted in sequence match the feeding requirement to the ground state of  $^{20}\text{O}$  as they have the same neutron emission probability (9.6(16) and 9.2(10)%, respectively). The neutron triple coincidence events were not observed to establish the sequence. However, there were two possible ways to place these neutron

decays. One way was to assign the 1021 keV neutron as depopulating a 13298 keV state in  $^{22}\text{O}$  and place the 1498 keV neutron to a state at 5379 keV in  $^{21}\text{O}$ . The second way was the interchange the order of emission. The proposed energy of 5379 keV state in  $^{21}\text{O}$  would then be lowered by 501 keV while the energy of the proposed 13298 keV state in  $^{22}\text{O}$  would remain unchanged. The 5379 keV state in  $^{21}\text{O}$  is presented in Figure 4.9 as 5128 keV, which is the average energy of the above mentioned limits, and the uncertainty of the state is shown by the shaded box. Feeding to the state at 1674 keV in  $^{20}\text{O}$  was possible with the sequential emission of the 5178 keV neutron and one of the neutrons with energy 2791, 3274, or 4069 keV, since they have similar emission probabilities. However, the sequential neutron transitions of 5178 and 2791 keV were assigned to feed the 1674 keV state in  $^{20}\text{O}$  based on the available energy window. The 2791 and 5178 keV neutrons were assigned to the states at 8411 keV in  $^{21}\text{O}$ , and at 20839 keV in  $^{22}\text{O}$ , respectively. These assignments are also subject to an interchange of the order of emission, which would increase the energy of the proposed 8411 keV state by 2506 keV. The average energy of 9664 keV is represented the 8411 keV state in  $^{21}\text{O}$  in the figure and the uncertainty is shown by the shaded box. The summary of the neutron assignments is given in Table 4.4. In addition, the gamma-ray transitions with energies 1386, 3198 and 3312 keV were placed, as given in Table 4.4, in the  $^{22}\text{O}$  levels to be consistent with the previous work [21]. The beta-delayed gamma-gamma coincidence events were not useful for placement due to poor statistics.

Figure 4.9 shows decay to the single-neutron daughter,  $^{21}\text{O}$ , with a single neutron emission probability of 33(3)% and to the two-neutron daughter,  $^{20}\text{O}$ , with a two-neutron emission probability of 12(3)%. The total neutron emission probability ( $P_n$ ) for the beta decay of  $^{22}\text{N}$  was 57(5)% and was deduced by adding the weighted neutron emission probabilities of both daughters [ $P_n = 1P_{1n} + 2P_{2n}$ ]. The beta branching ratios given in Table 4.5 have been calculated by considering the intensity flow through the decay scheme. The transition probabilities for both neutrons and gamma-rays

Table 4.4: Assignments of gamma-ray and neutron energies for beta decay of  $^{22}\text{N}$ .

Gamma-ray energy (keV)	Emission probability (%)	Nuclide	Energy level(keV)
1386(4)	3.0(16)	$^{22}\text{O}$	4584
3198(8)	21(3)	$^{22}\text{O}$	3198
3312(5)	2(1)	$^{22}\text{O}$	6510
1221(3)	7.0(11)	$^{21}\text{O}$	1221
1674(3)	2.2(12)	$^{20}\text{O}$	1674
Neutron energy (keV)	Emission probability (%)	Nuclide	Energy level(keV)
763(1)	12(3)	$^{22}\text{O}$	7649
1845(4)	13(1)	$^{22}\text{O}$	8782
2370(6)	6.6(7)	$^{22}\text{O}$	10545
1021(2) <sup>1</sup>	9.6(16)	$^{21}\text{O}$	4878 <sup>2</sup>
5178(24) <sup>3</sup>	3.2(6)	$^{22}\text{O}$	20839
1498(3) <sup>1</sup>	9.2(10)	$^{22}\text{O}$	13298
2791(8) <sup>3</sup>	3.1(6)	$^{21}\text{O}$	8411 <sup>4</sup>

<sup>1</sup>The order of emission could be interchanged.

<sup>2</sup>This could terminate at the level at 5378 keV.

<sup>3</sup>The order of emission could be interchanged.

<sup>4</sup>This could terminated at the level at 10917 keV.

are given in parentheses following the transition energy. The energy levels shown in the shaded boxes represent the uncertainty introduced by the interchanging of the order of the sequential neutron emission. The neutron decay of the highest observed energy level in  $^{22}\text{O}$  has been displayed with dashed lines due to uncertainties in these assignments. The average half-life of 20(2) ms shown in Figure 4.9 was deduced from the neutron and gamma-ray gated decaycurves given above. The apparent  $\log(ft)$  values given in Table 4.5 were calculated as explained in Ref. [71] using the Q-value of 22750 keV [19], the half-life of 20 ms and the observed beta decay branching ratios. Five states in  $^{22}\text{O}$  were assigned negative parity while the observed neutron bound states were assigned positive parity based on the  $\log(ft)$  values and beta decay selection rules. The possible spins for the negative parity states are 0, 1 or 2 assuming allowed beta decays from the  $0^-$  or  $1^-$  ground state of  $^{22}\text{N}$  [48]. All bound states

Table 4.5: Properties of the  $^{22}\text{N}$  beta decay.

Energy level (keV)	Branch (%)	Log(ft)	Spin parity	B(GT)
0	< 31.6	5.82	$0^+$	0.006
3198	15(3)	5.79	$2^+$	0.006
4584	7(3)	5.95	$3^+$	0.004
6510	2(1)	6.24	$2^+$	0.002
7649	12(3)	5.30	$0^-, 1^-, 2^-$	0.020
8782	13(1)	5.26	$0^-, 1^-, 2^-$	0.022
10545	6.6(7)	5.08	$0^-, 1^-, 2^-$	0.033
13298	9.6(16)	4.52	$0^-, 1^-, 2^-$	0.12
20839	3.2(6)	1.67	$0^-, 1^-, 2^-$	84

observed in present work of  $^{22}\text{N}$  beta decay were known by several experimental work. The spins of the positive parity bound states in  $^{22}\text{O}$  should be 0, 1, 2 or 3 to satisfy the selection rules of the first forbidden decay. However the spins of the bound states, shown in Figure 4.9, were assigned based mostly on previous work. The spins and parities of the observed states in  $^{22}\text{O}$  are given in Table 4.5. The spins and parities for states in  $^{21}\text{O}$  and  $^{20}\text{O}$ , shown in Figure 4.9, were adopted from the literature [21, 34]. The Gamow-Teller strengths for beta decay to the observed states in  $^{22}\text{O}$  were calculated as explained in Chapter 2 and reported in Table. 4.5 for later comparison with shell model calculations.

## 4.2 Beta Decay of $^{25}\text{F}$

The largest contaminant of the implanted beam was  $^{25}\text{F}$ . The beta decay of  $^{25}\text{F}$  populates levels in  $^{25}\text{Ne}$ , which can provide indirect information on the existence of  $N = 16$  shell gap in the Ne isotopes. The shell structure of  $^{25}\text{Ne}$  has two valence protons in the  $0d_{5/2}$  orbital and one valence neutrons in the  $1s_{1/2}$  orbital. It has been argued that the assignment of  $1/2^+$  to the ground state of  $^{25}\text{Ne}$  with a negligible contribution from the  $0d_{3/2}$  orbital provides evidence a the large energy gap between the  $1s_{1/2}$  and  $0d_{3/2}$  single particle states [16, 72]. The recent measurement of  $^{25}\text{F}$

beta decay and comparison with USD shell model calculations by Padgett et al. [16] claimed the location of  $0d_{3/2}$  moves closer to the  $fp$  shell increasing the  $N = 16$  shell gap for the Ne isotopes. This work also showed a considerable discrepancy in the shell ordering between the experimental and the USD calculated energy levels for the first  $3/2^+$  and  $5/2^+$  states. However, it is important to accurately determine the energy states in  $^{25}\text{Ne}$  in order to understand the  $N = 16$  shell gap in the Ne isotopes.

The half-life and total neutron emission probability of the  $^{25}\text{F}$  beta decay were first reported to be 59(40) ms and 15(1)%, respectively, by Reeder et al. [39]. Another experiment was carried out using four Ge detectors and 42 He proportional counters by Reed et al. [63] and reported a half-life of 50(6) ms and a total neutron emission probability of 14(5)%. This work also reported four gamma-ray transitions of 574.7(5), 1613.4(12), 1702.7(7) and 2188.6(1.3) keV associated with three energy levels at 1702.7(7), 3316.1(14) and 3890.8(15) keV in  $^{25}\text{Ne}$ . The recent beta decay study by Padgett et al. [16] published three gamma-rays at 1234, 1622 and 2090 keV associated with energy levels at 2090 and 3324 keV in  $^{25}\text{Ne}$ . The half-life of 90(9) ms was reported in the same work, which is much longer than previously reported values except for the value of 70(10) ms measured by Penionzhkevich [62]. The reported total neutron emission probability of 23.1(4.5)% from the work of Padgett et al. is in reasonable agreement with the previous values. Although the average total neutron emission probability of 17% was reported from all measurements, the beta-delayed neutron energies leading to neutron unbound states are not known at present for the  $^{25}\text{F}$  beta decay.

The energy level structure of  $^{25}\text{Ne}$  was first investigated by Wilcox et al. [73] using the reaction  $^{26}\text{Mg}(^7\text{Li}, ^8\text{B})^{25}\text{Ne}$ . Five excited states up to 4.7(1) MeV was observed. Woods et al. [74] had studied the reaction  $^{26}\text{Mg}(^{13}\text{C}, ^{14}\text{O})^{25}\text{Ne}$  and measured four excited states in  $^{25}\text{Ne}$  including a level at 6.28(5) MeV, which is 2.7 MeV above neutron separation energy. A study based on a single step fragmentation experiment by Belleguic et al. [75] reported two cascading gamma-rays of 1617(5) and 1707(4)

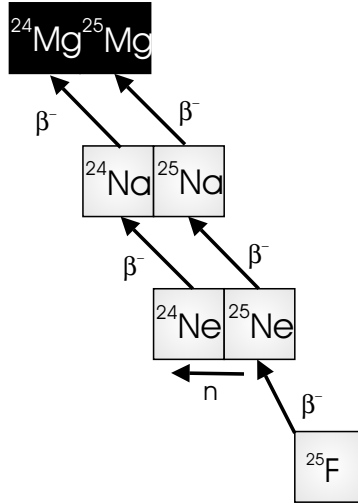


Figure 4.10: The  $^{25}\text{F}$  beta decay chain. Beta decay chains end with stable  $^{24}\text{Mg}$  and  $^{25}\text{Mg}$  shown in black squares.

keV associated with the 1707 and 3324 keV levels. The recent investigation using the direct one-neutron knockout reaction by Terry et al. [72] reported three gamma-rays corresponding to three energy levels in  $^{25}\text{Ne}$  with their spectroscopic factors. In addition, the spins and parities for the first three excited states in  $^{25}\text{Ne}$  have been assigned as  $5/2^+$ ,  $3/2^+$  and  $5/2^+$ , respectively. The ground state of  $^{25}\text{Ne}$  was reported to be  $1/2^+$  in all experiments. No neutron unbound states except the 6.28 MeV state and no negative parity states were observed in  $^{25}\text{Ne}$ .

The beta decay of  $^{25}\text{F}$  produces the beta decay  $A = 25$  daughter chain and the beta-delayed neutron  $A = 24$  daughter decay chain has shown in Figure 4.10. The variations in the activities during the experiment were checked by a decay model incorporating all decay chains under the experimental conditions similar to that for  $^{22}\text{N}$  discussed above. Details of the model and the method are given in the  $^{22}\text{N}$  experiment section and Appendix A. The simulated activity curves for nuclei in the  $^{25}\text{F}$  beta decay chains, shown in Figure 4.11, shows that all daughters and granddaughters reach their saturation activities within the first 400 s of the experiment. The input parameters for the simulation such as half-lives of all decays and the total neutron emission probability of  $^{25}\text{F}$  were taken from literature [19] and also are presented in

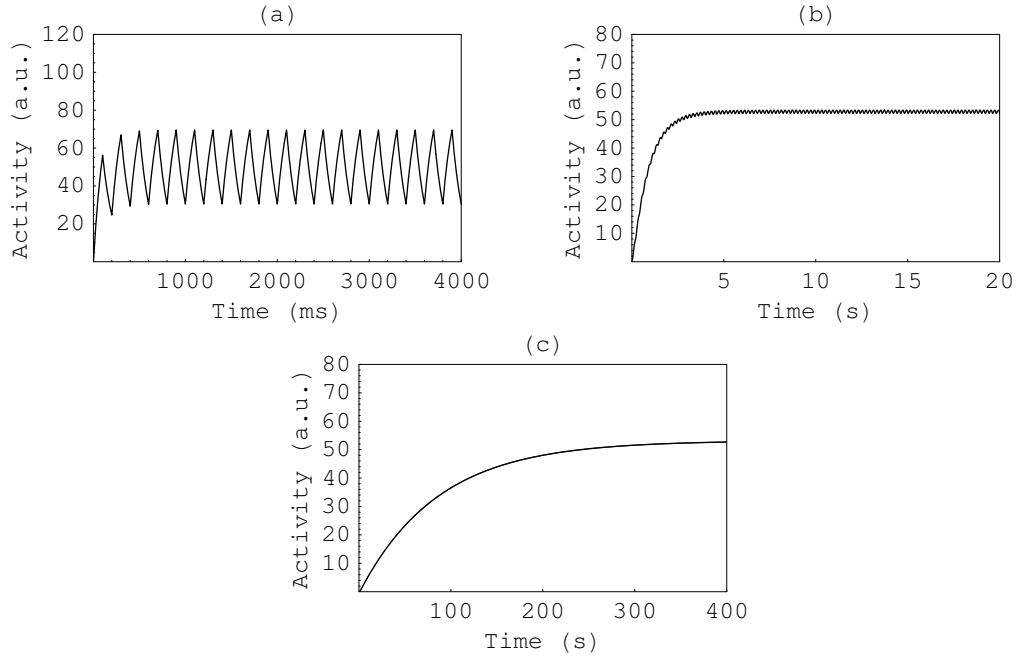


Figure 4.11: Growth and decay curves for the  $^{25}\text{F}$  decay series calculated using a decay model with a production rate of 100 pps for the parent of the decay series for (a)  $^{25}\text{F}$  activity curve, (b)  $^{25}\text{Ne}$  decay activity and (c)  $^{25}\text{Na}$  activity curve.

The beam on/off modes were also included in the calculations.

## Appendix.B.

The assignment of gamma-ray transitions to the  $^{25}\text{F}$  beta decay chains was performed based on the knowledge of those beta decays and the extracted half-lives from the gamma-ray gated decay curves. Gamma-rays with energies 87, 981, 1071 and 2203 keV were associated with the beta decay of  $^{25}\text{Ne}$  (see Figures 4.6 and 4.7). Gamma-rays at 386, 583, 976 and 1613 keV from transitions in  $^{25}\text{Mg}$  following the beta decay of  $^{25}\text{Na}$  were also present. The intensities of transitions agreed with previous measurements, thus confirming their assignments. In addition to the beta decay mass chain of  $A = 24$  introduced by the implantation of  $^{24}\text{O}$ , the beta-delayed neutron decay daughter chain of  $^{25}\text{F}$  also produced  $^{24}\text{Ne}$  and  $^{24}\text{Na}$  from subsequent beta decays. Therefore, the 1983 keV level in  $^{24}\text{Ne}$ , which is the only reported state in  $^{24}\text{Ne}$ , has two feeding pathways, namely, the direct beta decay of  $^{24}\text{F}$  generated from the  $A = 24$  mass chain and feeding from the beta-delayed neutron decay of  $^{25}\text{F}$ . In addition, the gamma-ray at 1983 keV from the  $^{24}\text{F}$  beta decay, 474 and 876 keV from the  $^{24}\text{Ne}$

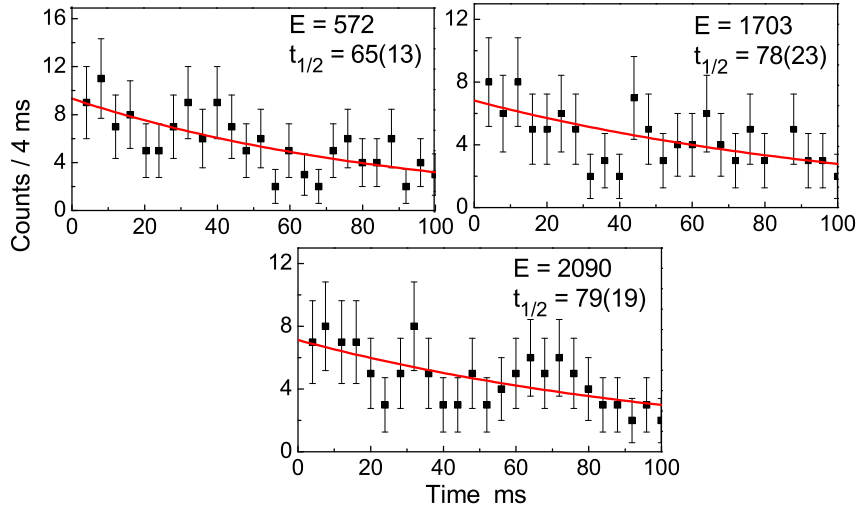


Figure 4.12: Gamma gated half-lives for the  $^{25}\text{F}$  beta decay. The gamma-ray energy in keV and the respective gated half-life in ms are given.

beta decay, and 1369 and 2756 keV from the  $^{24}\text{Na}$  beta decay were observed and are shown in Figures 4.6 and 4.7 confirming the  $A = 24$  decay chain. All gamma-ray energies, intensities and their decay assignments are given in Appendix B.

The 1703, 2090, 1616, 1236, 572 and 2187 keV gamma-ray transitions associated with the beta decay of  $^{25}\text{F}$  were observed in the present experiment, which reconfirms the observations reported in Ref. [16]. The gamma-ray gated decay curves displayed in Figure 4.12 were created for transitions that had reasonable statistics and were well resolved. The half-lives were determined from a fit using a single exponential decay constant and a flat background. The resulting half-lives were consistent with the literature values confirming their placement in the level scheme of  $^{25}\text{Ne}$ . The present work did not observe new gamma-rays associated with decay of  $^{25}\text{F}$  compared to the Padgett et al. work. Therefore, the gamma-ray decay in  $^{25}\text{Ne}$ , shown in Figure 4.13, was established to match the work of Padgett et al. Note that no beta-gamma-gamma coincidences were observed in present work. The assignments are summarized in Table 4.6 along with their gamma-ray emission probabilities.

The beta decay scheme of  $^{25}\text{F}$ , shown in Figure 4.13, was generated from all

Table 4.6: Gamma-ray and neutron energies assignments for the  $^{25}\text{F}$  beta decay.

Gamma energy (keV)	Emission probability (%)	Nuclide	Energy level(keV)
572(3)	12(2)	$^{25}\text{Ne}$	3889
1236(3)	7(2)	$^{25}\text{Ne}$	3326
1616(4)	11.2(38)	$^{25}\text{Ne}$	3315
1623(4)	10.6(38)	$^{25}\text{Ne}$	3326
1703(3)	31(5)	$^{25}\text{Ne}$	1703
2090(5)	25(4)	$^{25}\text{Ne}$	2090
2187(4)	5(2)	$^{25}\text{Ne}$	3889
1983(5)	19.4(20)	$^{24}\text{Ne}$	1983
Neutron energy (keV)	Emission probability (%)	Nuclide	Energy level(keV)
1212(2)	17(2)	$^{25}\text{Ne}$	7426

gamma-rays discussed above and the neutron transition identified from this work. The following will be discussed the neutron identification. The analysis of the neutron time-of-flight spectrum in the  $^{22}\text{N}$  experiment suggested that the neutrons with energies 1212, 3274 and 4069 keV could originate from  $^{25}\text{F}$  or  $^{24}\text{O}$ , as they could not be assigned to the  $^{22}\text{N}$  beta decay. The high uncertainty of the neutron gated half-life of 68(16) ms for the 1212 keV neutron could match the half-lives of either  $^{25}\text{F}$  or  $^{24}\text{O}$ . However, the assignment to  $^{25}\text{F}$  was based on the intensity requirement for the  $^{25}\text{F}$  beta decay neutron daughter branch from the independent gamma-ray measurements. The only known state at 1983 keV in  $^{24}\text{Ne}$  [76, 63, 16] can be populated either by the decay of  $^{24}\text{F}$  (100% of beta goes to this state), the daughter of  $^{24}\text{O}$ , or by delayed neutrons from  $^{25}\text{F}$  decay. The contribution from the  $^{24}\text{F}$  beta decay to the 1982 keV state in  $^{24}\text{Ne}$  was reasonably well known from the neutron emission probability of  $^{24}\text{O}$  (see the beta decay of  $^{24}\text{O}$ ). The feeding requirement to this state from the beta-delayed neutron decay of  $^{25}\text{F}$  has been calculated by taking the difference between the total number of observed 1982 keV gamma-rays and the contribution from the beta decay of  $^{24}\text{O}$ . Moreover, the neutron feeding was also calculated independently from the gamma-ray activities of  $^{25}\text{Ne}$ , which agreed within uncertainty with the above calculation. By considering both values, the average total neutron

emission probability of the  $^{25}\text{F}$  was found to be 19(2)% from the gamma-ray activity analysis. This value agreed with neutron emission probability of 17(2)% for the 1212 keV neutron energy group and with all reported  $P_n$  values within uncertainties [16]. Combinations of other neutron paths were considered but they failed to satisfy the feeding requirement by the state at 1983 keV in  $^{24}\text{Ne}$ . Therefore, the neutron energy of 1212 keV depopulates the neutron unbound new state of 7426 keV in  $^{25}\text{Ne}$  as given in Table 4.6 and Figure 4.13.

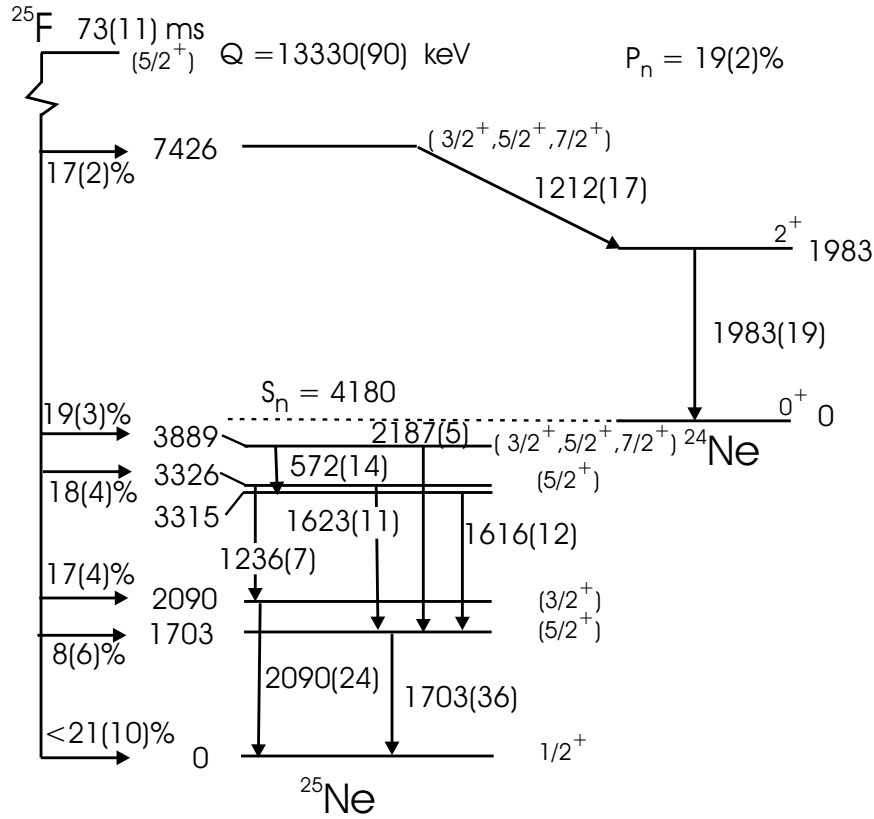


Figure 4.13: Beta decay scheme of  $^{25}\text{F}$ .

The beta branching ratios were deduced by considering the intensity sum rules. The apparent  $\log(ft)$  values, given in Table 4.7, were deduced using the method described in Ref. [71] along with the reported Q value of 13.33(9) MeV and the average half-life of 73(11) ms deduced from all gated decay curves related to the  $^{25}\text{F}$  beta decay. The spins and parities for the observed excited states were assigned based on the beta decay selection rules assuming the spin and parity of the ground state

Table 4.7: Properties of the  $^{25}\text{F}$  beta decay.

Energy level (keV)	Branch (%)	Log(ft)	Spin parity	B(GT)
0	<21(10)	<5.36	$1/2^+$	>0.017
1703	8(6)	5.48	$5/2^+$	0.013
2090	17(4)	5.08	$3/2^+$	0.033
3315	0	-	-	-
3326	18(4)	4.80	$5/2^+$	0.062
3889	19(3)	4.65	$3/2^+, 5/2^+, 7/2^+$	0.088
7426	17(2)	3.72	$3/2^+, 5/2^+, 7/2^+$	0.75

of  $^{25}\text{F}$  to be  $5/2^+$ . Five allowed beta decay transitions were observed along with a new neutron unbound state at 7426 keV. The spins and parties for states at 1703, 2090 and 3326 keV given in Table 4.7 were independently assigned and reconfirm the values given by the works of Padgett et al. and Terry et al.. An upper limit of the beta decay feeding to the ground state of  $^{25}\text{Ne}$  was determined by taking the difference between the number of  $^{25}\text{Ne}$  beta decay events deduced from the corresponding gamma-ray activities, and number of gamma-rays feeding from the excited states to the ground state. The B(GT) values, given in Table 4.7, for the observed beta decay transitions were calculated as explained in Chapter 2 for later comparison with shell model calculations.

### 4.3 Beta Decay of $^{24}\text{O}$

$^{24}\text{O}$  was one of the contaminants that was implanted during the  $^{22}\text{N}$  experiment. The beta decay of  $^{24}\text{O}$  heads the decay mass chain of  $A = 24$  and has a beta-delayed neutron daughter in the mass chain  $A = 23$ , shown in Figure 4.14. The daughter  $^{24}\text{F}$  decays to the  $^{24}\text{Ne}$  granddaughter and subsequently, to the great-granddaughter  $^{24}\text{Na}$ . Finally,  $^{24}\text{Na}$  decays to the stable nucleus  $^{24}\text{Mg}$ . In the case of the beta-delayed neutron daughter chain, stable  $^{23}\text{Na}$  nuclei are produced from subsequent decays of  $^{23}\text{F}$  and  $^{23}\text{Ne}$ . The activity of nuclei originating from the  $^{24}\text{O}$  decay chain during the first 1000 s period of the experimental run were simulated to check whether they

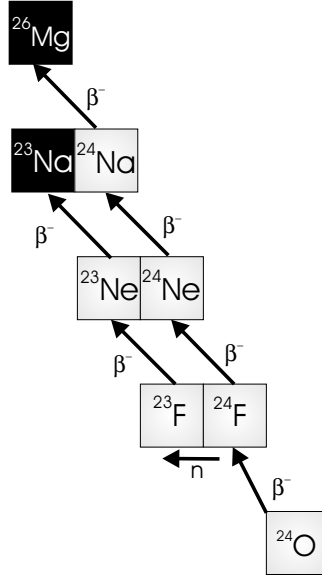


Figure 4.14:  $^{24}\text{O}$  beta decay chain. The stable isotopes are shown in solid squares.

become saturated using the model described in Appendix A. The simulation used the half-lives of all beta decays in the  $^{24}\text{O}$  decay chain as given in Appendix A. Figure 4.15 shows the activity build up of  $^{24}\text{O}$ ,  $^{24}\text{F}$  and  $^{24}\text{Ne}$  obtained from the simulation with a production rate of 100 pps for  $^{24}\text{O}$ . The activities become saturated after 1000 s. The results from the simulation assured that the daughter gamma-rays could be used to extract absolute gamma-ray intensities.

The heaviest bound oxygen isotope,  $^{24}\text{O}$ , beta decays to  $^{24}\text{F}$  thus allowing the study of the structure of  $^{24}\text{F}$  that has very little known information. The beta decay of  $^{24}\text{O}$  was first studied by Mueller et al. [10] using a  $4\pi$  neutron detector in coincidence with a Si(Li) beta detector. They reported a half-life of  $61_{-19}^{+32}$  ms and a total neutron emission probability of 58(12)%. In contrast to this measurement, Reed et al. [63] obtained 65(5) ms and 18(6)% for the half-life and the total neutron emission probability, respectively, from an experiment that implanted 9000  $^{24}\text{O}$  ions in a Si telescope at GANIL. The gamma-rays were measured with four large Ge detectors and neutrons with 42 He proportional counters. Although the half-lives agreed within uncertainties, the total neutron emission probability has a large discrepancy. Three gamma-ray transitions with energies 521.5(3), 1309.5(5) and 1831.6(5) keV associated

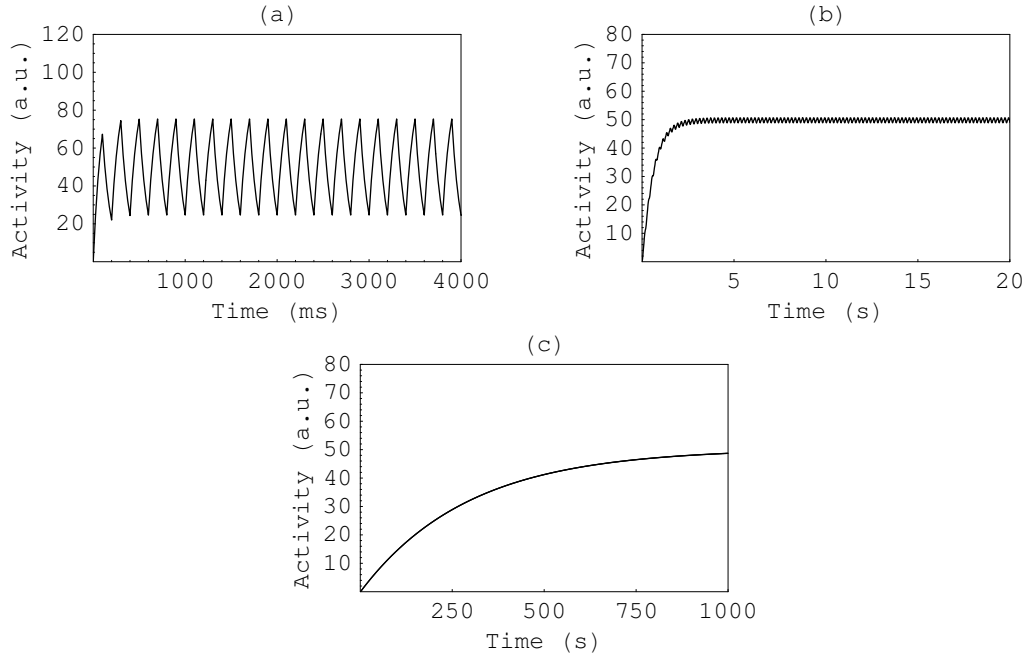


Figure 4.15: Growth and decay curves for the  $^{24}\text{O}$  decay series were calculated using a decay model with a production rate of 100 pps for the parent of the decay series for (a)  $^{24}\text{O}$  activity curve, (b)  $^{24}\text{F}$  activity curve and (c)  $^{24}\text{Ne}$  activity curve. The beam on/off modes are included to the calculation.

with the 522 and 1832 keV levels in  $^{24}\text{F}$  were reported by Reed et al. and it is the only information on excited states in  $^{24}\text{F}$ . The spins and parities of  $2^+$  and  $1^+$  have been assigned to the 522 and 1832 keV states, respectively, based on comparison with shell model predictions. In addition, the shell model calculations using the USD, SDPOTA and CW(Chung and Wildenthal) interactions predicted other  $0^+$  and  $1^+$  states in  $^{24}\text{F}$  in addition to the previously reported states, such low spin states with positive parities favored by allowed beta decay, but were not observed in the previous work. Gamma-rays from these states might be observed in the present experiment because the states are expected below the neutron separation energy.

The beta-gamma coincidence spectra from  $^{22}\text{N}$  cocktail beam are shown in Figures 4.6 and 4.7, where the gamma-ray peaks are labeled by their parent nuclei. As explained in the analysis of the  $^{25}\text{F}$  beta decay, gamma-rays associated with beta decays of  $^{24}\text{F}$ ,  $^{24}\text{Ne}$  and  $^{24}\text{Na}$  were observed, and the energies and intensities are given in Appendix B. Seven gamma-rays attributed to  $^{23}\text{F}$  decay and a single gamma-ray

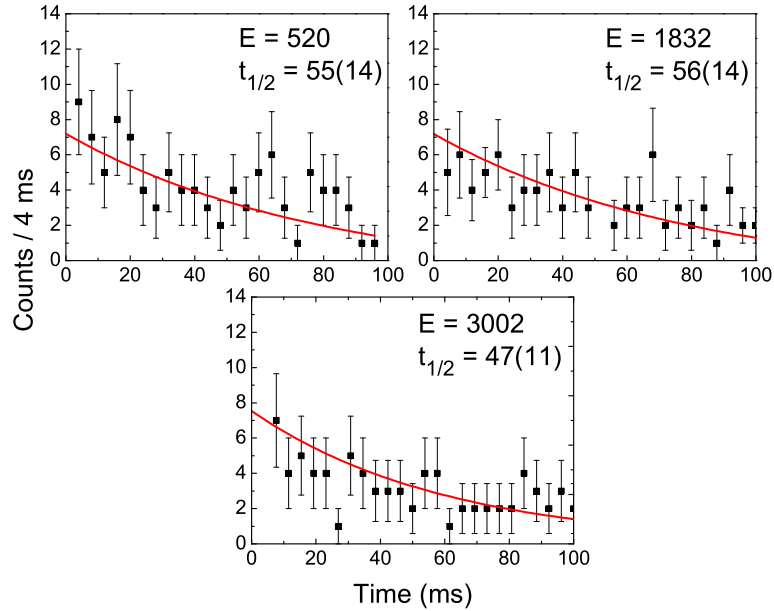


Figure 4.16: Gamma gated decay curves of the  $^{24}\text{O}$  beta decay. The gamma-ray energies in keV and the gated half-lives in ms are shown.

at 439 keV from  $^{23}\text{Ne}$  decay were identified thus confirming the beta-delayed neutron daughter chain of  $^{24}\text{O}$ , since the  $A = 23$  mass chain was not implanted. The reported 520, 1312 and 1832 keV gamma-ray transitions in  $^{24}\text{F}$  have been observed in the present study and the assignment of the 520 and 1832 keV transitions to the decay of  $^{24}\text{O}$  was confirmed by half-life results from the gated decay curves shown in the top panels of Figure 4.16. A new gamma-ray transition with energy 3002 keV in  $^{24}\text{F}$  was also identified based on the half-life obtained from the gated decay curve in Figure 4.16. A single weak gamma-ray at 2243 keV, which could be associated to gamma-ray decay in  $^{23}\text{F}$  known from our experiment using  $^{23}\text{O}$  cocktail beam (see analysis of  $^{23}\text{O}$  beta decay) was observed in present work. However, the peak at 2243 keV might also be the single escape peak of an intense gamma-ray at 2754 keV produced from the beta decay of  $^{24}\text{Na}$ . The peak was assigned to  $^{23}\text{F}$ . The observed gamma-ray emission probabilities for observed gamma-rays are given in Table 4.8.

The tentative beta decay scheme of  $^{24}\text{O}$  is shown in Figure 4.17. The level assign-

Table 4.8: Gamma-ray and neutron energies assignments for the beta decay of  $^{24}\text{O}$

Gamma energy (keV)	Emission probability (%)	Nuclide	Energy level(keV)
520(3)	14(4)	$^{24}\text{F}$	520
1312(5)	13(5)	$^{24}\text{F}$	1832
1832(4)	30(5)	$^{24}\text{F}$	1832
3002(6)	14(4)	$^{24}\text{F}$	3002
Neutron energy (keV)	Emission probability (%)	Nuclide	Energy level(keV)
3274(10)	12(2)	$^{24}\text{F}$	9515
4069(15)	11(2)	$^{24}\text{F}$	8102

ments for the observed gamma-rays in  $^{24}\text{F}$  were based on the knowledge of gamma-ray decay in  $^{24}\text{F}$  from the work of Reed et al. [63] and comparison to a shell model calculation given in the same work. The new gamma-ray at 3002 keV was attributed tentatively to a new state at 3002 keV in  $^{24}\text{F}$ . This new assignment fills in the previously missing allowed beta decay to a state at 3000 keV predicted by shell model calculations using the CW interaction, which has good agreement with the other observed states.

The analysis of the neutron time-of-flight spectrum for implantation during the  $^{22}\text{N}$  experiment revealed six neutrons energies that assigned to the beta decay of  $^{22}\text{N}$  and a 2730 keV neutron attributed to the same decay ( $^{22}\text{N}$ ) based on the intensity flow arguments and available beta decay energy window in  $^{22}\text{O}$ . The neutron with energy 1212 keV was assigned to the  $^{25}\text{F}$  beta decay. The two remaining unassigned neutrons were candidates for the beta decay of  $^{24}\text{O}$  since they did not satisfy intensity sum rules in either  $^{22}\text{N}$  or  $^{25}\text{F}$  beta decays. The gated decay curves for these neutrons did not produce half-lives due to low statistics. The neutron emission probabilities of the 3274 and 4069 keV neutrons were found to be 13(2)% and 11(2)%, respectively, with respect to the total number of  $^{24}\text{O}$  beta decay events. However, the gamma-ray activity of  $^{23}\text{F}$  beta decay required 39(8)% feeding to the ground state of  $^{23}\text{F}$ . Since  $^{23}\text{F}$  was not implanted, this feeding had to be fulfilled by beta-delayed neutron decay of  $^{24}\text{O}$ . The gamma-rays associated with the energy levels in  $^{23}\text{F}$  were not observed as discussed

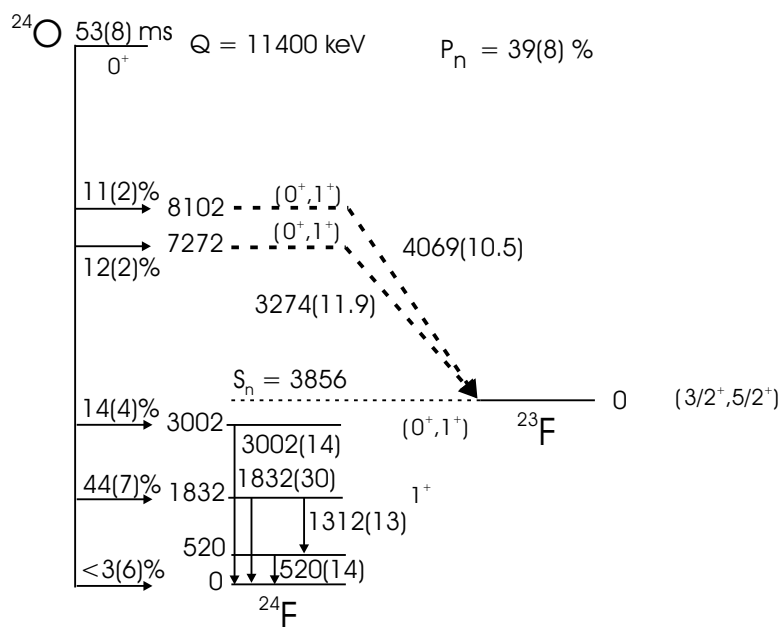


Figure 4.17: Beta decay scheme of  $^{24}\text{O}$ . The transition energies in keV and emission probabilities in parenthesis are given close to the arrow representing the transition. The tentative assigned neutron transitions and their states are displayed in dashed lines.

above. Hence, both neutrons have been placed to feed the ground state of  $^{23}\text{F}$  as shown in Figure 4.17. The neutrons with energies 3274 and 4069 keV depopulate levels at 7272 and 8102 keV states in  $^{24}\text{F}$ , respectively. In addition to these states, the decay associated with the neutron unbound states that were not observed in this experiment was 16% of the total decay, which was estimated from the feeding and decay of the  $^{24}\text{F}$  ground state.

The total neutron emission probability of the  $^{24}\text{O}$  decay was found to be 39(8)% from the gamma-ray activity in  $^{23}\text{Ne}$ , the decay of beta-delayed neutron daughter. The beta branches, shown above the horizontal arrows in Figure 4.17, were calculated to satisfy the feeding requirements of each state. The upper limit of the beta branch to the ground state of  $^{24}\text{F}$  was calculated as 3(6)% by considering the total neutron emission probability and the beta decay feeding to the neutron bound states in  $^{24}\text{F}$ . The state at 520 keV in  $^{24}\text{F}$  had no feeding within the uncertainties. The transition energies with their emission probabilities in parenthesis are also given in the same figure for both gamma-rays and neutrons. The apparent  $\log(ft)$  values and  $B(\text{GT})$

Table 4.9: Properties of the  $^{24}\text{O}$  beta decay.

Energy level (keV)	Branch (%)	Log(ft)	Spin parity	B(GT)
0	<3(6)	>5.71	$0^+, 1^+$	>0.008
520	0	-	-	-
1832	44(7)	4.15	$1^+$	0.28
3002	14(4)	4.38	$0^+, 1^+$	0.28
7272	11(2)	3.00	$0^+, 1^+$	4.0
8102	12(2)	2.61	$0^+, 1^+$	9.7
>3856	<16(4)	-	-	-

values, given in Table 4.9 were calculated as explained in previous sections. The beta feeding to all observed excited states were categorized as allowed beta decay based on the apparent  $\log(ft)$  values, and except for the 1832 keV state, were tentatively assigned spins and parities of  $0^+$  or  $1^+$  assuming that the ground state of  $^{24}\text{O}$  is  $0^+$ . The 1832 keV state was given a  $1^+$  to be consistent with the work of Reed et al. and the shell model calculations. The spin and parity for the ground state of  $^{24}\text{F}$  was not given as the feeding is negligible.

#### 4.4 Analysis of $^{23}\text{O}$ Beta Decay Experiment

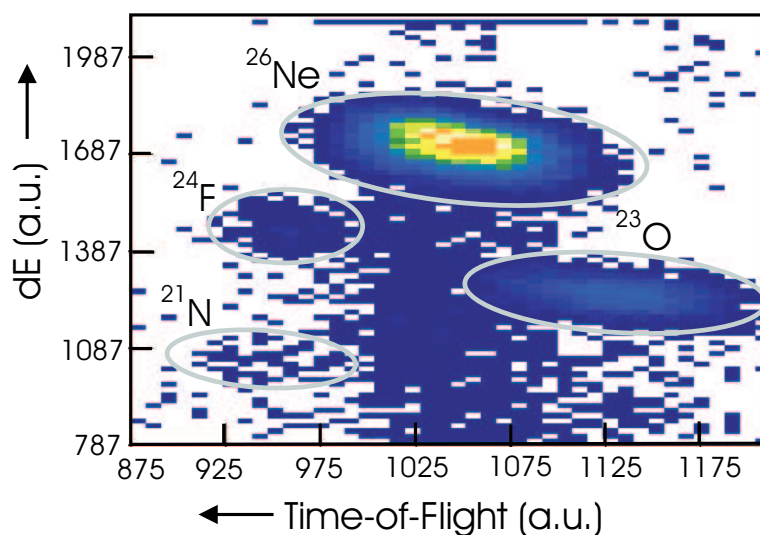


Figure 4.18: The identification of implanted nuclides. The identified particles from the  $^{23}\text{O}$  cocktail beam are labeled.

Table 4.10: Beam purity of the  $^{23}\text{O}$  experiment from the A1900 and the implantation detector.

Nuclide	A1900 Purity <sup>1</sup> (%) <sup>2</sup>	Implantation Detector Purity <sup>3</sup> (%)	Literature half-life <sup>4</sup> (ms)
$^{23}\text{O}$	16.8	14.2	82(37)
$^{26}\text{Ne}$	62.2	83.1	192(6)
$^{24}\text{F}$	7.4	2.1	400(50)
$^{21}\text{N}$	1.5	0.6	85(7)

<sup>1</sup>At the A1900 focal plane from the TOF and energy loss measurement.

<sup>2</sup> $^{25}\text{F}$ ,  $^{27}\text{Ne}$ ,  $^{10,11,12,13}\text{Be}$ ,  $^{7,8,9}\text{Li}$  and  $^6\text{He}$  contribute to the remaining 12.1%.

<sup>3</sup>Taken from the difference in counts from the dE and Veto detectors.

<sup>4</sup>Taken from Ref. [19].

The secondary beam of  $^{23}\text{O}$  was produced by fragmentation of a 140 MeV/A  $^{48}\text{Ca}$  beam with the same target and wedge as in the  $^{22}\text{N}$  experiment, but the settings of the A1900 magnets were change to optimize  $^{23}\text{O}$ . The beam was analyzed for purity at the focal plane of the A1900 before the implantation runs. The secondary beam from the A1900 separator was a cocktail beam consisting of  $^{23}\text{O}$ ,  $^{26}\text{Ne}$ ,  $^{24}\text{F}$  and  $^{21}\text{N}$  as major constituents, and  $^{25}\text{F}$ ,  $^{27}\text{Ne}$ ,  $^{10,11,12,13}\text{Be}$ ,  $^{7,8,9}\text{Li}$  and  $^6\text{He}$  as minor constituents. The percentage compositions of the beam at the focal plane of the A1900 are given in Table 4.4. A part of particle identification spectrum generated using the dE detector is shown in Figure 4.18, where major constituents are labeled and the light particles are not shown. The purity of the implanted beam, also given in Table 4.4, was deduced by applying gates on particle identification plot and taking the difference in counts between the dE and Veto detectors. The implanted beam consisted of only  $^{23}\text{O}$ ,  $^{26}\text{Ne}$ ,  $^{24}\text{F}$  and  $^{21}\text{N}$ . The reported half-lives for the implanted nuclei are given in the same table.

The beta decay of  $^{23}\text{O}$  produces the  $A = 23$  mass chain, which includes the daughter decay of  $^{23}\text{F}$  and the granddaughter  $^{23}\text{Ne}$  decay to the stable  $^{23}\text{Ne}$ . The beta-delayed neutron branch of  $^{23}\text{O}$  decay introduces the  $A = 22$  decay chain with

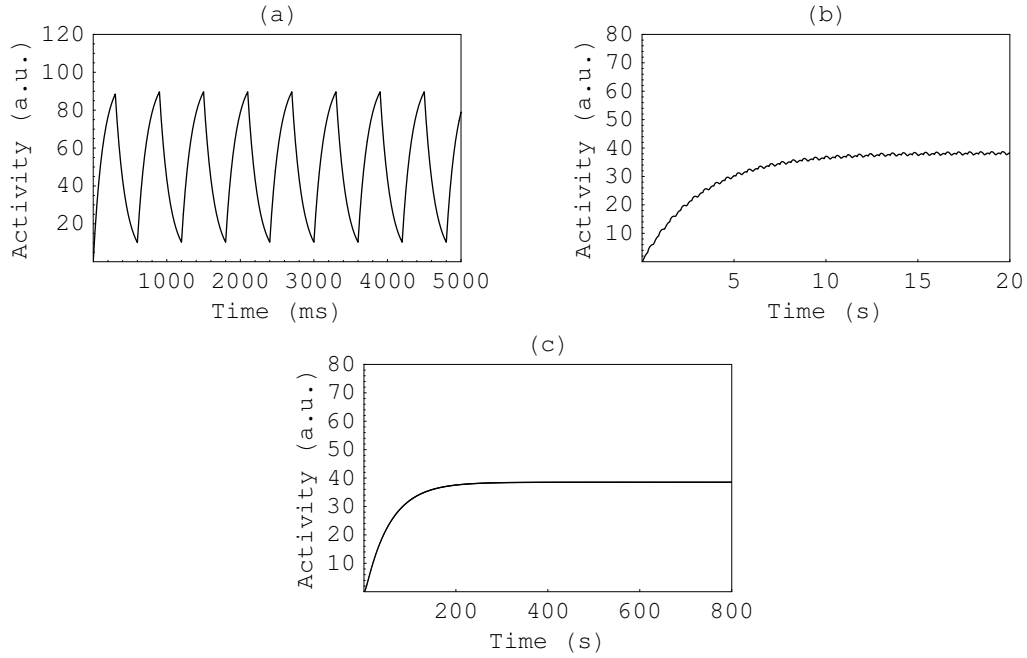


Figure 4.19: Growth and decay curves for the  $^{23}\text{O}$  decay series were calculated using a decay model with a production rate of 100 pps for the parent of the decay series for (a)  $^{23}\text{O}$  activity curve, (b)  $^{23}\text{F}$  activity curve and (c)  $^{23}\text{Ne}$  activity curve. The beam-on/off period of 300 ms are included to the calculation.

$^{22}\text{F}$  decay to the stable  $^{22}\text{Ne}$ . Figure 1.9 shows all decay chains for  $^{23}\text{O}$  beta decay. All of these decays could be observed in addition to the decays of the implanted impurity beta decay chains. The analysis of the beta decay of  $^{26}\text{Ne}$ , the major impurity in the implanted beam, will be given in a separate section.

The analysis of the  $^{23}\text{O}$  beta decay data for determining absolute transition intensities requires the knowledge of whether activities of daughters and granddaughters become saturated under the experimental conditions and were needed to determine the beta decay feeding contribution from directly implanted parent nucleus. The simulations were performed as explained in the section of the analysis of the  $^{22}\text{N}$  data. The Bateman equations [64] were written for the growth and decay of all decays during the beam-on/off periods. The detailed explanation of equations and the fitting function are given in Appendix A. The nuclei that did not decay during the beam-off period were added to the next cycle. The growth of the beta-delayed neutron decay chain was established by means of the neutron emission probabilities given in Ap-

pendix A. Figure 4.19 shows the simulated decay curves obtained for a production rate of 100 pps for  $^{23}\text{O}$ . The growth and decay of  $^{23}\text{O}$  during the first 5000 ms period of the experimental run is shown in Figure 4.19.(a) and the activity variations of  $^{23}\text{F}$  and  $^{23}\text{Ne}$  are shown Figure 4.19.(b) and (c), respectively. The simulation confirmed that  $^{23}\text{O}$  and the daughter activities were saturated after 200 s from the beginning of the experimental run.

#### 4.4.1 Total Number of Beta Decay Events

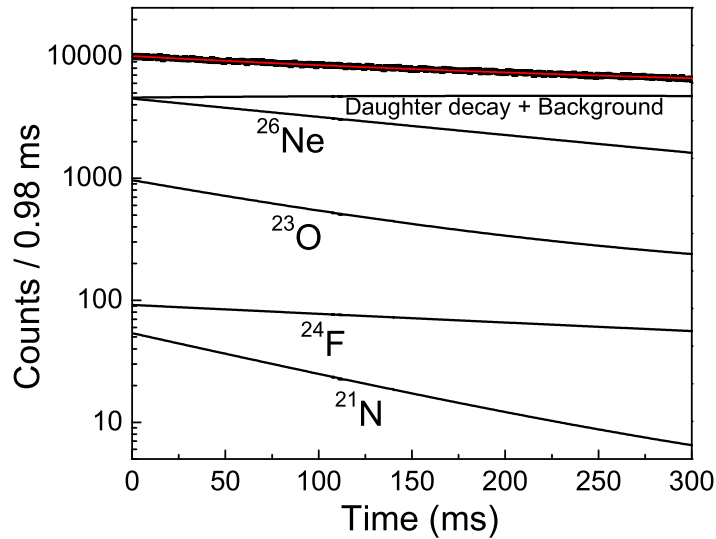


Figure 4.20: Ungated beta decay curve for the  $^{23}\text{O}$  experiment. The total fit to the decay curve, the individual decay components of the implanted  $^{26}\text{Ne}$ ,  $^{23}\text{O}$ ,  $^{24}\text{F}$  and  $^{21}\text{N}$ , and the background plus all decay contributions of daughters and granddaughters decay are shown.

The total number of beta decay events from a particular nucleus detected by the implantation detector was determined by integrating the beta decay curve. Beta decay events were time stamped from the start of beam-off period to produce an overall beta decay curve. This curve had contributions from the decays of all implanted nuclides and their decay series. The decay curve shown in Figure 4.20 was fitted with a function that describes the decays of all implanted nuclides and their decay chains

Table 4.11: Detected beta decay events from the  $^{23}\text{O}$  experiment

Nuclide	Total number of beta decay events	Half-life (ms)
$^{23}\text{O}$	$1.47(4)\times 10^5$	$102(23)^1$
$^{26}\text{Ne}$	$8.61(2)\times 10^5$	$192(4)^2$
$^{24}\text{F}$	$2.21(7)\times 10^4$	$384(16)^2$
$^{21}\text{N}$	$6.53(5)\times 10^3$	$85(14)^3$

<sup>1</sup>By fitting the decay curve, see the text.

<sup>2</sup>Gamma-ray gated half-lives from the present work.

<sup>3</sup>Taken from Ref. [76].

including the growth and decay during the beam-on and off periods. As explained in the analysis of the  $^{22}\text{N}$  experiment, a function was composed for each implanted decay series using the Bateman equations [64] for beam-off period and included the growth and decay contributions during the beam-on period. A detail explanation for the fitting function is given in Appendix A. The implantation purity ratios, taken from measurements in the dE and Veto detectors, were used to fix the initial activity ratios of the implanted isotopes. The half-lives of all daughters and granddaughters, and the half-life of  $^{21}\text{N}$ , which are reported in literature [19](see Appendix A), were kept constant through out the fitting procedure. The half-lives of  $^{26}\text{Ne}$  and  $^{24}\text{F}$ , which were deduced from the gamma-ray gated decay curves (see below) were also taken as fixed values. In addition, the neutron emission probabilities of  $^{24}\text{F}$  and  $^{21}\text{N}$  were also included by using the values of 5.9% and 81%, respectively, as reported in the literature [19]. Four parameters were left to vary: the half-life of  $^{23}\text{O}$ , the implantation rate of  $^{26}\text{Ne}$ , the neutron emission probability of  $^{23}\text{O}$  and a flat background. The individual contributions to the decay curve from each implanted nuclide are shown in Figure 4.20 with the total daughter and granddaughter contributions plus the background. The number of beta decay events extracted by integrating the individual components are given in Table 4.4.1 with half-life and their uncertainties taken from appropriate sources as cited. The half-life and  $P_n$  value for  $^{23}\text{O}$  were deduced to be  $102(23)$  ms and  $11(9)\%$ , respectively. The large number of activities present in the

detector does not allow more precise measurement of the half-lives in the bulk activity.

#### 4.4.2 Beta-delayed neutron time-of-flight measurement

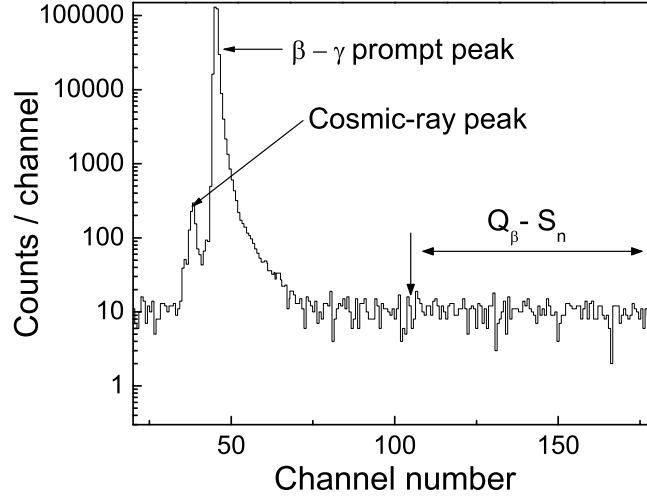


Figure 4.21: The beta-delayed neutron time-of-flight spectrum of  $^{23}\text{O}$  obtained by adding the data from all neutron detectors in the array. The peak due to cosmic-ray interaction with neutron detectors and the prompt peak are labeled. The upper limit of the beta decay energy window ( $Q_\beta - S_n$ ) to the neutron unbound states is indicated by the arrow.

The total neutron time-of-flight spectrum measured during the beam-off period and corrected for the constant-fraction discriminator (CFD) walk in all of the detectors in the neutron spectroscopic array is shown in Figure 4.21. The position of the prompt peak provided the time zero reference point for the time-of-flight spectrum. Cosmic-rays predominately propagate in the opposite direction through the detection system and trigger the electronics at a shorter time relative to the prompt peak to produce the cosmic-ray peak in Figure 4.21. No neutron peaks were observed within energy detection limits. The lower and upper energy detection limits are approximately 360 and 8000 keV, respectively. Since the energy window available for beta decay into the neutron unbound states is limited to 3750 keV (channel number 112), the energies of neutrons are well within the upper detection limit. It is possible

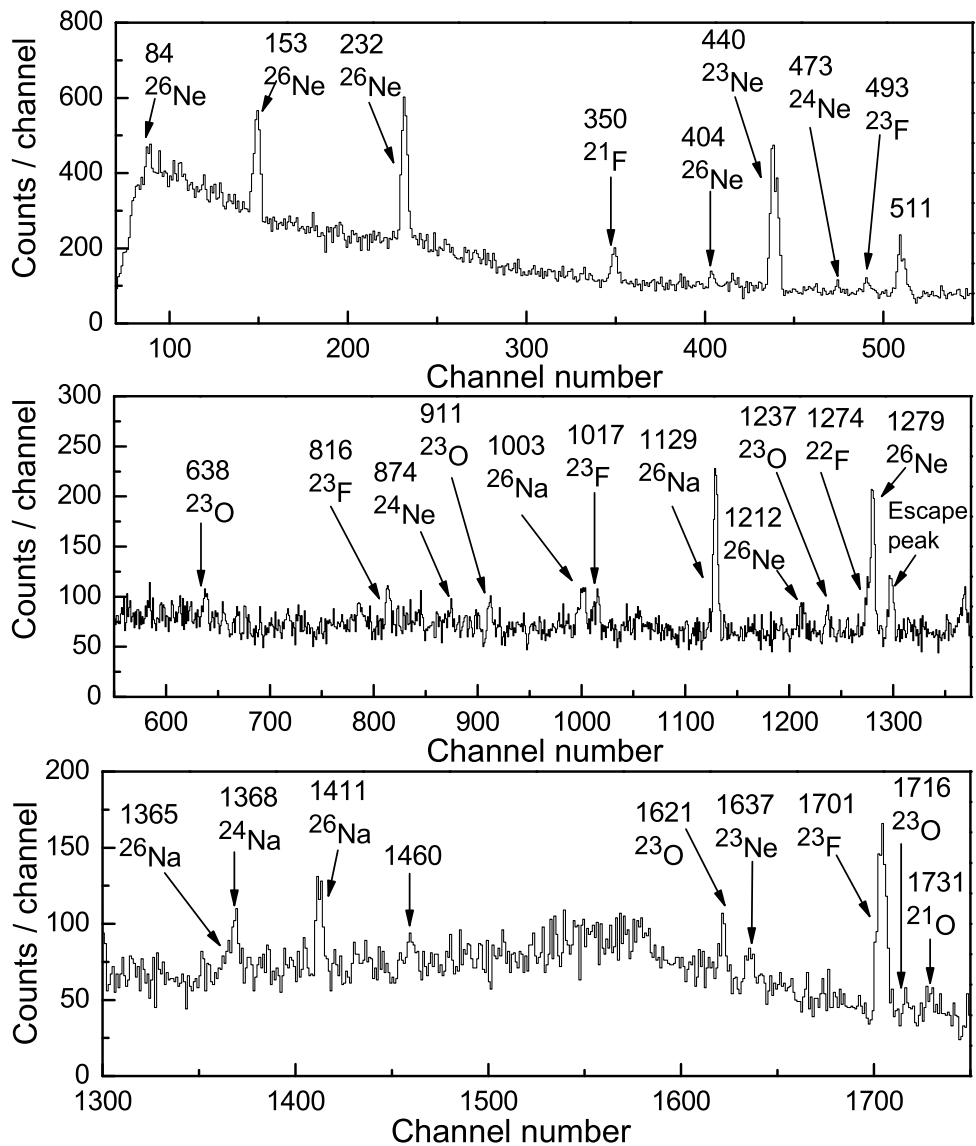


Figure 4.22: Beta-gamma coincidence spectrum for  $^{23}\text{O}$  experiment: Part I. The peaks are labeled with the parent nucleus and the energy in keV.

that low energy beta-delayed neutrons from the decay of  $^{23}\text{O}$  were below the lower energy detection limit of the neutron spectroscopic array or there are no neutron emission from this decay. To determine whether this could be the case, a search for the gamma-rays that originated from the beta-delayed neutron daughter decay was undertaken.

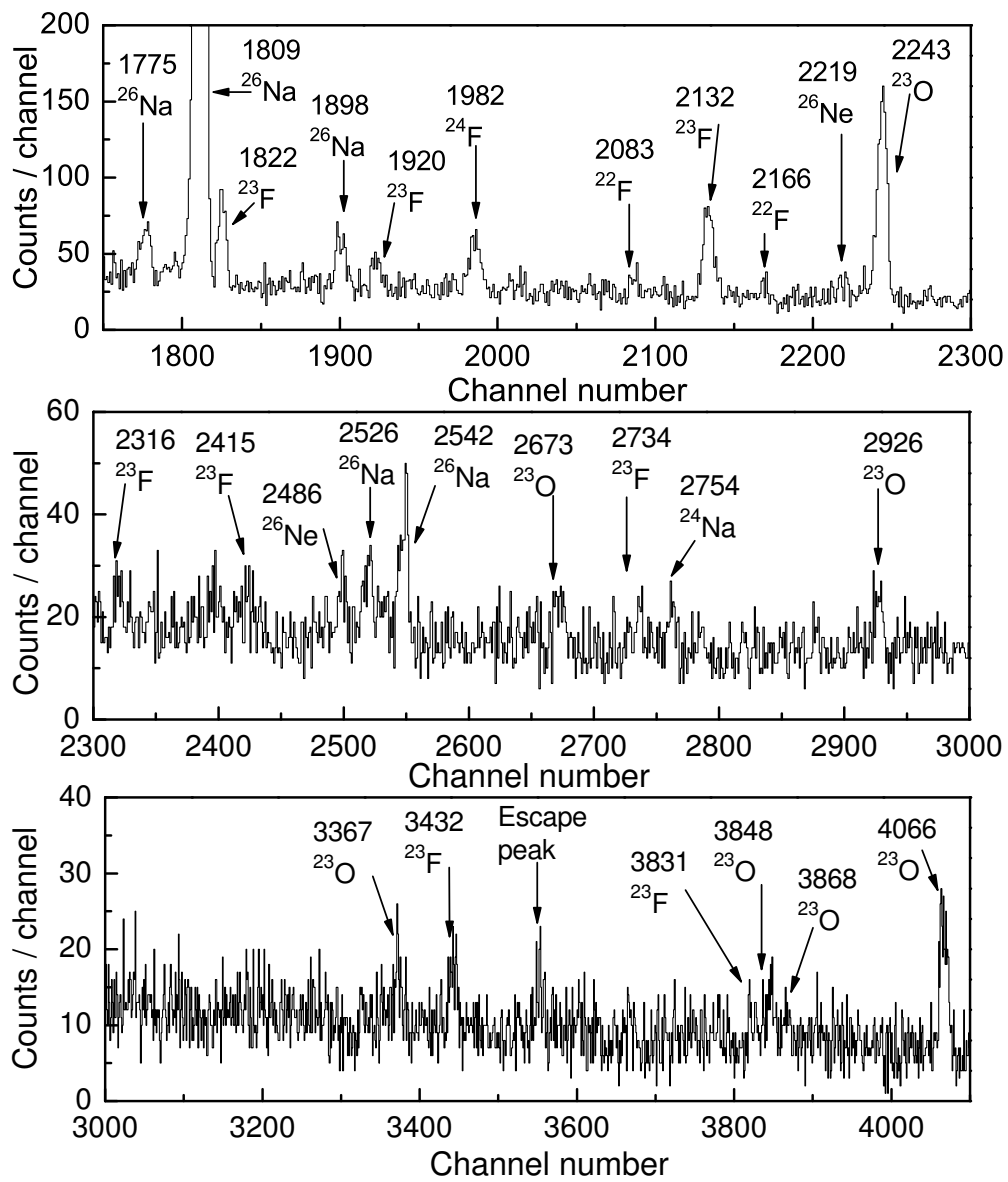


Figure 4.23: Beta-gamma coincidence spectrum for  $^{23}\text{O}$  experiment: Part II. The peaks are labeled with the parent nucleus and the energy in keV.

### 4.4.3 Beta-delayed gamma-ray measurement

Figures 4.22 and 4.23 show the total gamma-ray spectrum obtained in coincidence with the beta decay of the  $^{23}\text{O}$  cocktail during the beam-off period. The peaks are labeled with their assigned parent nucleus and energy in keV. The beta decay of  $^{23}\text{O}$  leads to the  $A = 23$  decay chain, which produces gamma-rays from decays of  $^{23}\text{F}$  and  $^{23}\text{Ne}$ . The gamma-ray transitions with energies 493, 816, 1017, 1701, 1822, 1920, 2132, 2316, 2415, 2734, 3432 and 3831 keV were assigned to the beta decay of  $^{23}\text{F}$  based on previous measurements [76]. The assignments were reconfirmed based on resulting half-lives from gamma-ray gated decay curves for those peaks that were statistically significant. Two gamma-rays from  $^{23}\text{Ne}$  beta decay, the granddaughter of  $^{23}\text{O}$ , were observed with energies 440 and 1637 keV and emission probabilities of 33.0% and 1.1%, respectively. These observations were in good agreement with literature values [76]. The gamma-ray transitions from the decay of the impurities in the cocktail beam, such as  $^{26}\text{Ne}$ ,  $^{24}\text{F}$  and  $^{21}\text{N}$ , and their daughters and granddaughters are shown and labeled in Figures 4.22 and 4.23. The gamma-ray transitions associated with the  $A = 26$  decay chain will be addressed separately below. In addition, a gamma ray with energies 1983 keV was assigned to the beta decay of  $^{24}\text{F}$ , which was also reported in Ref. [76]. The half-life extracted from the gamma-ray gated decay curve was 384(26) and confirms this assignment. A few gamma-rays from the  $A = 21$  decay chain determined in previous experiments are also shown and labeled in Figure 4.22.

Although beta-delayed neutrons from  $^{23}\text{O}$  were not observed, gamma-ray peaks associated with the beta decay of  $^{22}\text{F}$ , the beta-delayed neutron daughter of  $^{23}\text{O}$  were observed with energies 1274, 2083 and 2166 keV. These weak transitions had an intensity ratio of 5:4:3. This observation leads to the conclusion that at least one of the  $^{22}\text{F}$  states is populated by beta-delayed neutron decay of  $^{23}\text{O}$ , since nuclides with  $A = 22$  were not implanted during the experiment. Excited states in  $^{22}\text{F}$  were studied previously in beta decay of  $^{22}\text{O}$  [66], and the  $^{22}\text{Ne}(^3\text{He}, t)$  and  $^{22}\text{Ne}(^7\text{Li}, ^7\text{Be})$  reactions [77]. A weak gamma-ray at 638 keV associated with energy levels in  $^{22}\text{F}$  was

observed in present work. The known gamma-ray energy 72 keV attributed to  $^{22}\text{F}$  gamma-ray decay and expected to observe in cascade with a 638 keV transition was not seen here due to the threshold of the SeGA detectors. Although neutrons were not observed as discussed above, the observation of the  $A = 22$  decay chain and a weak transition in  $^{22}\text{F}$  indicate a total beta-delayed neutron emission probability at the level of 7(2)%, which was calculated from the total beta decay of  $^{22}\text{F}$  derived from the observed gamma-ray activities in  $^{22}\text{Ne}$ . Note that the parent and daughter activities in this decay series were saturated during the 30-minute long runs, as discussed in the previous section.

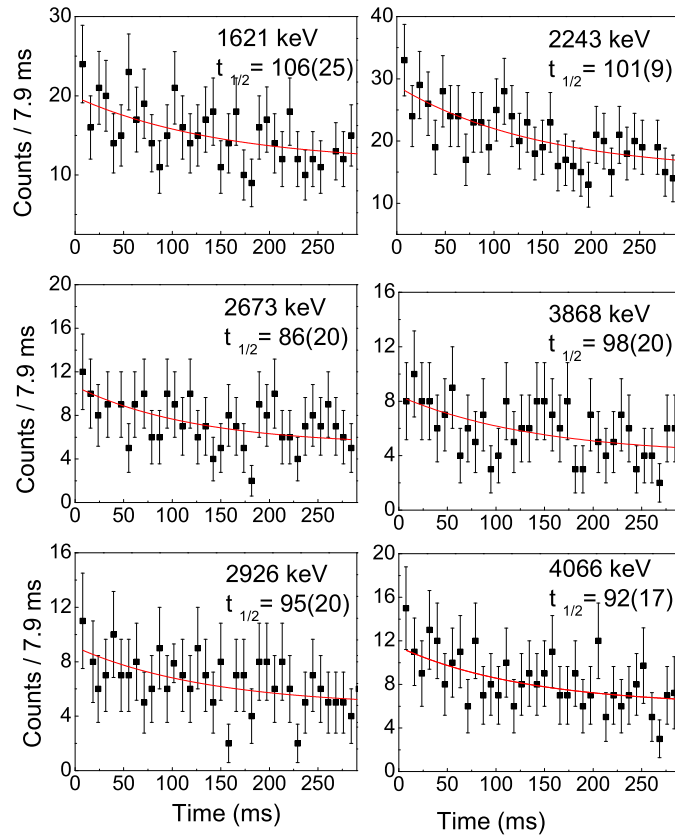


Figure 4.24: Gamma gated decay curves of  $^{23}\text{O}$ . The fitted single exponents are shown for the statistically significant peaks corresponding to beta decay of  $^{23}\text{O}$ . The gated gamma-ray peak energies and corresponding gated half-lives are given in keV and ms, respectively.

The relatively strong gamma-ray transitions with energies 1621, 2243, 2673, 2926,

Table 4.12: Gamma-ray assignment for the beta decay of  $^{23}\text{O}$ 

Gamma energy (keV)	Gated half-life (ms)	Emission Probability (%)	Nuclide	Energy level (keV)
911(4)	-	2.7(12)	$^{23}\text{F}$	3837
1237(4)	-	3.1(9)	$^{23}\text{F}$	4604
1621(6)	106(25)	5.7(10)	$^{23}\text{F}$	3866
1716(6)	-	2.1(6)	$^{23}\text{F}$	5553
2243(8)	101(9)	51.5(12)	$^{23}\text{F}$	2243
2673(9)	86(20)	5(1)	$^{23}\text{F}$	5599
2926(10)	95(20)	7(2)	$^{23}\text{F}$	2926
3367(13)	-	4.5(10)	$^{23}\text{F}$	3367
3868(15)	98(20)	10.1(16)	$^{23}\text{F}$	3866
4066(16)	92(17)	17.1(17)	$^{23}\text{F}$	4066
638(3)	-	1.5(8)	$^{22}\text{F}$	710

3868 and 4026 keV were assigned to the beta decay of  $^{23}\text{O}$ , which agree with previous work [37, 43]. The half-lives were obtained from gamma-ray gated decay curves by fitting a single exponential plus a flat background, as shown in Figure 4.24. The deduced half-lives gave a weighted average value of 97(8) ms. Although the half-life of  $^{21}\text{Na}$  is 85(7) ms, the above gamma-ray transitions cannot be attributed to the  $^{21}\text{Na}$  beta decay since the number of implanted  $^{21}\text{N}$  nuclei were not sufficient to produce such intense gamma-ray peaks. Four gamma-rays with energies 911, 1237, 1716 and 3367 keV were also attributed to the  $^{23}\text{O}$  beta decay based on the work of Belleguic et al. and Michimasa et al. [37, 43]. The transitions at 911, 1237, 1716 and 3367 keV also matched within uncertainties with the reported transitions in Refs. [37, 43]. Gamma-ray peaks at 2003, 3445, 3985 and 4732 keV reported in the nuclear reaction study were not observed in the present work.

#### 4.4.4 Beta Decay Scheme of $^{23}\text{O}$

The proposed beta decay scheme of  $^{23}\text{O}$  based on the observation from present work is shown in Figure 4.25 and the details of assignments will be discussed following. The assignment of gamma-rays to the energy levels in  $^{23}\text{F}$  was based on the previously known energy levels and gamma-ray transitions, since the beta-delayed gamma-

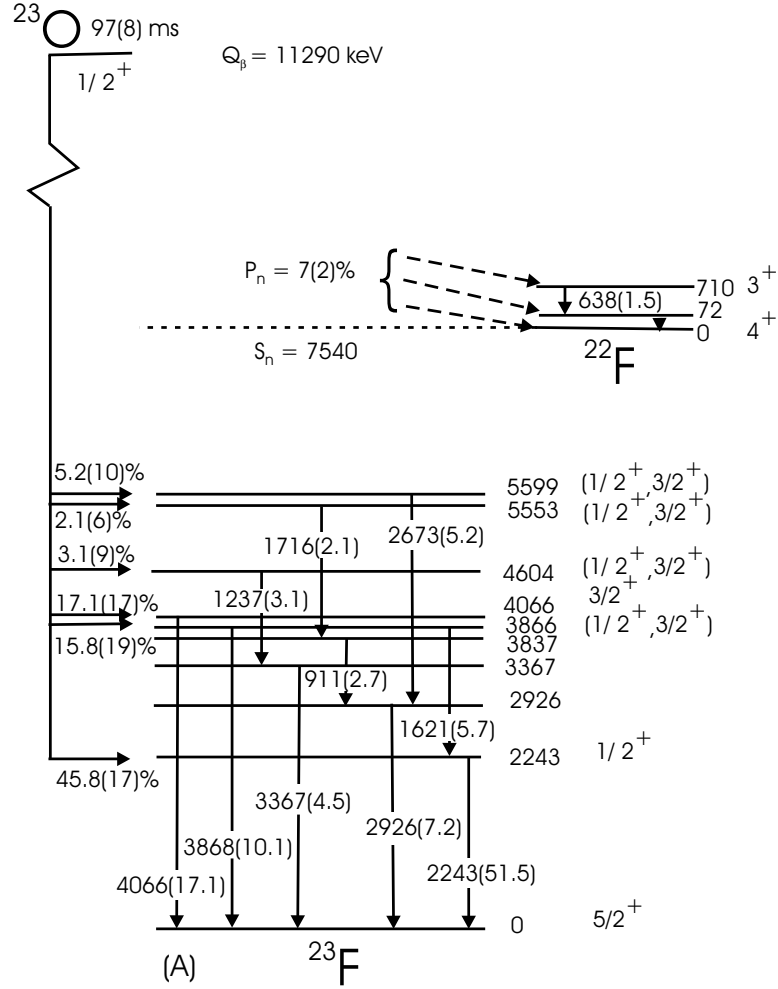


Figure 4.25: Beta decay scheme of  $^{23}\text{O}$ . The gamma-ray decay was given in vertical arrows with the transition energy and emission probabilities in parenthesis. The horizontal arrow shows the beta decay feeding to the level with the beta branch and the corresponding uncertainty in parenthesis.

gamma coincidence events were not evident due to poor statistics. The gamma-ray transition with energy 638 keV was placed to deexcite an energy level at 710 keV in the neutron daughter  $^{22}\text{F}$  following Ref. [77]. The gamma-ray transitions at 2243, 2926, 3367, 3868 and 4066 keV were assigned to feed the ground state of  $^{23}\text{F}$  as reported in Ref. [43] and shown in Figure 4.25. The gamma-rays of 912, 1237 and 2673 keV were placed to depopulate the known states at 3837, 4604 and 5599 keV, respectively, in order to be consistent with the gamma decay scheme in  $^{23}\text{F}$  as given in Ref. [43]. The gamma-ray with energy 1716 keV has been placed depopulating the known state at 5553 keV. This tentative placement is reasonable because it matches with the dif-

Table 4.13: Properties of the  $^{23}\text{O}$  beta decay.

Energy level (keV)	Branch (%)	Log(ft)	Spin parity	B(GT)
2243	47.8(17)	4.29	$1/2^+$	0.20
2926	0	-	-	-
3367	0	-	-	-
3837	0	-	-	-
3866	16.5(19)	4.33	$(1/2^+, 3/2^+)$	0.18
4066	17.9(17)	4.24	$3/2^+$	0.23
4604	3.2(9)	4.82	$(1/2^+, 3/2^+)$	0.06
5553	2.2(6)	4.68	$(1/2^+, 3/2^+)$	0.08
5599	5.2(1)	4.28	$(1/2^+, 3/2^+)$	0.21

ference in known energy levels and the intensity flow. Although the gamma-ray with energy 1621 keV was not seen in previous experiments, it was assigned to the 3866 keV state in  $^{23}\text{F}$  based on the energy difference between the known energy levels at 2243 and 3866 keV. Table 4.12 shows the observed gamma-rays with their uncertainties, the half-lives, the gamma emission probabilities and the energy level assignments for the beta decay of  $^{23}\text{O}$ .

The absolute beta decay branching to each level was deduced from the difference between gamma-ray intensity into and out of each level, normalized to the total decay. The gamma-ray energies and their emission probabilities in parenthesis are given on the vertical arrows in Figure 4.25. The comparison of total gamma-ray feeding to the  $^{23}\text{F}$  ground state and the total gamma-ray activity in the  $^{23}\text{F}$  beta decay showed a negligible beta decay feeding to the ground state. Beta decay branching was not deduced for the states at 2926, 3367 and 3837 keV since the feeding and deexcitation intensities balanced within uncertainties. The observation of the 638 keV gamma-ray in  $^{22}\text{F}$  suggested that beta-delayed neutrons populate excited states in  $^{22}\text{F}$  as shown in Figure 4.25.

The apparent  $\log(ft)$  values were determined for the bound states in  $^{23}\text{F}$  using the method explained in previous sections. Table 4.13 shows the calculated beta decay branches,  $\log(ft)$  values and Gamow-Teller transition strengths [B(GT)] for the



Shell model calculations have been successful in reproducing the shell structure of nuclei close to the valley of stability. However, there are cases where significant differences between shell model predictions and experimental data occur. One such case is the beta decay of  $^{26}\text{Ne}$ , which was recently re-measured by Weissman et al. [79] to check the discrepancy between theory and experiment. Weissman et al. reported the beta decay feeding to three  $1^+$  states at 82.5, 1511 and 2723 keV, and two  $2^+$  states at 233.5 and 406 keV in  $^{26}\text{Na}$  compare to the previously measured two  $1^+$  states at 82.5 and 233.6 keV by Dufour et al. [78] as shown in Figure 4.26. This leads to a contradiction for the spin assignment of the 233.5 keV state based on the beta decay experiments. In contrast, the USD shell model calculations performed by Wildenthal et al. [18] predicted five  $1^+$  beta decay states in  $^{26}\text{Na}$ , with four below 2.8 MeV. The weakest beta branch among four of them was predicted to be 0.76% to the state at 2538 keV. These predicted levels were also presented in Ref. [79]. The predicted fourth  $1^+$  state was not observed by the previous beta decay experiments including the work of Weissman et al., which had a sensitivity of 0.4% for the beta branch. The nonobservation of the predicted  $1^+$  state below 3 MeV in  $^{26}\text{Na}$  shows a clear discrepancy between the experimental and theoretical values.

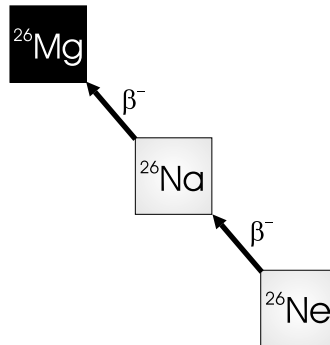


Figure 4.27:  $^{26}\text{Ne}$  beta decay chain. The stable isotope is shown in the solid square.

The energy levels of  $^{26}\text{Na}$  have been studied by Flynn et al. [82] using the  $^{26}\text{Mg}(t, ^3\text{He})$  reaction up to 4702 keV assuming a spin and parity assignment of  $3^+$  for the ground

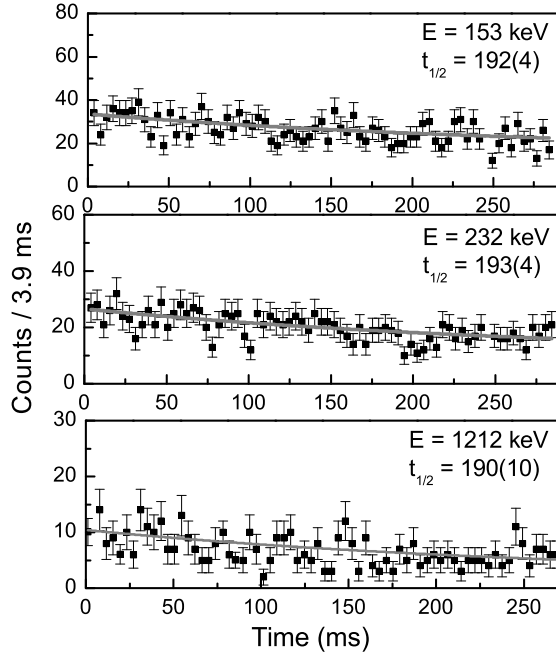


Figure 4.28: Gamma gated half-lives of  $^{26}\text{Ne}$  beta decay. The energies in keV and Half-lives in ms are given.

state of  $^{26}\text{Na}$ . Other investigations carried out by Pearce et al. [80] and Clarke et al. [76] using the same reaction reported a few more levels in addition to the previously observed ones, and assigned spins and parities to a few of the new levels in  $^{26}\text{Na}$ . Figure 4.26 summarizes the experimental and calculated energy levels in  $^{26}\text{Na}$ . The  $^{14}\text{C}(^{14}\text{C},d)$  reaction was used by Lee et al. [81] recently to observe even a few more levels in  $^{26}\text{Na}$ . This reaction confirmed the spin and parity assignment of  $1^+$  to the 82.5, 1511 and 2723 keV states and  $2^+$  to the 233.5 and 406 keV states later reported by Weissman et al. Since  $^{26}\text{Ne}$  was the largest contaminant in the  $^{23}\text{O}$  cocktail beam with a high production rate, it was interesting to remeasure the beta decay of  $^{26}\text{Ne}$  to check the controversy between previous beta decay measurements and shell model calculations.

$^{26}\text{Ne}$  decays to  $^{26}\text{Na}$ , which subsequently decays to stable  $^{26}\text{Mg}$  as shown in Figure 4.27. The beta-delayed gamma-ray spectrum observed within the beam-off time period in the  $^{23}\text{O}$  experiment, shown in Figures 4.22 and 4.23, displays the gamma-ray

lines from the  $^{26}\text{Ne}$  parent decay. The gamma-rays energies at 1003, 1129, 1365, 1411, 1775, 1809, 1898, 2526 and 2542 keV were assigned to the  $^{26}\text{Na}$  decay, the daughter of  $^{26}\text{Ne}$ , and are in agreement with a pervious experiment [19]. The gamma-ray transitions in  $^{26}\text{Na}$  were assigned as 84, 153, 232, 404, 1212, 1279 and 2486 keV based on the knowledge from the previous  $^{26}\text{Ne}$  beta decay experiment [79] and present decay curve analysis. Gated decay curves were generated for gamma-rays assigned to  $^{26}\text{Ne}$  decay that were statistically significant. The half-lives were determined by fitting a function that included a single exponential decay with constant background to the decay curves. The gamma-ray gated decay curves associated with the  $^{26}\text{Ne}$  beta decay are shown in Figure 4.28. The weighted average half-life for the  $^{26}\text{Ne}$  beta decay was deduced as 192(4) ms in present work, consistent with the reported half-life of 192(6) ms from the beta decay experiment and the theoretically estimated half-live range of 162 - 170 ms [79]. A weak gamma-ray energy 2219(4) keV could be the same as the observation of 2232(15) keV gamma-ray transition in  $^{26}\text{Na}$  by Lee et al. [81]. The gamma-ray emission probabilities, given in Table 4.14 were calculated using the total number of  $^{26}\text{Ne}$  beta decay events and the gamma-ray efficiency. The emission probability of the gamma-ray at 84 keV was not determined, because this energy was below energy threshold in some of the SeGA detectors. The gamma-ray emission probability was taken from literature for this transition [79].

The proposed beta decay scheme was given in Figure 4.29. The gamma-ray place-

Table 4.14: Gamma-ray assignment for the beta decay of  $^{26}\text{Ne}$

Gamma energy (keV)	Emission Probability (%)	Nuclide	Energy level (keV)
84(3)	95	$^{26}\text{Na}$	84
153(3)	3.4(2)	$^{26}\text{Na}$	234
232(2)	4.4(2)	$^{26}\text{Na}$	234
404(3)	0.4(1)	$^{26}\text{Na}$	404
1212(3)	1.2(3)	$^{26}\text{Na}$	2723
1279(3)	5.4(2)	$^{26}\text{Na}$	1513
2219(4)	0.6(2)	$^{26}\text{Na}$	2453
2486(4)	0.7(2)	$^{26}\text{Na}$	2723

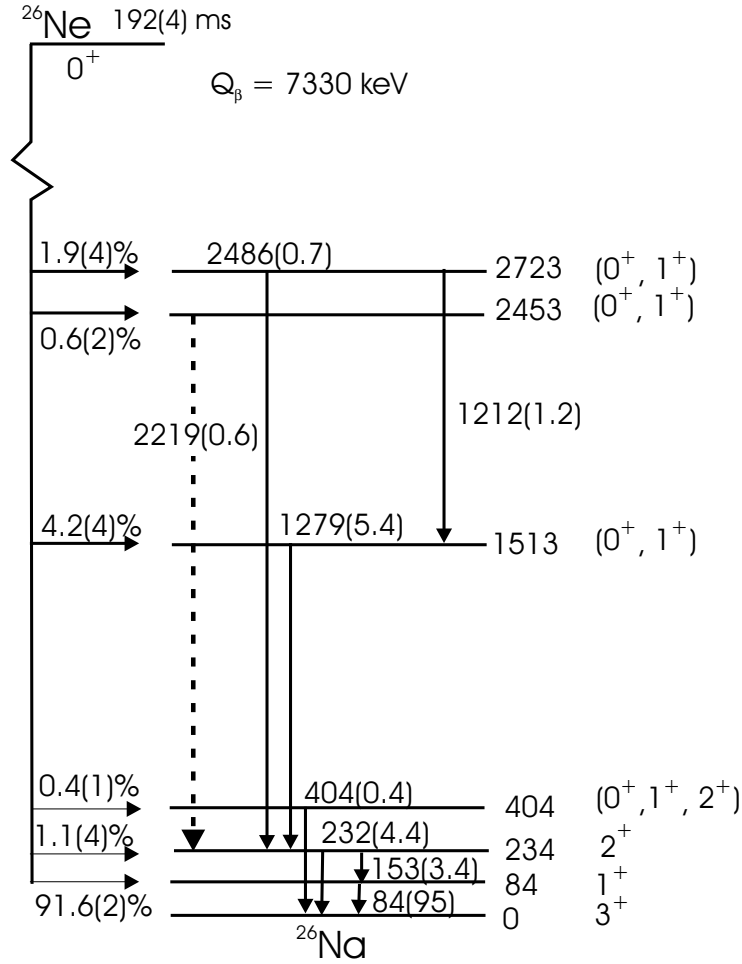


Figure 4.29: Beta decay scheme of  $^{26}\text{Ne}$ . The gamma-ray decay is given in vertical arrows with the transition energy and emission probabilities in parenthesis. The horizontal arrow shows the beta decay feeding to the level with the beta branch and the respective uncertainty in parenthesis. The dotted arrow shows a new gamma-ray transition.

ment in the decay scheme of  $^{26}\text{Ne}$  was constructed based on the knowledge from gamma-ray decay in  $^{26}\text{Na}$  from Refs. [79, 81]. All gamma-rays except for a new transitions at 2219 keV were placed among the energy levels in  $^{26}\text{Na}$  as in Ref. [79]. The assignments of these gamma-rays are given in Table 4.14. The new 2219 keV gamma-ray was tentatively placed to the known 2453 keV state [81] as a feeding to the 234 keV state to match the shell model calculations, which will be discussed in the next chapter. The beta branching was calculated by taking the difference in intensity flow into and out of a specific level. The beta decay branch to the ground state of  $^{26}\text{Na}$  was negligible as the summed intensities of gamma-rays feeding from excited states

Table 4.15: Properties of the  $^{26}\text{Ne}$  beta decay.

Energy level (keV)	Branch (%)	Log(ft)	Spin parity	B(GT)
0	-	-	$3^+$	-
84	91.6(2)	3.84	$1^+$	0.57
234	1.7(4)	5.72	$(0^+, 1^+, 2^+)$	0.008
404	0.4(1)	6.11	$(0^+, 1^+, 2^+)$	0.003
1513	4.2(4)	4.73	$(0^+, 1^+)$	0.07
2453	0.6(2)	5.23	$(0^+, 1^+)$	0.02
2723	1.9(4)	4.6	$(0^+, 1^+)$	0.10

to the ground state and  $^{26}\text{Na}$  beta decay events deduced from daughter gamma-ray activities were similar. The apparent  $\log(ft)$  values given in Table 4.15 were calculated for observed states using the method given in Ref. [71]. Four allowed beta decay transitions were found based on the beta decay selection rules. They were assigned with  $0^+$  or  $1^+$  spins and parities considering the ground state of  $^{26}\text{Ne}$  has a  $0^+$ , except for the 84 keV state, which was given a  $1^+$  to agree with previous work. The feeding to the states at 234 and 404 keV was categorized as the first forbidden decay based their  $\log(ft)$  values and the spin and parity assignments are shown in Figure 4.29. The B(GT) values given in Table 4.15 were calculated as explain in Chapter.2.

# Chapter 5

## Discussion

### 5.1 Beta Decay of $^{22}\text{N}$

The results of the beta decay of  $^{22}\text{N}$  (Figure 4.9) showed that allowed beta decay feeds five neutron unbound energy states in  $^{22}\text{O}$ . The total feeding to those states is 44(4)% of the total beta decay of  $^{22}\text{N}$ . The first forbidden beta decays, which account for 56(4)% of the total beta decay, were observed with three excited states and the ground state of  $^{22}\text{O}$ . Note that the observed first forbidden decays go to neutron bound states in  $^{22}\text{O}$ . In addition, three gamma-rays transitions in  $^{22}\text{O}$  and a single gamma-ray transition in each of the neutron daughters of  $^{21}\text{O}$  and  $^{20}\text{O}$  were confirmed from previous works. Beta-delayed neutrons of  $^{22}\text{N}$  leading to the single neutron and two neutron daughters were observed yielding neutron emission probabilities of  $P_{1n} = 33(3)\%$  and  $P_{2n} = 12(3)\%$ . The total neutron emission probability was found to be 57(5)% from gamma-ray analysis of the daughter decay activities. The half-lives and the total neutron emission probabilities of  $^{22}\text{N}$  beta decay from the present work and literature are shown in Figure 5.1 for comparison. The total neutron probability deduced in the present work are in agreement with values reported by Yoneda et al. [40] and Penionzhkevich et al. [62] but disagreed with the value reported by Reeder et al. [39]. Note that the upper limit of the two neutron emission probability

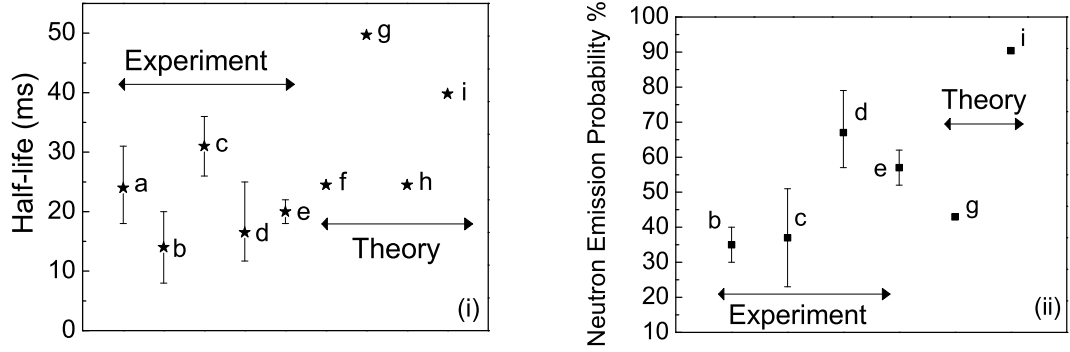


Figure 5.1: The comparison of half-life(i) and neutron emission probability(ii) of  $^{22}\text{N}$ . The values are taken from works of (a) Mueller et al. [38], (b) Reeder et al. [39], (c) Penionzhkevich [62], (d) Yoneda et al. [40], (e) present work, (f) Groote et al. [44], (g) Wapstra et al. [45], (h) Wildenthal et al. and (i) New shell model calculations. The experimental and theoretical values are labeled for both cases.

of 13% reported by Yoneda et al. agrees with our measurement. The average half-life derived from the gated decay curves was found to be 20(2) ms, which is in agreement with all previously published values [19]. Shell model calculations that are discussed below were also performed to compare the results of the  $^{22}\text{N}$  beta decay.

The new shell model calculations for the allowed beta decay of  $^{22}\text{N}$  used the WBP interaction in the *sp $s$ d* shell model space. Since the energy gap between the  $0^-$  ground state and the  $1^-$  excited state in  $^{22}\text{N}$  is predicted to be small [48], the calculations considered the feeding of  $0^-$ ,  $1^-$  and  $2^-$  states in  $^{22}\text{O}$  assuming the ground state of  $^{22}\text{N}$  as either  $0^-$  or  $1^-$ . The beta decay half-life of  $^{22}\text{N}$  was calculated to be 39.8 and 24.5 ms for the  $0^-$  or  $1^-$  ground states, respectively, and both agree with the adopted value. Figure 5.2 shows the calculated allowed beta decay schemes of  $^{22}\text{N}$  for both the  $0^-$  and  $1^-$  ground states. Note that these schemes show only the beta decay branches higher than 1%. In the case of the  $1^-$  ground state, the allowed beta branch of 9.56% feeds only one state below the neutron separation energy, and the rest of the allowed beta decay feeds the neutron unbound states resulting in a predicted total neutron emission probability of 90.4%. In contrast, the calculations for the beta decay of the  $0^-$  ground state of  $^{22}\text{N}$  predict that all allowed decay feeds neutron unbound states

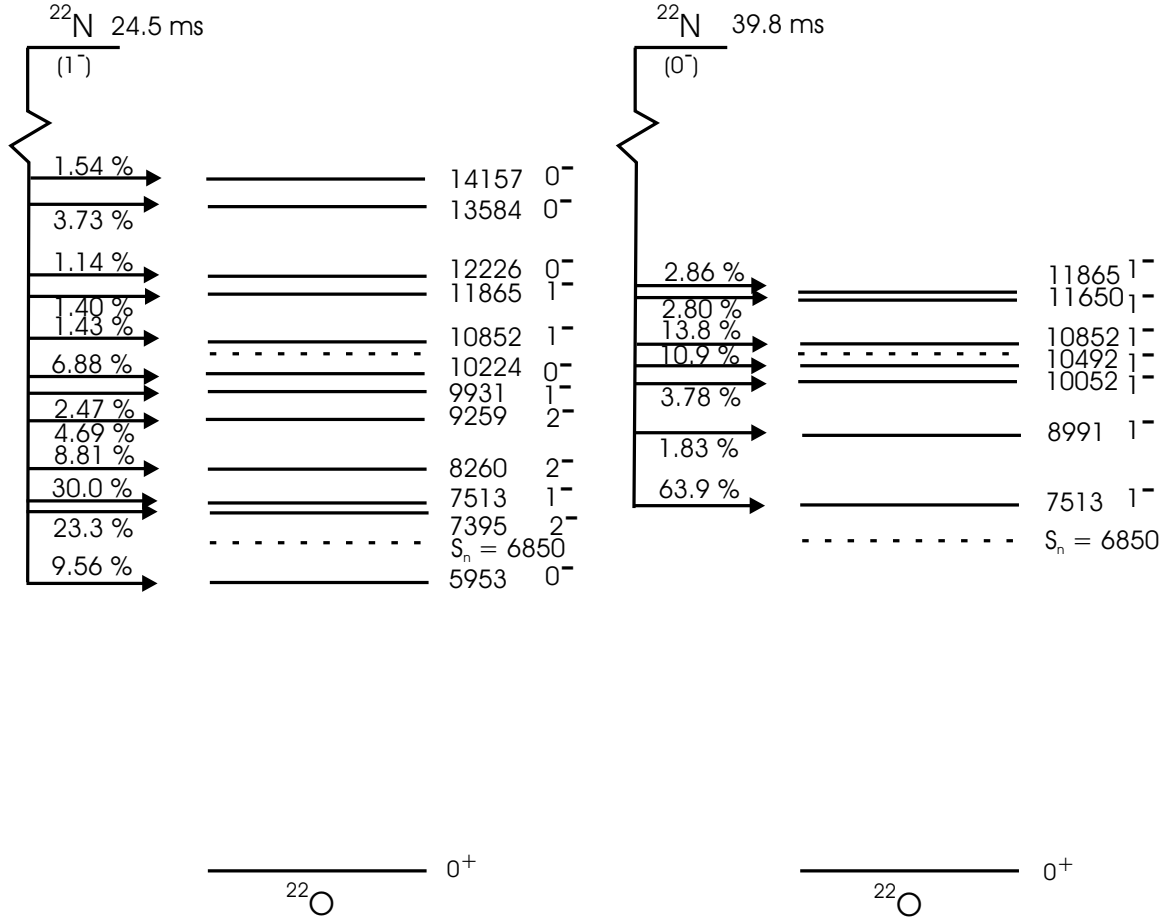


Figure 5.2: Theoretical beta decay scheme of  $^{22}\text{N}$ . The beta decay schemes shown in the left and right are calculated considering the ground state of  $^{22}\text{N}$  is  $1^-$  or  $0^-$ , respectively. The allowed beta decay branches higher than 1% are shown. The calculated half-lives in ms, spins and parities, and energies in keV are given.

making the total neutron emission probability of 100%. However, the predictions for neutron emission probabilities could change dramatically as the estimated energies of the negative parity states have about a 1 MeV uncertainty. In the extreme case, the states close to the neutron separation energy could move closer and even into the neutron bound region, reducing the total neutron emission probability to about 36%. Although this theoretical lower limit become closer to the observed single neutron emission probability of 33% by lowering the energy levels, the present experiment did not observe any bound state fed by the allowed decay. Therefore, one can expect that there should be a considerable contribution from the first forbidden decay in  $^{22}\text{N}$  decay which is consistent with our results.

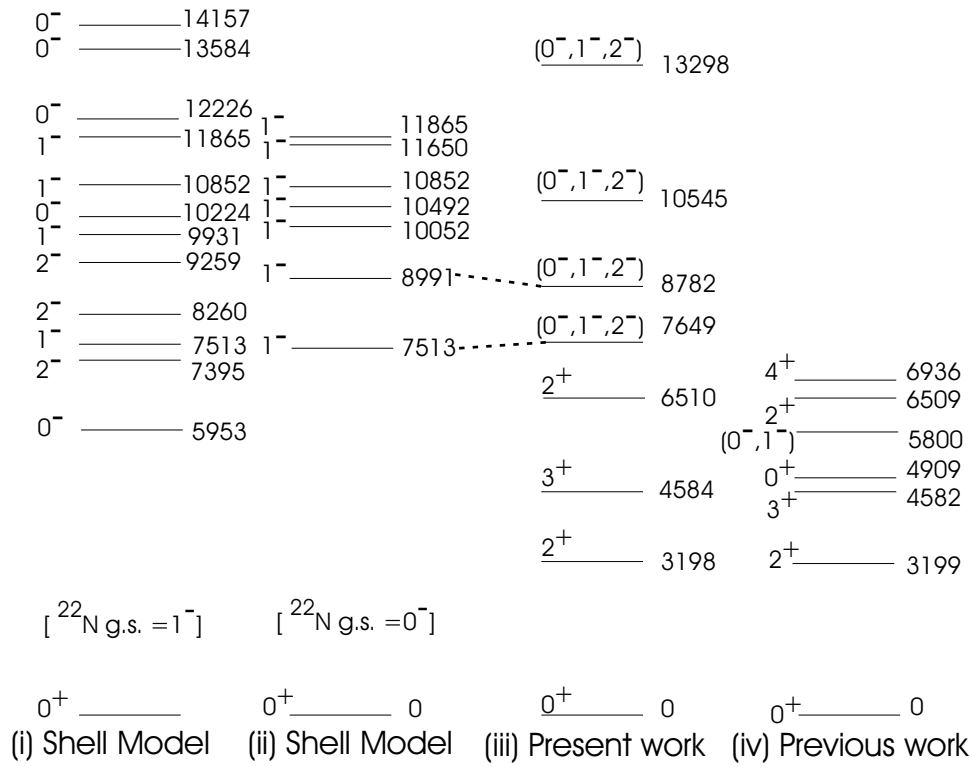


Figure 5.3: Comparison of the <sup>22</sup>O energy levels. Shell model calculated energy levels that are fed by the allowed beta decay of (i) 1<sup>-</sup> or (ii) 0<sup>-</sup> <sup>22</sup>N ground state are shown. The observed levels from (iii) present work and the known levels in <sup>22</sup>O (iv) from the works of Stanoiu et al. and Cortina-Gil et al. are shown. All energies are given in keV. The likely energy levels are connected with the dashed lines.

The energy level scheme of <sup>22</sup>O obtained in the present work and the negative parity states predicted by the shell model considering the 1<sup>-</sup> or 0<sup>-</sup> ground states for <sup>22</sup>N are compared in Figure 5.3 along with the known energy levels from previous works of Stanoiu et al. and Cortina-Gil et al. The observed energy levels are closely matched with the predicted levels that were calculated from beta decay of the 0<sup>-</sup> <sup>22</sup>N ground state compared to the beta decay of 1<sup>-</sup> state. The likely energy levels are connected with dashed lines as shown in the figure. The observed levels higher than 8782 keV are not compared due to the complexity of the shell model predictions. The positive parity bound states that are observed in this work were measured by previous experiments. However, the only known negative parity bound state at 5800 keV in <sup>22</sup>O, which is favored by beta decay, was not observed in this work.

The experimental Gamow-Teller strengths for <sup>22</sup>N beta decay are compared with

the corresponding values calculated by considering either a  $0^-$  or  $1^-$  ground state of  $^{22}\text{N}$  and are shown in Figure 5.4. The experimental values shown in the figure include the observed allowed and first forbidden beta decay transitions. In contrast, the shell model predictions, shown in the figure, are associated only with the allowed beta decay. The figure shows the  $B(\text{GT})$  values corresponding to the energy range 7 - 11 MeV derived assuming the  $1^-$  ground state for  $^{22}\text{N}$  are in reasonable agreement with the experimental values. However, the overall comparison between the observations of the  $^{22}\text{N}$  beta decay with the shell model calculations for both cases is poor due to the large strengths at high energies that are not reproduced by shell model. Large beta decay strengths for states at high excitation energy is one of the signatures of the halo structure as discussed in Chapter 1. Figure 5.4 shows large  $B(\text{GT})$  values to states at 13298 and 20839 keV in  $^{22}\text{O}$  supporting the halo structure of  $^{22}\text{N}$ . The distribution of  $B(\text{GT})$  values from the beta decay of  $^{22}\text{N}$  is similar to the beta decay of  $^{11}\text{Be}$  and  $^{11}\text{Li}$  as given in Figure 1.6. Although the above facts support the  $^{22}\text{N}$  halo structure, a study of the one-neutron knockout reaction for  $^{22}\text{N}$  is required to confirm the nature of the structure.

## 5.2 Beta Decay of $^{23}\text{O}$ and Energy States in $^{23}\text{F}$

The weighted half-life of 97(8) ms for beta decay of  $^{23}\text{O}$  measured in this experiment is consistent with the half-life reported by Mueller et al. [10]. However, the new shell model calculations using the USDB interaction [83] and free-nucleon Gamow-Teller operator predicted a half-life of 160 ms for  $^{23}\text{O}$  beta decay. Thus, the  $^{23}\text{O}$  beta decay rate is enhanced relative the theory. In contrast, the shell model calculations for  $^{22}\text{O}$  [66] and  $^{26}\text{Ne}$  decay using the same interaction produced half-lives of 1.4 s and 114 ms, both shorter than the experimental values of 2.3(1) s and 192(4) ms, respectively. The hindrance of experimental relative to theoretical half-lives for beta decay is typical, but the enhancement of the experimental  $^{23}\text{O}$  beta decay is not

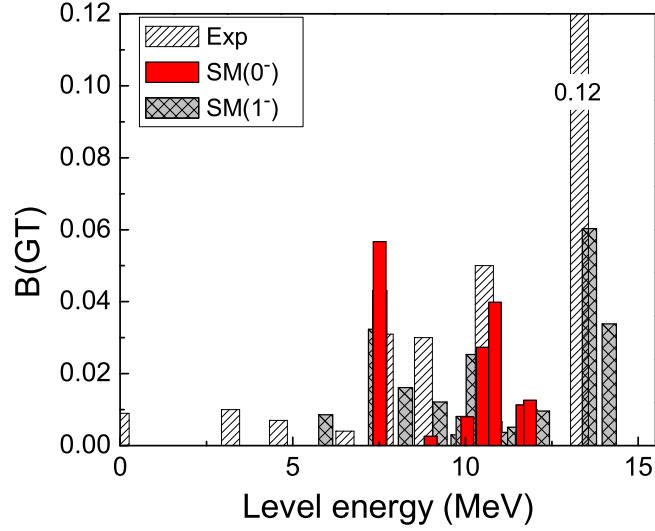


Figure 5.4: Comparison of Gamow-Teller strengths between the experiment values and the shell model calculated values for the beta decay of  $^{22}\text{N}$ . Gamow-Teller strengths are shown for the observed (Exp) and the predicted (SM( $0^-$ ) and SM( $1^-$ )) states in  $^{22}\text{O}$ .

understood. The total neutron emission probability of 7.2(18)% from present work is inconsistent with both experimental values in the literature and also with most of the theoretical predictions except for that of Wildenthal et al. and the new shell model calculations (about 2%).

Shell model calculations were performed for the allowed beta decay of  $^{23}\text{O}$  using the USDB interaction in  $sd$ -shell model space assuming a  $1/2^+$  ground state for  $^{23}\text{O}$ . In addition, the gamma-ray decay scheme of  $^{23}\text{F}$  was calculated in order to construct the complete  $^{23}\text{O}$  beta decay scheme. Figure 5.5 shows the theoretical  $^{23}\text{O}$  beta decay scheme for the allowed beta decay branches greater than 0.5%. These calculations predict that nine states are fed by allowed beta decays with branches greater than 0.5%. Two of these states are neutron unbound, leading to the total neutron emission probability of 1.7%. However, the uncertainty of about 1 MeV associated with the shell model predicted energy could move a few levels above the neutron separation energy, which yields the upper limit for the total neutron emission probability of

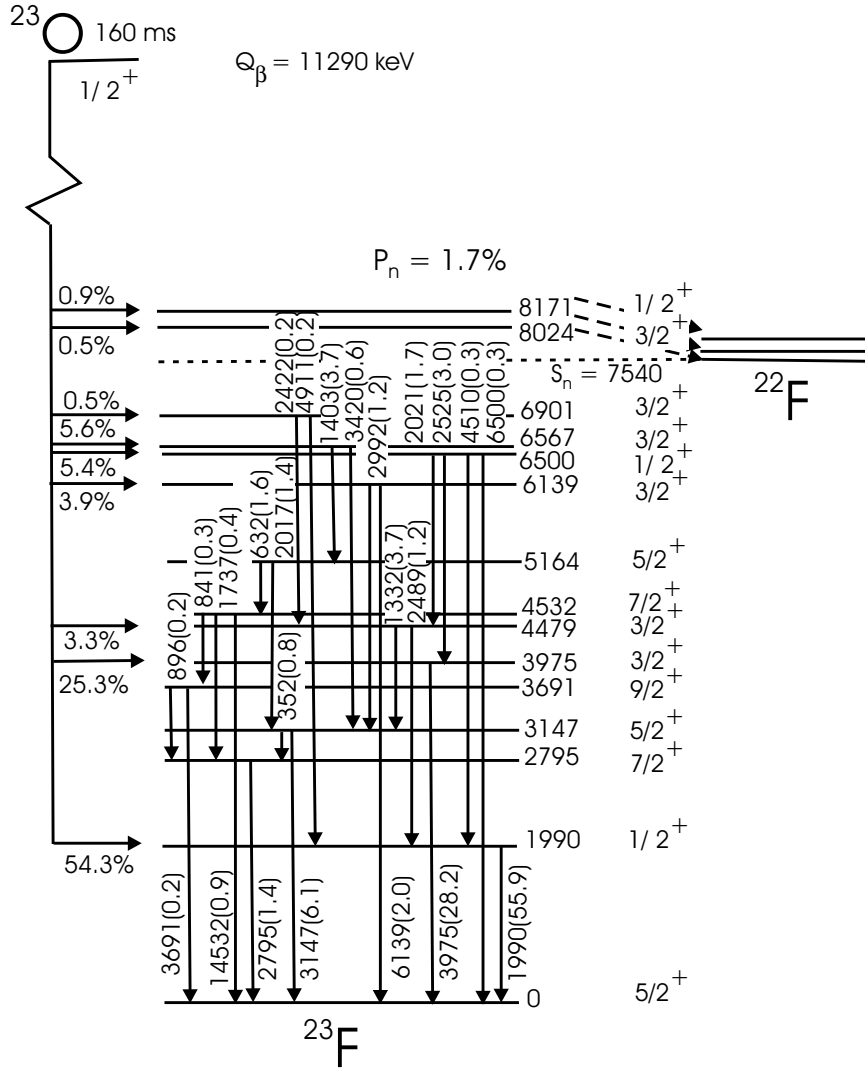


Figure 5.5: Theoretical decay scheme of  $^{23}\text{O}$ . The decay scheme was constructed with a minimum limit of 0.5% for the beta branch and 0.2% for gamma-ray emission.

12.9%. The calculations indicate major beta branching of 54.3% and 25.3% to the states at 1990 and 3975 keV. The overall agreement between the experimental and theoretical decay schemes is reasonable within the experimental detection limits.

The level scheme for  $^{23}\text{F}$  from the present work in Fig. 5.6 can be compared with the shell model calculations in  $sd$ -shell model space and previous experimental work. The thick lines in Fig. 5.6 show the predicted levels in  $^{23}\text{F}$  that have beta decay feeding greater than 0.5%. The first experimental  $1/2^+$  state located at 2243 keV is about 253 keV higher than the shell model predicted state at 1990 keV. The likely experimental and calculated states are joined with the dashed lines in the

figure. The level at 4066 keV was previously associated with the first  $3/2^+$  state based on spectroscopic factors measured by Michimasa et al.. This assignment was also supported by recently calculated spectroscopic strength for the  ${}^4\text{He}({}^{22}\text{O}, {}^{23}\text{F}\gamma)$  reaction by Brown [48]. Note that the analysis of the theoretical spectroscopic factor for the above mentioned reaction shows the state at 3975 keV contains about 50% of the  $d_{3/2}$  spectroscopic strength, which is supported by the observation of the highest cross-section going to this level in the work of Michimasa et al.. The next higher shell model state with the spin and parity of  $3/2^+$  at 4479 keV should be associated with the 4604 keV state. There are no other low spin states near 3.8 MeV in the  $sd$  model space calculations that can be associated with the 3866 keV state. Thus, this could be an intruder state. Its observation in beta decay may be due to a strong mixing

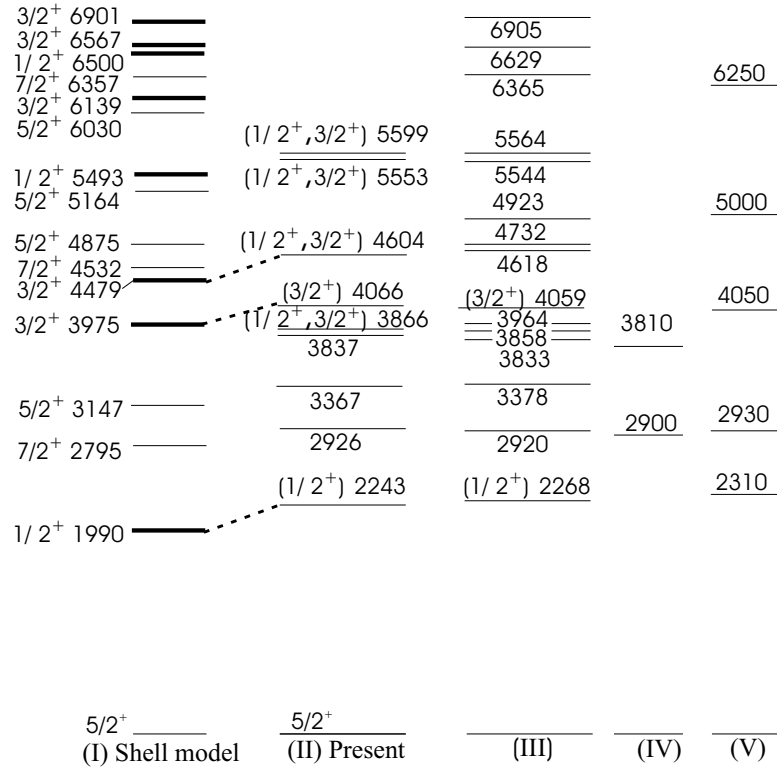


Figure 5.6: Comparison of  ${}^{23}\text{F}$  levels from the present experiment along with shell model calculations and previous works. Shell model predicted (I) allowed beta decay states in thick lines and forbidden beta decay states in thin lines, and the energy levels from the present work (II) and work of Michimasa et al. (III), Belleguic et al. (IV) and Orr et al. (V) are shown. The likely calculated and experimental states are combined with the dashed lines. All energies are given in keV.

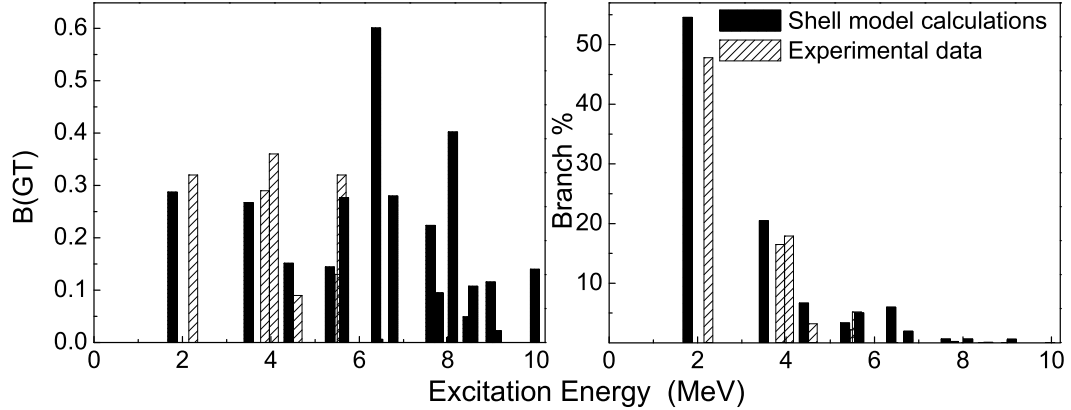


Figure 5.7: Comparison of beta decay branching (right) and Gamow-Teller strengths (left) between shell model predictions and the experiment values for the beta decay of  $^{23}\text{O}$ .

with the  $sd$ -shell state. The experimental beta decay branching and  $B(\text{GT})$  values compared with corresponding predicted values from the same reference are shown in Fig. 5.7. The experimental values for beta decay branching and  $B(\text{GT})$  to the first  $1/2^+$  state agreed reasonably with shell model predictions. The beta decay feeding to the state at 3866 keV and above is not consistent with the theory. The inconsistency is highlighted by the difference of the  $B(\text{GT})$  values.

Fig. 5.8 shows the energies of the lowest  $5/2^+$ ,  $1/2^+$  and  $3/2^+$  states in odd-mass fluorine isotopes. The ground state of odd-mass fluorine isotopes have a single proton in the  $d_{5/2}$  shell. Neutrons are added to the  $d_{5/2}$  shell as the mass of the isotope increases. The systematic variation of the lowest  $1/2^+$ ,  $3/2^+$  and  $5/2^+$  levels in the fluorine isotopes shows a sudden increase in the splitting of the  $5/2^+$  and  $1/2^+$  levels in  $^{23}\text{F}$  as shown in Fig. 5.8. This observation could be an indication of the appearance of  $N = 14$  shell closure in this region. Moreover, the lowering of the observed  $3/2^+$  state in  $^{23}\text{F}$  relative to the  $3/2^+$  state in  $^{17}\text{F}$  illustrates the influence of the monopole interaction and it can be further explained in following. The analysis of the experimental spectroscopic strengths for  $^{23}\text{F}$  taken from Michimasa et al. [43]

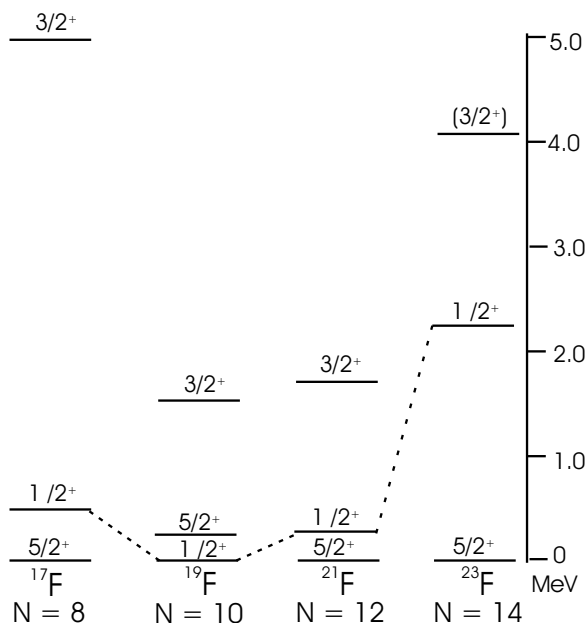


Figure 5.8: The location of experimental energy states in odd-mass fluorine isotopes as a function of neutron number. The neutron number corresponding to each isotope is given at the bottom.

and for  $^{17}\text{F}$  taken from Yasue et al. shows that the energies of the first  $3/2^+$  states in both structures represent the location of the  $d_{3/2}$  proton single particle states. Note that  $^{23}\text{F}$  has a structure with a fully occupied neutron  $d_{5/2}$  orbit in contrast to the empty neutron  $d_{5/2}$  orbit in  $^{17}\text{F}$ . Therefore, the orbital split between the proton  $d_{5/2}$  and  $d_{3/2}$  is affected by the monopole interaction where additional neutrons in  $^{23}\text{F}$  relative to  $^{17}\text{F}$  causes a reduction of  $d_{5/2} - d_{3/2}$  energy gap at  $^{23}\text{F}$ .

### 5.3 The $1^+$ Excited States in $^{26}\text{Na}$

The previous measurement of  $^{26}\text{Ne}$  beta decay observed three  $1^+$  excited states in  $^{26}\text{Na}$  at 82.5, 1511 and 2723 keV. The shell model predicts four  $1^+$  excited states below 3 MeV with relatively strong beta branches. Based on a comparison between the experimental data and the theory, Lee et al. [81] argue that the nonobservation of one of the  $1^+$  state in  $^{26}\text{Na}$  was a clear disagreement. The similar situation was observed with the beta decay of  $^{28}\text{Ne}$  reported in Ref. [84, 81]. Three allowed beta decay states with  $1^+$  at 0, 2218 and 2714 keV in  $^{28}\text{Na}$  was observed compare to

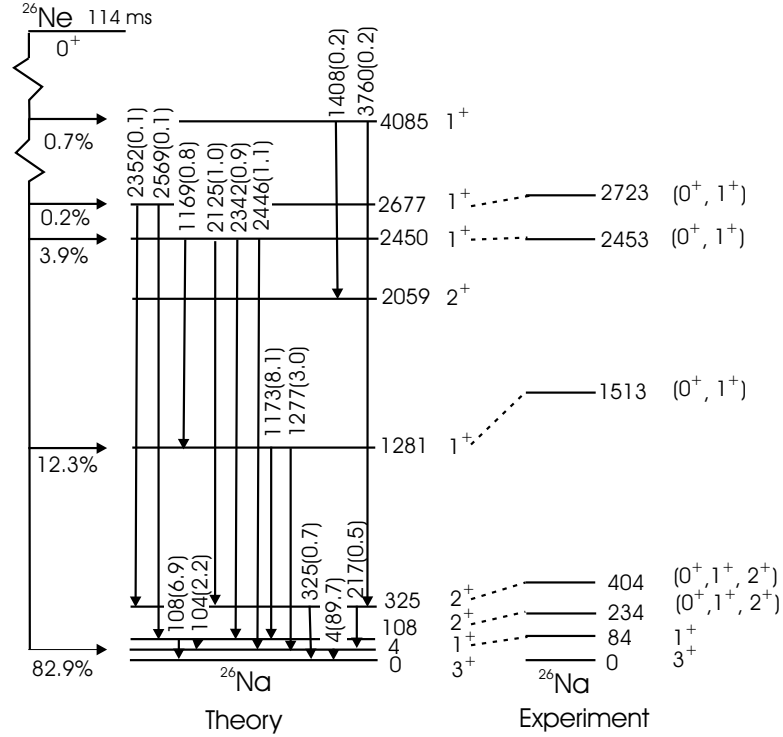


Figure 5.9: Theoretical beta decay scheme of  $^{26}\text{Ne}$ . The decay scheme is constructed with a minimum limit of 0.1% for the beta branch and gamma-ray emission probability. The observed states from present work are connected to the corresponding calculated states with the dashed lines. All energies are given in keV and the calculated half-life is 114 ms.

four allowed states in similar energy regime predicted by USD shell model for the beta decay of  $^{28}\text{Ne}$ . Therefore, the discrepancy was explored for the observed energy levels in  $^{26}\text{Na}$ . The theoretical beta decay scheme for  $^{26}\text{Ne}$ , shown in Figure 5.9, was constructed using the USDB interactions in  $sd$ -shell model space to search for the missing  $1^+$  state. The beta decay feedings greater than 0.1% are shown in the figure with the possible deexcitation gamma-rays associated with each state. The calculated energies for states in  $^{26}\text{Na}$  have a reasonable agreement as shown in Figure 5.9. However, the calculated gamma-ray decay intensities in  $^{26}\text{Na}$ , especially for higher-lying states, showed a disagreement with the observations. The observation of the 84(3), 1212(3), 1279(3) and 2486(4) keV gamma-rays originated from the  $1^+$  states at 84, 1513 and 2486 keV in the present work confirmed previous work of Weissman et al. In addition, we observed a weak gamma-ray at 2219(4) keV identified similar to

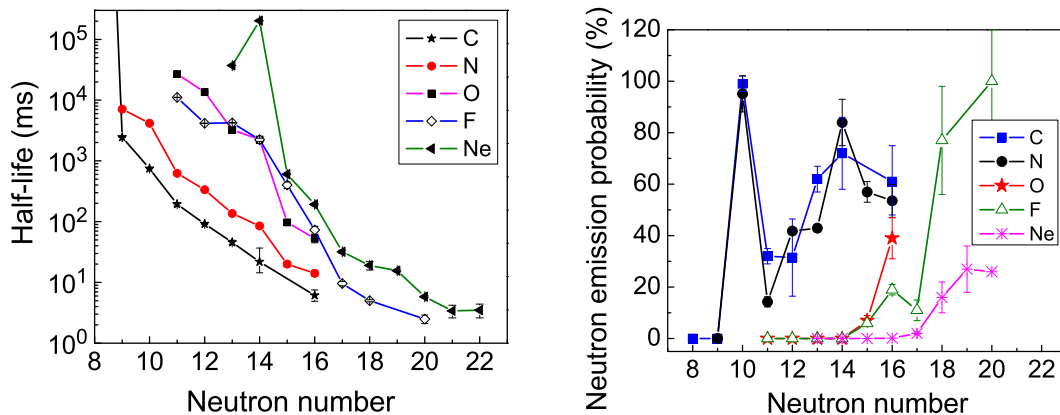


Figure 5.10: Variation of half-lives and neutron emission probabilities with neutron number.

the observation of a 2232(15) keV gamma-ray in  $^{26}\text{Na}$  by Lee et al. They assigned the 2232 keV gamma-ray to an excited level with a direct feeding to the ground state [81]. However, this transition is unlikely in the beta decay of  $^{26}\text{Ne}$  as the ground state of  $^{26}\text{Na}$  has  $3^+$  and the allowed beta decay feeding states have  $0^+$  or  $1^+$ . As well, the shell model does not predict any gamma-ray transition from  $1^+$  high energy states to  $3^+$  ground state making the placement of the 2232 keV state uncertain. Therefore, we assigned the 2219 keV gamma-ray to the known 2453 keV level feeding to the 234 keV state which matches with the shell model calculations.

## 5.4 The Half-lives and Total Neutron Emission Probabilities of Neutron-rich Light Nuclei

The variation of the experimental half-lives with increasing neutron number in neutron-rich light nuclei is shown in Figure 5.10 (left). The half-lives of  $^{22}\text{N}$ ,  $^{23}\text{O}$ ,  $^{25}\text{F}$ ,  $^{24}\text{O}$  and  $^{26}\text{Ne}$  were taken from the measurements of present work and the rest of half-lives were obtained from Ref. [19]. The general trend of decreasing half-life as the neutron number increases is seen, as expected, due to decreasing binding energy. The discon-

tinuities peaks at  $N = 14$  for oxygen and neon isotopes are obvious and indicate a possible shell closure in these isotopes. Figure 5.10 (right) shows the total neutron emission probabilities taken from Ref. [19] and from the present work for  $^{22}\text{N}$ ,  $^{25}\text{F}$ ,  $^{24}\text{O}$  and  $^{23}\text{O}$  isotopes. There is a discontinuity at  $N = 10$  for carbon and nitrogen isotopes due to the influence of the  $N = 8$  closed shell. The beta-delayed neutron daughters of  $^{16}\text{C}$  and  $^{17}\text{N}$  (isotopes at the tip of peaks) have higher stability relative to the surrounding isotopes due to the magic number  $N = 8$ . The peak at  $N = 14$  for nitrogen isotopes ( $^{21}\text{N}$ ) cannot be explained based on the argument that  $N = 14$  closed shell has an extra stability as the neutron daughter of  $^{21}\text{N}$  does not belong to closed shell configuration and this peak could be due to measurement error. The peaks shown at  $N = 16$  for oxygen and fluorine isotopes can also be explained by the extra stability due to  $N = 14$  shell closure. The isotopes  $^{24}\text{O}$  and  $^{25}\text{F}$  located at the tip of the peak have beta-delayed neutron daughters of  $^{23}\text{F}$  and  $^{24}\text{Ne}$ , respectively that have extra stability due to  $N = 14$  shell closure and, hence, more feeding to high lying states in the daughter that lead to a large neutron emission. The overall analysis showed the influence of shell closure at  $N = 14$  on the beta decay properties particularly with oxygen and fluorine isotopes.

## 5.5 Conclusion and Summary

The beta decay measurements of  $^{22}\text{N}$  and  $^{23}\text{O}$  have been performed to investigate the shell structure evolution in the region close to the oxygen drip line. The exotic fragments were produced by fragmenting a  $140\text{MeV}/A$   $^{48}\text{Ca}$  beam in a Be target. The A1900 fragment separator provided isotope selection. The desired isotopes were implanted into a thin plastic scintillator to measure beta decay events. Beta-delayed neutrons using the neutron spectroscopic array and beta-delayed gamma-rays using eight detectors from SeGA have been measured in coincidence with beta decay events. The neutron spectroscopic array was calibrated for energy and efficiency using

well-known beta-delayed neutrons from  $^{16}\text{C}$  and  $^{17}\text{N}$  beta decays. The beta-gamma coincidence efficiency and energy calibrations for SeGA detectors were produced using the known gamma-rays from the daughters of the implanted nuclei and the offline  $^{60}\text{Co}$ ,  $^{207}\text{Bi}$  and  $^{152}\text{Eu}$  sources. The cocktail beams of  $^{22}\text{N}$  and  $^{23}\text{O}$  also produced a significant amounts of  $^{25}\text{F}$ ,  $^{24}\text{O}$  and  $^{26}\text{Ne}$  impurities, allowing the study of the beta decay of these nuclei as well.

Half-lives and total neutron emission probabilities were determined with improved precision and accuracy for beta decays of  $^{22}\text{N}$ ,  $^{23}\text{O}$ ,  $^{25}\text{F}$ ,  $^{24}\text{O}$  and  $^{26}\text{Ne}$ . Single and two beta-delayed neutron emissions were observed from  $^{22}\text{N}$  decay with probabilities of 33(3)% and 12(3)%, respectively, in good agreement with literature. Five new negative parity states and three previously known positive parity states were observed in  $^{22}\text{O}$ , confirming the shell closure at  $N = 14$  for oxygen isotopes. The observation of large beta decay strength at high excitation energies in  $^{22}\text{O}$  indicates the indirect evidence for the halo structure of  $^{22}\text{N}$ . The total neutron emission probability of  $^{23}\text{O}$  beta decay was found to be 7(2)%, which was inconsistent with literature values. Systematic increase in the energy of the first  $1/2^+$  state in  $^{23}\text{F}$  relative to  $^{21}\text{F}$  indicates an existence of  $N = 14$  shell closure for the fluorine isotopes. New beta decay schemes were established for  $^{22}\text{N}$  and  $^{23}\text{O}$ . New transitions and unbound states were added to the existing beta decay schemes of  $^{25}\text{F}$ ,  $^{24}\text{O}$  and  $^{26}\text{Ne}$ .

The new results were compared to new shell model calculations particularly for  $^{22}\text{N}$ ,  $^{23}\text{O}$  and  $^{26}\text{Ne}$ . The overall agreement between the experimental and theoretical values for both  $^{23}\text{O}$  and  $^{26}\text{Ne}$  beta decay is reasonable with the experimental detection limits. However, the results from  $^{22}\text{N}$  beta decay have a poor agreement with the shell model predictions.

# Appendix A

## Beta Decay Fitting Model

The following explains how activities associated with the implanted nucleus and its decay chain vary with time during the experimental run. The activity variations of only the parent, daughter and granddaughter will be explained the simplicity. Beta decay experiment was performed in beam-on/off mode where the desired nucleus was implanted during the beam-on period and the beta decay was monitored during the beam-off time. Consider that the desired nucleus is produced at a constant rate of  $p$  ( $s^{-1}$ ) during the beam-on time of  $T$  (s). The initial activity of the parent nucleus is taken to be zero at the first cycle of the experiment. The activity variation of the parent within the first four cycles is shown in Figure A.1. The growth of the parent activity and the decay activities of the daughter and the granddaughter produced from the decay of implanted parent are given in Equations A.1, A.2 and A.3, respectively;

$$A_1 = p(1 - e^{-\lambda_1 t}) \quad (\text{A.1})$$

$$B_1 = p.D(1 - e^{-\lambda_1 t})(e^{-\lambda_1 t} - e^{-\lambda_2 t}) \quad (\text{A.2})$$

$$C_1 = \lambda_2 \lambda_3 p(1 - e^{-\lambda_1 t})(\alpha e^{-\lambda_1 t} + \beta e^{-\lambda_2 t} + \gamma e^{-\lambda_3 t}) \quad (\text{A.3})$$

where  $\lambda_1$ ,  $\lambda_2$  and  $\lambda_3$  are decay constants for the parent, the daughter and the granddaughter, respectively. The basic formulas for the growth and decay of nuclei in the

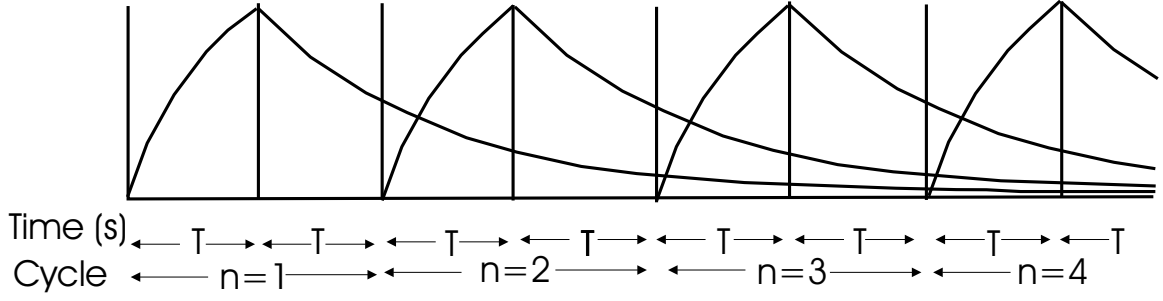


Figure A.1: The growth and decay of the parent nucleus. The first four cycles are shown and cycles are numbered by  $n$ . In each cycle, the activity is grown during the beam-on time of  $T$  s and then decay during the beam-off time of  $T$  s.

decay series are adopted from the Bateman equations [64]. The notations  $D$ ,  $\alpha$ ,  $\beta$  and  $\gamma$  are defined by following equations.

$$D = \frac{\lambda_1}{\lambda_2 - \lambda_1}$$

$$\alpha = \frac{1}{(\lambda_2 - \lambda_1)(\lambda_3 - \lambda_1)}$$

$$\beta = \frac{1}{(\lambda_1 - \lambda_2)(\lambda_3 - \lambda_2)}$$

$$\gamma = \frac{1}{(\lambda_1 - \lambda_3)(\lambda_2 - \lambda_3)}$$

The activities produced during the beam-on period of the first cycle decay during the beam-off time of  $T$  s. The decay curve of the parent during the first cycle is shown in Figure A.1 in addition to the other few cycles. Equations A.4, A.6 and A.7 illustrate how activities of the parent, the daughter and the granddaughter are varying with time during the beam-off time, respectively.

$$a_1 = p(1 - e^{-\lambda_1 T})e^{-\lambda_1(t-T)} \quad (\text{A.4})$$

$$b_1 = p.D(1 - e^{-\lambda_1 T})[(e^{-\lambda_1(t-T)} - e^{-\lambda_2(t-T)}) + (e^{-\lambda_1(T)} - e^{-\lambda_2(T)})e^{-\lambda_2(t-T)}] \quad (\text{A.5})$$

$$\begin{aligned}
c_1 = & \lambda_2 \lambda_3 p (1 - e^{-\lambda_1 t}) (\alpha e^{-\lambda_1 (t-T)} + \beta e^{-\lambda_2 (t-T)} + \gamma e^{-\lambda_3 (t-T)}) \quad (\text{A.6}) \\
& + p.D(1 - e^{-\lambda_1 T}) (e^{-\lambda_1 T} - e^{-\lambda_2 T}) D_1 (e^{\lambda_2 (t-T)} - e^{-\lambda_3 (t-T)}) \\
& + \lambda_2 \lambda_3 p (1 - e^{-\lambda_1 T}) (\alpha e^{-\lambda_1 T} + \beta e^{-\lambda_2 T} + \gamma e^{-\lambda_3 T}) e^{-\lambda_3 (t-T)}
\end{aligned}$$

The notation  $D_1$  is defined by;

$$D_1 = \frac{\lambda_2}{\lambda_3 - \lambda_2}$$

The activities produced during the beam-on period of the second cycle consist of the activities due to the implantation explained in the first cycle and the activities that have not decayed from the previous cycle. Both activities are added to derive the total activity corresponding to each nucleus, given in Equations [A.7](#), [A.9](#) and [A.10](#).

$$A_2 = p(1 - e^{-\lambda_1 (t-2T)}) + p(1 - e^{-\lambda_1 T}) e^{-\lambda_1 (t-T)} \quad (\text{A.7})$$

$$\begin{aligned}
B_2 = & p.D(1 - e^{-\lambda_1 (t-2T)}) (e^{-\lambda_1 (t-2T)} - e^{-\lambda_2 (t-2T)}) \quad (\text{A.8}) \\
& + p.D(1 - e^{-\lambda_1 (T)}) (e^{-\lambda_1 (t-T)} - e^{-\lambda_2 (t-T)}) \\
& + p.D(1 - e^{-\lambda_1 (T)}) (e^{-\lambda_1 (T)} - e^{-\lambda_2 (T)}) e^{\lambda_2 (t-T)}
\end{aligned}$$

$$\begin{aligned}
C_2 = & \lambda_2 \lambda_3 p (1 - e^{-\lambda_1 (t-2T)}) (\alpha e^{-\lambda_1 (t-2T)} + \beta e^{-\lambda_2 (t-2T)} + \gamma e^{-\lambda_3 (t-2T)}) \quad (\text{A.9}) \\
& + \lambda_2 \lambda_3 p (1 - e^{-\lambda_1 T}) (\alpha e^{-\lambda_1 (t-T)} + \beta e^{-\lambda_2 (t-T)} + \gamma e^{-\lambda_3 (t-T)}) \\
& + p.D(1 - e^{-\lambda_1 T}) (e^{-\lambda_1 T} - e^{-\lambda_2 T}) D_1 (e^{\lambda_2 (t-T)} - e^{-\lambda_3 (t-T)}) \\
& + \lambda_2 \lambda_3 p (1 - e^{-\lambda_1 T}) (\alpha e^{-\lambda_1 T} + \beta e^{-\lambda_2 T} + \gamma e^{-\lambda_3 T}) e^{-\lambda_3 (t-T)}
\end{aligned}$$

As in previous cycle, the produced activities are decayed during the beam-off period and the total activity corresponding to each nucleus is taken by adding the decay of the activity produced in the present cycle and the decay of the remaining activity from the previous cycle. The variation of activities with time for the parent,

the daughter and the granddaughter are given in Equations [A.10](#), [A.12](#) and [A.13](#).

$$a_2 = p(1 - e^{-\lambda_1(T)})e^{-\lambda_1(t-3T)} + p(1 - e^{-\lambda_1 T})e^{-\lambda_1(t-T)} \quad (\text{A.10})$$

$$\begin{aligned} b_2 = & p.D(1 - e^{-\lambda_1 T})[(e^{-\lambda_1(t-3T)} - e^{-\lambda_2(t-3T)}) \\ & +(e^{-\lambda_1(t-T)} - e^{-\lambda_2(t-T)}) + (e^{-\lambda_1(T)} - e^{-\lambda_2(T)}) \\ & (e^{-\lambda_1(t-T)} - e^{-\lambda_2(t-T)})] \end{aligned} \quad (\text{A.11})$$

$$\begin{aligned} c_2 = & \lambda_2\lambda_3p(1 - e^{-\lambda_1 T})(\alpha e^{-\lambda_1(t-3T)} + \beta e^{-\lambda_2(t-3T)} + \gamma e^{-\lambda_3(t-3T)}) \quad (\text{A.12}) \\ & + \lambda_2\lambda_3p(1 - e^{-\lambda_1 T})(\alpha e^{-\lambda_1(t-T)} + \beta e^{-\lambda_2(t-T)} + \gamma e^{-\lambda_3(t-T)}) \\ & + p.D(1 - e^{-\lambda_1 T})(e^{-\lambda_1 T} - e^{-\lambda_2 T}) \\ & D_1[(e^{\lambda_2(t-T)} - e^{-\lambda_3(t-T)}) + (e^{-\lambda_2(t-3T)} - e^{-\lambda_3(t-3T)})] \\ & + \lambda_2\lambda_3p(1 - e^{-\lambda_1 T})(\alpha e^{-\lambda_1 T} + \beta e^{-\lambda_2 T} + \gamma e^{-\lambda_3 T}) \\ & \times (e^{-\lambda_3(t-T)} + e^{-\lambda_3(t-3T)}) \end{aligned}$$

The variation of activities with time corresponding to each nucleus can be written for the  $n^{th}$  cycle expanding the algorithm discussed above. The activity of any nucleus during the beam-on period contains the activity due to the implantation or its decay in the present cycle and activities decaying from  $n-1$  number of previous cycles. Note that the  $n^{th}$  cycle begins after spending of  $2T(n-1)$  s time from the beginning of the experimental run. The activity relationship with time for the parent, the daughter and the granddaughter are given in Equations [A.13](#), [A.15](#) and [A.16](#).

$$A_n = p(1 - e^{-\lambda_1 t}) + p(1 - e^{-\lambda_1 T})e^{-\lambda_1(t+T)} \left( \frac{1 - e^{\lambda_1 2T(n-1)}}{1 - e^{\lambda_1 2T}} \right) \quad (\text{A.13})$$

$$\begin{aligned}
B_n &= p.D(1 - e^{-\lambda_1 t})(e^{-\lambda_1 t} - e^{-\lambda_2 t}) + p.D(1 - e^{-\lambda_1 T}) \\
&\quad [e^{-\lambda_1(t+T)} \left( \frac{1 - e^{\lambda_1 2T(n-1)}}{1 - e^{\lambda_1 2T}} \right) - e^{-\lambda_2(t+T)} \left( \frac{1 - e^{\lambda_2 2T(n-1)}}{1 - e^{\lambda_2 2T}} \right) \\
&\quad + (e^{-\lambda_1(T)} - e^{-\lambda_2(T)})(e^{-\lambda_2(t+T)} \left( \frac{1 - e^{\lambda_2 2T(n-1)}}{1 - e^{\lambda_2 2T}} \right))] \tag{A.14}
\end{aligned}$$

$$\begin{aligned}
C_n &= \lambda_2 \lambda_3 p(1 - e^{-\lambda_1 t})(\alpha e^{-\lambda_1 t} + \beta e^{-\lambda_2 t} + \gamma e^{-\lambda_3 t}) \\
&\quad + \lambda_2 \lambda_3 p(1 - e^{-\lambda_1 T})[\alpha e^{-\lambda_1(t+T)} \left( \frac{1 - e^{-\lambda_1 2T(n-1)}}{1 - e^{-\lambda_1 2T}} \right) \\
&\quad + \beta e^{-\lambda_2(t+T)} \left( \frac{1 - e^{-\lambda_2 2T(n-1)}}{1 - e^{-\lambda_2 2T}} \right) + \gamma e^{-\lambda_3(t+T)} \left( \frac{1 - e^{-\lambda_3 2T(n-1)}}{1 - e^{-\lambda_3 2T}} \right)] \\
&\quad + p.D(1 - e^{-\lambda_1 T})(e^{-\lambda_1 T} - e^{-\lambda_2 T})D_1 \\
&\quad [e^{-\lambda_2(t+T)} \left( \frac{1 - e^{-\lambda_2 2T(n-1)}}{1 - e^{-\lambda_2 2T}} \right) - e^{-\lambda_3(t+T)} \left( \frac{1 - e^{-\lambda_3 2T(n-1)}}{1 - e^{-\lambda_3 2T}} \right)] \\
&\quad + \lambda_2 \lambda_3 p(1 - e^{-\lambda_1 T})(\alpha e^{-\lambda_1 T} + \beta e^{-\lambda_2 T} + \gamma e^{-\lambda_3 T}) \\
&\quad \times e^{-\lambda_3(t+T)} \left( \frac{1 - e^{-\lambda_3 2T(n-1)}}{1 - e^{-\lambda_3 2T}} \right) \tag{A.15}
\end{aligned}$$

At the beam-off period of  $n^{th}$  cycle, The activities produced from all previous cycles and the implanted activity during the beam-on period of the present cycle are decay to yield the total activity of the desired nucleus. Equations A.16, A.18 and A.19 represent how the activities of the parent, the daughter and the granddaughter vary with time during the beam-off period of  $n^{th}$  cycle, respectively.

$$a_n = p(1 - e^{-\lambda_1 T})e^{-\lambda_1 t} \left( \frac{1 - e^{\lambda_1 2Tn}}{1 - e^{\lambda_1 2T}} \right) \tag{A.16}$$

$$\begin{aligned}
b_n = & p.D(1 - e^{-\lambda_1 T})[e^{-\lambda_1 t} \left( \frac{1 - e^{\lambda_1 2Tn}}{1 - e^{\lambda_1 2T}} \right) \\
& - e^{-\lambda_2 t} \left( \frac{1 - e^{\lambda_2 2Tn}}{1 - e^{\lambda_2 2T}} \right) + (e^{-\lambda_1(T)} - e^{-\lambda_2(T)}) \\
& \times e^{-\lambda_2 t} \left( \frac{1 - e^{\lambda_2 2Tn}}{1 - e^{\lambda_2 2T}} \right)] \tag{A.17}
\end{aligned}$$

$$\begin{aligned}
c_n = & \lambda_2 \lambda_3 p(1 - e^{-\lambda_1 T})[\alpha e^{-\lambda_1 t} \left( \frac{1 - e^{-\lambda_1 2Tn}}{1 - e^{-\lambda_1 2T}} \right) \\
& + \beta e^{-\lambda_2 t} \left( \frac{1 - e^{-\lambda_2 2Tn}}{1 - e^{-\lambda_2 2T}} \right) + \gamma e^{-\lambda_3 t} \left( \frac{1 - e^{-\lambda_3 2Tn}}{1 - e^{-\lambda_3 2T}} \right)] \\
& + p.D(1 - e^{-\lambda_1 T})(e^{-\lambda_1 T} - e^{-\lambda_2 T})D_1 \\
& [e^{-\lambda_2 T} \left( \frac{1 - e^{-\lambda_2 2Tn}}{1 - e^{-\lambda_2 2T}} \right) - e^{-\lambda_3 T} \left( \frac{1 - e^{-\lambda_3 2Tn}}{1 - e^{-\lambda_3 2T}} \right)] \\
& + \lambda_2 \lambda_3 p(1 - e^{-\lambda_1 T})(\alpha e^{-\lambda_1 T} + \beta e^{-\lambda_2 T} + \gamma e^{-\lambda_3 T}) \\
& \times e^{-\lambda_3 t} \left( \frac{1 - e^{-\lambda_3 2Tn}}{1 - e^{-\lambda_3 2T}} \right) \tag{A.18}
\end{aligned}$$

The beta-delayed neutron branch of the decay series is included by incorporating the total neutron emission probability ( $P_n$ ) to equations, where the production activity is replaced with the product of the initial activity and  $P_n$  value. The data used in fitting and simulation procedures are given in Table A.1

Table A.1: Decay curve fitting parameters.

Nuclide	Half-life	$P_n$ (%)	Purity (%)	Nuclide	Half-life	$P_n$ (%)	Purity (%)
<sup>22</sup> N	24 ms	67	51.8	<sup>24</sup> Ne	3.38 min	58	12.6
<sup>22</sup> O	2.25 s			<sup>24</sup> Na	14.9590 h		
<sup>22</sup> F	4.23 s			<sup>24</sup> O	53 ms		
<sup>21</sup> O	3.42 s			<sup>24</sup> F	384 ms		
<sup>21</sup> F	4.158 s	23	35.6	<sup>23</sup> F	2.23 s	5.9	2.1
<sup>20</sup> O	13.51 s			<sup>23</sup> Ne	37.24 s		
<sup>20</sup> F	11.163 s			<sup>23</sup> O	82 ms		
<sup>25</sup> F	73 ms			<sup>26</sup> Ne	197 ms		
<sup>25</sup> Ne	602 ms			<sup>26</sup> Na	1.07128 s		
<sup>25</sup> Na	59.1 s			<sup>21</sup> N	85 ms		
				81	0.6		

# Appendix B

## Gamma-ray Spectrum Analysis

The beta-gamma coincidence spectrum from  $^{22}\text{N}$  experiment was analyzed to reveal gamma-ray energies and their emission probabilities using respective calibrations. Since this spectrum contained gamma-ray transitions from all beta decays associated with the beta decay chains of  $^{22}\text{N}$ ,  $^{25}\text{F}$  and  $^{24}\text{O}$ , the gamma-ray identification was done based on knowledge from previous experiments and by extracting gated half-lives for gamma-ray peaks, which had significant statistics. The analysis of gamma-ray spectrum includes the determination of energy, emission probability and assignment. The summary of the gamma-ray spectrum analysis and the literature information on relevant beta decays are presented in Table B.5.

Table B.1: Gamma-ray measurements and literature data for  $^{22}\text{N}$  (I)

Experimental		Literature	
Gamma-ray Energy (keV)	Emission Probability (%)	Gamma-ray Energy (keV)	Emission Probability (%)
$^{22}\text{N}$ beta decay		Half-life: 24(5) ms	
1221(3)	7.0(11)	1383(4)	43(8)
1386(4)	3.0(16)	2354(6)	20(7)
1674(3)	2.2(12)	3199(8)	100(15)
3198(8)	21(3)	3310(90)	< 17
3312(5)	2(1)	3710(90)	15(7)

Table B.2: Gamma-ray measurements and literature data for  $^{22}\text{N}$  (II)

Experimental		Literature	
Gamma-ray Energy (keV)	Emission Probability (%)	Gamma-ray Energy (keV)	Emission Probability (%)
$^{22}\text{O}$ beta decay		Half-life: 2.25 s	
637(3)	96(5)	72	100
708(4)	9(3)	638	98(10)
918(3)	33(3)	918	33(5)
1863(4)	59(4)	944	3(1)
1874(4)	8(3)	1862	63(3)
2501(4)	3(1)	2499	1.5(10)
$^{22}\text{F}$ beta decay		Half-life: 4.23 s	
1275(4)	101(6)	1275.54(3)	100
1901(4)	10(3)	1900.0(6)	8.7(4)
2084(6)	84(5)	2082.6(5)	81.9(2)
2167(5)	58(5)	2166.1(5)	61.6(14)
2992(7)	5(3)	2987.7(9)	7.0(3)
4372(9)	11(3)	3983.5(10)	1.2(2)
		4247.9(10)	1.0(2)
		4366.1(10)	11.3(6)
$^{21}\text{O}$ beta decay		Half-life: 3.42 s	
278(3)	13(3)	279.92(6)	324(12)
933(3)	6(3)	933.2(3)	127(12)
1451(6)	11(6)	1450.5(2)	216(12)
1731(5)	42(4)	1729.2	90(12)
1751(5)	9(4)	1730.28(8)	1000(12)
1788(5)	13(3)	1754.74(8)	248(12)
1885(4)	8(3)	1787.16(8)	311(12)
		1884.01(9)	150(12)
		3179.43(10)	115(12)
		3459.38(13)	65(12)
		3517.40(10)	338(12)
		4572.2(4)	104(12)
		4583.5(3)	116(12)
$^{21}\text{F}$ beta decay		Half-life: 4.158 s	
349(3)	91(3)	350.725(8)	10000
1395(4)	12(5)	1395.131(17)	1713(30)
		1745.8	86.4(15)
		1890.4(3)	0.20(3)
		1989(1)	0.022(6)
		2779.4(3)	0.177(17)

Table B.3: Gamma-ray measurements and literature data  $^{22}\text{N}$  (III)

Experimental		Literature	
Gamma-ray Energy (keV)	Emission Probability (%)	Gamma-ray Energy (keV)	Emission Probability (%)
$^{21}\text{F}$ beta decay		Half-life: 4.158 s	
		2793.94(5)	0.20(3)
		3384.6(2)	0.039(6)
		3533.2(4)	0.326(17)
		3735.2(5)	0.278(26)
		3883.9	0.107(14)
		4174.1(3)	3.57(7)
		4333.52(25)	5.31(14)
		4525.84(24)	1.06(3)
		4684.27(25)	3.13(11)
$^{20}\text{O}$ beta decay		Half-life: 13.51 s	
1057(2)	100(2)	325.73(14)	0.0001(1)
		653.2(3)	0.0001(1)
		656.00(3)	0.0002(2)
		983.53(4)	0.0011(2)
		1056.78(3)	99.975(3)
		1187.70(6)	0.0001(1)
		1309.17(3)	0.0023(1)
		1644.50(8)	0.0020(2)
		1843.74(3)	0.0018(1)
		2179.09(4)	0.0025(2)
		2431.43(99)	0.0019(8)
		2504.54(18)	0.0010(1)
		3488.13(4)	0.0196(68)
$^{20}\text{F}$ beta decay		Half-life: 11.163 s	
1634(2)	100(3)	1633.602(15)	99.9995
		3332.54(20)	0.0082(60)
		4965.85(20)	0.00005(2)
$^{23}\text{F}$ beta decay		Half-life: 2.23 s	
492(2)	6(2)	492.9(7)	11(3)
819(4)	8(3)	815.2(5)	25(5)
1017(2)	9(3)	1016.7(5)	20(6)
1701(3)	32(6)	1701.44	100(5)
1820(3)	17(4)	1822.25(21)	47.4(26)
1918(4)	7(4)	1919.3(5)	19.3(25)
2127(5)	24(7)	2128.8(7)	68(11)
		2314.2(8)	7.7(27)
		2414.3(4)	15(3)
		2515.9(13)	2.9(10)

Table B.4: Gamma-ray measurements and literature data for  $^{22}\text{N}$  (IV)

Experimental		Literature	
Gamma-ray Energy (keV)	Emission Probability (%)	Gamma-ray Energy (keV)	Emission Probability (%)
$^{23}\text{F}$ beta decay		Half-life: 2.23 s	
		2734.2(5)	11.9(16)
		3431.4(4)	25.4(16)
		3830.7(4)	6.8(9)
$^{23}\text{Ne}$ beta decay		Half-life: 37.24 s	
438(3)	32(2)	439.986	33.0(13)
		1635.96	1.00(4)
		2075.91	0.101(6)
		2541.92	0.027(2)
		2981.85	0.038(2)
$^{24}\text{O}$ beta decay		Half-life: 61(26) ms	
520(3)	14(4)	521.5(3)	14.3(20)
1312(5)	13(5)	1309.5(5)	12.0(26)
1832(4)	30(5)	1831.6(5)	28.3(30)
3002(6)	14(4)		
$^{24}\text{F}$ beta decay		Half-life: 400(50) ms	
1983(4)		1981.5	100
$^{24}\text{Ne}$ beta decay		Half-life: 3.38(2) min	
474(2)	101(7)	472.202	100
876(3)	5(3)	874.41	8.0(3)
$^{24}\text{Na}$ beta decay		Half-life: 14.9590(12) h	
1369(4)	100(5)	996.82	0.0014(2)
2756(4)	99(8)	1368.633	100
		2754.028	99.944(4)
		2869.50	0.0003(1)
		3866.19	0.052(4)
		4237.96	0.0011(2)
$^{25}\text{F}$ beta decay		Half-life: 90(9) ms	
572(3)	12(2)	574.7(5)	9.5(9)
1236(3)	7(2)	1234	
1616(4)	11.2(38)	1613.4(12)	11.6(18)
1623(4)	10.6(38)	1622	
1703(3)	31(5)	1702.7(7)	39.1(26)
2090(5)	25(4)	2090	
2187(4)	5(2)	2188.6(13)	7.2(16)

Table B.5: Gamma-ray measurements and literature data for  $^{22}\text{N}$  (V)

Experimental		Literature	
Gamma-ray Energy (keV)	Emission Probability (%)	Gamma-ray Energy (keV)	Emission Probability (%)
$^{25}\text{Ne}$ beta decay		Hal4-life: 602(8) ms	
87(3)		89.53	95.5(6)
981(4)	18(4)	979.77	18.1(19)
1071(3)	2(1)	1069.30	2.3(4)
2203(4)	3(2)	1133.00	0.4(3)
		2112.00	0.62(19)
		2202.00	1.1(3)
		3219.00	0.53(15)
		3597.00	0.22(16)
		3687.00	0.96(24)
$^{25}\text{Na}$ beta decay		Hal4-life: 59.1(6) s	
386(2)	10(3)	389.70	97.5(17)
583(4)	12(2)	585.03	100.0(14)
976(4)	15(4)	836.84	0.800(20)
1613(4)	10(3)	974.72	115.0(17)
		989.85	1.280(24)
		1379.53	1.78(4)
		1611.711	72.9(11)
		1964.53	1.128(17)
		2216.32	0.719(16)
		2801.30	0.380(12)

The radioactive beam of  $^{23}\text{O}$  was implanted with impurities of  $^{26}\text{Ne}$ ,  $^{24}\text{F}$  and  $^{21}\text{N}$  in  $^{23}\text{O}$  experiment. Thus, the beta-gamma coincidence spectrum from  $^{23}\text{O}$  experiment contains gamma-ray decay events from beta decay of impurities and their decay series in addition to  $^{23}\text{O}$  decay series. The results of the analysis of the beta-gamma-ray coincidence spectrum are shown in Table B.7 and compared with relevant literature values.

Table B.6: Gamma-ray measurements and literature data for  $^{23}\text{O}$  (I)

Experimental		Literature	
Gamma-ray Energy (keV)	Emission Probability (%)	Gamma-ray Energy (keV)	Emission Probability (%)
$^{23}\text{O}$ beta decay		Hal4-life: 82(+45-28) ms	
638(3)	1.5(8)	913(7)	
911(4)	2.7(12)	1240(12)	
1237(4)	3.1(9)	1696(25)	
1621(6)	5.7(10)	1706(21)	
1716(6)	2.1(6)	1711(8)	
2243(8)	51.5(12)	2003(12)	
2673(9)	5(1)	2268(12)	
2926(10)	7(2)	2644(49)	
3367(13)	4.5(10)	2920(3)	
3868(15)	10.1(16)	3378(11)	
4066(16)	17.1(17)	3445(54)	
		3858(24)	
		3985(41)	
		4059(11)	
		4732(59)	
$^{23}\text{F}$ beta decay		Hal4-life: 2.23 s	
493(2)	3.1(7)	492.9(7)	11(3)
816(4)	7(3)	815.2(5)	25(5)
1017(2)	6.5(12)	1016.7(5)	20(6)
1701(3)	33(2)	1701.44	100(5)
1822(3)	18(4)	1822.25(21)	47.4(26)
1920(4)	8(2)	1919.3(5)	19.3(25)
2132(5)	24(2)	2128.8(7)	68(11)
2316(7)	3(1)	2314.2(8)	7.7(27)

Table B.7: Gamma-ray measurements and literature data for  $^{23}\text{O}$  (II)

Experimental		Literature	
Gamma-ray Energy (keV)	Emission Probability (%)	Gamma-ray Energy (keV)	Emission Probability (%)
$^{23}\text{F}$ beta decay		Hal4-life: 2.23 s	
2415(6)	4(2)	2414.3(4)	15(3)
2734(7)	5(1)	2515.9(13)	2.9(10)
3432(8)	9(1)	2734.2(5)	11.9(16)
3831(11)	3(1)	3431.4(4)	25.4(16)
		3830.7(4)	6.8(9)
$^{23}\text{Ne}$ beta decay		Hal4-life: 37.24 s	
439(3)	33(1)	439.986	33.0(13)
1636(3)	1.2(4)	1635.96	1.00(4)
		2075.91	0.101(6)
		2541.92	0.027(2)
		2981.85	0.038(2)
$^{22}\text{F}$ beta decay		Hal4-life: 4.23 s	
1274(3)	99(7)	1275.54(3)	100
2083(6)	73(12)	1900.0(6)	8.7(4)
2166(5)	56(13)	2082.6(5)	81.9(2)
		2166.1(5)	61.6(14)
		2987.7(9)	7.0(3)
		3983.5(10)	1.2(2)
		4247.9(10)	1.0(2)
		4366.1(10)	11.3(6)
$^{26}\text{Ne}$ beta decay		Hal4-life: 197(1) ms	
84(3)	95	82.5	100
153(3)	3.4(2)	151	3.3(7)
232(2)	4.4(2)	232.5	4.9(10)
404(3)	0.4(1)	406	0.4(2)
1212(3)	1.2(3)	1211	1.3(4)
1279(3)	5.4(2)	1278	5.9(10)
2219(4)	0.6(2)	2489	1.1(3)
2486(4)	0.7(2)		
$^{26}\text{Na}$ beta decay		Hal4-life: 1.07128(25) s	
1003(2)	1.1(1)	1002.61(12)	1.282(8)
1129(2)	5.9(2)	1128.89(13)	5.93(3)
1365(2)	0.37(6)	1365.21(15)	0.3517(15)
1411(3)	2.3(3)	1411.32(16)	2.466(7)
1775(3)	1.7(2)	1775.08(20)	1.57(4)
1809(2)	97(2)	1808.71(20)	100
1898(3)	2.1(4)	1896.78(22)	2.074(7)
2526(5)	1.2(2)	2524.1(3)	1.43(3)
2542(5)	2.2(2)	2541.6(3)	2.39(5)

# Bibliography

- [1] M. G. Mayer and J. H. D. Jenson. *Elementary Theory of Nuclear Shell Structure*. John Wiley & Sons, Inc., New York, 1955. [1](#), [3](#)
- [2] B. A. Brown. *Prog. in Part. And Nucl. Phys.*, 47:517, 2001. [2](#), [4](#)
- [3] B. A. Brown. New magic nuclei towards the drip lines. In *Proceedings of the 10th International Conference on Nuclear Reaction Mechanisms (Ed. By E. Gadioli)*. Varenna, Italy, Ricerca Scientifica ed Educazione Permanente, 2003. Sup. N.122, p.41. [3](#), [7](#)
- [4] Y. Utsuno, T. Otsuka, T. Mizusaki, and M. Honma. *Phys. Rev. C*, **64**:011301, 2001. [4](#), [5](#)
- [5] M. Thoennessen. *Rep. Prog. Phys.*, **67**:1187, 2004. [4](#)
- [6] Isao Tanihata. *Nucl. Phys. A*, **682**:114c, 2001. [4](#), [6](#)
- [7] B. Jonson. *Phys. Reports*, **389**:1, 2004. [4](#), [9](#), [10](#)
- [8] A.G. Artukh, V.V. Avedichikov, L.P. Chelnokov, G.F. Gridnev, V.L. Vakatov, V.V. Volkov, and J. Wilczynski. *Phys. Lett. B*, **32**:43, 1970. [5](#)
- [9] A. T. Kruppa, P.-H. Heenen, H. Flocard, and R. J. Liotta. *Phys. Rev. Lett.*, **79**(12):2217, 1997. [5](#)
- [10] D. Guillemaud-Mueller, J. C. Jacmart, E. Kashy, A. Latimier, A. C. Mueller, F. Pougheon, A. Richard, Yu. E. Penionzhkevich, A. G. Artukh, A. V. Belozyorov, S. M. Lukyanov, R. Anne, P. Bricault, C. Détraz, M. Lewitowicz, Y. Zhang, Yu. S. Lyutostansky, M. V. Zverev, D. Bazin, and W. D. Schmidt-Ott. *Phys. Rev. C*, **41**(3):937, 1990. [5](#), [84](#), [112](#)
- [11] M. Fauerbach, D. J. Morrissey, W. Benenson, B. A. Brown, M. Hellström, J. H. Kelley, R. A. Kryger, R. Pfaff, C. F. Powell, and B. M. Sherrill. *Phys. Rev. C*, **53**(2):647, 1996. [5](#)
- [12] A. Schiller, T. Baumann, J. Dietrich, S. Kaiser, W. Peters, and M. Thoennessen. *Phys. Rev. C*, **72**(3):037601, 2005. [5](#)
- [13] H. Sakurai, S.H. Lukyanov, M. Notani, N. Aoi, D. Beaumel, N. Fukuda, M. Hirai, E. Ideguchi, N. Imai, and M. Ishihara. *Phys. Lett. B*, **448**:180, 1999. [5](#)

- [14] B. A. Brown, P. G. Hansen, and J. A. Tostevin. *Phys. Rev. Lett.*, **90**:159201, 2003. [5](#), [12](#)
- [15] A. Schiller et al. *in preparation*. [5](#), [9](#)
- [16] S. W. Padgett, Vandana Tripathi, S. L. Tabor, P. F. Mantica, C. R. Hoffman, M. Wiedeking, A. D. Davies, S. N. Liddick, W. F. Mueller, A. Stolz, and B. E. Tomlin. *Phys. Rev. C*, **72**:064330, 2005. [6](#), [61](#), [63](#), [76](#), [77](#), [80](#), [81](#), [82](#)
- [17] T. Nilsson, G. Nyman, and K. Riisager. *Hyper. Inter.*, **129**:67, 2000. [6](#), [10](#)
- [18] B. H. Wildenthal, M. S. Curtin, and B. A. Brown. *Phys. Rev. C*, **28**(3):1343, 1983. [8](#), [14](#), [26](#), [102](#), [103](#)
- [19] <http://www.nndc.bnl.gov/ensd/>. [8](#), [10](#), [49](#), [62](#), [66](#), [71](#), [75](#), [78](#), [90](#), [93](#), [105](#), [109](#), [119](#), [120](#)
- [20] B. Alex Brown and W. A. Richter. *Phys. Rev. C*, **72**:057301, 2005. [7](#), [8](#)
- [21] M. Stanoiu, F. Azaiez, Zs. Dombradi, O. Sorlin, B. A. Brown, M. Belleguic, D. Sohler, M. G. Saint Laurent, M. J. Lopez-Jimenez, Y. E. Penionzhkevich, G. Sletten, N. L. Achouri, J. C. Angelique, F. Becker, C. Borcea, C. Bourgeois, A. Bracco, J. M. Daugas, Z. Dlouhy, C. Donzaud, J. Duprat, Zs. Fulop, D. Guillemaud-Mueller, S. Grevy, F. Ibrahim, A. Kerek, A. Krasznahorkay, M. Lewitowicz, S. Leenhardt, S. Lukyanov, P. Mayet, S. Mandal, H. van der Marel, W. Mittig, J. Mrazek, F. Negoita, F. De Oliveira-Santos, Zs. Podolyak, F. Pougheon, M. G. Porquet, P. Roussel-Chomaz, H. Savajols, Y. Sobolev, C. Stodel, J. Timar, and A. Yamamoto. *Phys. Rev. C*, **69**:034312, 2004. [7](#), [8](#), [11](#), [12](#), [70](#), [71](#), [73](#), [74](#), [76](#)
- [22] P. G. Thirolf, B. V. Pritychenko, B. A. Brown, P. D. Cottle, M. Chromik, T. Glasmacher, G. Hackman, R. W. Ibbotson, K. W. Kemper, and T. Otsuka. *Phys. Lett. B*, **485**:16, 2000. [8](#), [11](#), [70](#)
- [23] E. Becheva, Y. Blumenfeld, E. Khan, D. Beaumel, J. M. Daugas, F. Delaunay, Ch-E. Demonchy, A. Drouart, M. Fallot, A. Gillibert, L. Giot, M. Grasso, N. Keeley, K. W. Kemper, D. T. Khoa, V. Lapoux, V. Lima, A. Musumarra, L. Nalpas, E. C. Pollacco, O. Roig, P. Roussel-Chomaz, J. E. Sauvestre, J. A. Scarpaci, F. Skaza, and H. S. Than. *Phys. Rev. Lett.*, **96**:012501, 2006. [8](#), [12](#), [70](#)
- [24] Z. Elekes, Zs. Dombradi, N. Aoi, S. Bishop, Zs. Fulop, J. Gibelin, T. Gomi, Y. Hashimoto, N. Imai, N. Iwasa, H. Iwasaki, G. Kalinka, Y. Kondo, A. A. Korshennikov, K. Kurita, M. Kurokawa, N. Matsui, T. Motobayashi, T. Nakamura, T. Nakao, E. Yu. Nikolskii, T. K. Ohnishi, T. Okumura, S. Ota, A. Perera, A. Saito, H. Sakurai, Y. Satou, D. Sohler, T. Sumikama, D. Suzuki, M. Suzuki, H. Takeda, S. Takeuchi, Y. Togano, and Y. Yanagisawa. *Phys. Rev. C*, **74**(1):017306, 2006. [8](#)

- [25] E. Khan, Y. Blumenfeld, Nguyen Van Giai, T. Suomijrvi, N. Alamanos, F. Auger, G. Col, N. Frascaria, A. Gillibert, T. Glasmacher, M. Godwin, K. W. Kemper, V. Lapoux, I. Lhenry, F. Marechal, D. J. Morrissey, A. Musumarra, N. A. Orr, S. Ottini-Hustache, P. Piattelli, E. C. Pollacco, P. Roussel-Chomaz, J. C. Roynette, D. Santonocito, J. E. Sauvestre, J. A. Scarpaci, and C. Volpe. *Phys. Lett. B*, **490**:45, 2000. [8](#)
- [26] M. D. Belbot, J. J. Kolata, K. Lamkin, R. J. Tighe, M. Zahar, R. Harkewicz, D. J. Morrissey, N. A. Orr, R. M. Ronningen, B. M. Sherrill, J. A. Winger, and M. Carpenter. *Phys. Rev. C*, **51**:2372, 1995. [9](#)
- [27] R. K. Gupta, S. Kumar, and W. Scheid. *J. Phys. G: Nucl. Part. Phys.*, **21**:L27, 1995. [9](#)
- [28] R. K. Gupta, S. Kumar, M. Balasubramaniam, G. Munzenberg, and W. Scheid. *J. Phys. G: Nucl. Part. Phys.*, **28**:699, 2002. [9](#)
- [29] Rituparna Kanungo, Masami Chiba, Naohito Iwasa, Shunji Nishimura, Akira Ozawa, Chhanda Samanta, Toshimi Suda, Takeshi Suzuki, Takayuki Yamaguchi, Tao Zheng, and Isao Tanihata. *Phys. Rev. Lett.*, **88**:142502, 2002. [9](#)
- [30] N. Aoi, K. Yoneda, H. Miyatake, H. Ogawa, Y. Yamamoto, E. Ideguchi, T. Kishida, T. Nakamura, M. Notani, H. Sakurai, T. Ternishi, H. Wu, S. S. Yamamoto, Y. Watanabe, A. Yoshida, and M. Ishihara. *Nucl. Phys. A*, **616**:181c, 1997. [10](#)
- [31] D. Anthony. *Decay Studies of the Neutron-Rich Nuclides  $^{19}\text{N}$  and  $^{20}\text{N}$* . PhD thesis, Michigan State University, 2000. [11](#)
- [32] K. W Scheller, J. Gorres, J. G. Ross, M. Wiescher, R. Harkewicz, D. J. Morrissey, B. M. Sherrill, M. Steiner, N. A. Orr, and J. A. Winger. *Phys. Rev. C*, **49**:46, 1994. [11](#)
- [33] K. W Scheller, J. Gorres, S. Vouzoukas, M. Wiescher, B. Pfeiffer, K. L. Kratz, D. J. Morrissey, B. M. Sherrill, M. Steiner, M. Hellstrom, and J. A. Winger. *Nucl. Phys. A*, **582**:109, 1995. [11](#), [102](#)
- [34] C. S. Sumithrarachchi, D. W. Anthony, P. A. Lofy, and D. J. Morrissey. *Phys. Rev. C*, **74**:024322, 2006. [11](#), [45](#), [71](#), [73](#), [76](#)
- [35] D. Cortina-Gil, J. Fernandez-Vazquez, T. Aumann, T. Baumann, J. Benlliure, M. J. G. Borge, L. V. Chulkov, U. Datta Pramanik, C. Forssen, L. M. Fraile, H. Geissel, J. Gerl, F. Hammache, K. Itahashi, R. Janik, B. Jonson, S. Mandal, K. Markenroth, M. Meister, M. Mocko, G. Munzenberg, T. Ohtsubo, A. Ozawa, Y. Prezado, V. Pribora, K. Riisager, H. Scheit, R. Schneider, G. Schrieder, H. Simon, B. Sitar, A. Stolz, P. Strmen, K. Summerer, I. Szarka, and H. Weick. *Phys. Rev. Lett.*, **93**:062501, 2000. [12](#), [14](#), [70](#)
- [36] F. Azaiez. *Nucl. Phys. A*, **704**:37, 2002. [11](#)

- [37] M. Belleguic, M. J. Lopez-Jimenez, M. Stanoiu, F. Azaiez, M. G. Saint-Laurent, O. Sorlin, N. L. Achouri, J. C. Anglique, C. Bourgeois, C. Borcea, J.-M. Daugas, C. Donzaud, F. De Oliveira-Santos, J. Dupart, S. Grevy, D. Guillemaud-Mueller, S. Leenhardt, M. Lewitowicz, Yu.-E. Penionzhkevich, and Yu. Sobolev. *Nucl. Phys. A*, 682:136c, 2001. [11](#), [15](#), [99](#)
- [38] A. C. Mueller, D. Guillemaud-Mueller, J. C. Jacmart, E. Kashy, F. Pougheon, A. Richard, A. Staudt, H. V. Klapdor-Kleingrothaus, M. Lewitowicz, R. Anne, P. Bricault, C. Detraz, Yu. E. Penionzhkevich, A. G. Artukh, A. V. Belozyorov, and S. M. Lukyanov. D. Bazin. W. D. Schmidt-Ott. *Nucl. Phys. A*, **513**:1, 1990. [13](#), [14](#), [61](#), [63](#), [109](#)
- [39] P. L. Reeder, R. A. Warner, W. K. Hensley, D. J. Vieira, and J. M. Wouters. *Phys. Rev. C*, 44(4):1435, 1991. [13](#), [14](#), [77](#), [108](#), [109](#)
- [40] K. Yoneda, N. Aoi, H. Iwasaki, H. Sakurai, H. Ogawa, T. Nakamura, W.-D. Schmidt-Ott, M. Schafer, M. Notani, N. Fukuda, E. Ideguchi, T. Kishida, S. S. Yamamoto, and M. Ishihara. *Phys. Rev. C*, **67**:014316, 2003. [13](#), [61](#), [108](#), [109](#)
- [41] E. Sauvan, F. Carstouiu, N. A. Orr, J. C. Anglique, W. N. Catford, N. M. Clarke, M. Mac Cormick, N. Curtis, M. Freer, S. Grvy, C. Le Brun, M. Lewitowicz, E. Liegard, F. M. Marques, P. Roussel-Chomaz, M. G. Saint Laurent, M. Shawcross, and J. S. Winfield. *Phys. Lett B*, 491:1, 2000. [14](#), [26](#)
- [42] N. A. Orr, L. K. Fifield, W. N. Catford, and C. L. Woods. *Nucl. Phys. A*, 491:457, 1989. [15](#)
- [43] S. Michimasa, S. Shimoura, H. Iwasaki, M. Tamaki, S. Ota, N. Aoi, H. Baba, N. Iwasa, S. Kanno, S. Kubono, K. Kurita, M. Kurokawa, T. Minemura, T. Motobayashi, M. Notani, H. J. Ong, A. Saito, H. Sakurai, E. Takeshita, S. Takeuchi, Y. Yanagisawa, and A. Yoshida. *Phys. Lett B*, 638:146, 2006. [15](#), [99](#), [100](#), [102](#), [116](#)
- [44] H. von Groote, E. R. Hilf, and K. Takahashi. *At. Data and Nucl. Data Tables*, 17:418, 1976. [14](#), [109](#)
- [45] A. H. Wapstra, G. Audi, and R. Hoekstra. *At. Data and Nucl. Data Tables*, 39:281, 1988. [14](#), [109](#)
- [46] D. H. Wilkinson, A. Gallmann, and D. E. Alburger. *Phys. Rev. C*, **18**:401, 1978. [26](#)
- [47] Samuel S. M. Wong. *Introductory Nuclear Physics*. John Wiley and Sons, Inc., second edition edition, 1998. [26](#)
- [48] Private communication. [26](#), [75](#), [109](#), [115](#)
- [49] D. Bazin, O. Tarasov, M. Lewitowicz, and O. Sorlin. *Nucl. Instr. and Meth. A*, **482**:307, 2002. [29](#)

- [50] L. F. Oliveira, R. Donangelo, and J. O. Rasmussen. *Phys. Rev. C*, **19**:826, 1979. [29](#)
- [51] D. J. Morrissey, B. M. Sherrill, M. Steiner, A. Stolz, and I. Wiedenhoever. *Nucl. Instr. and Meth. B*, **204**:90, 2003. [29](#)
- [52] J. P. Biersack and L. Haggmark. *Nucl. Instr. and Meth. B*, **174**:257, 1980. [32](#)
- [53] <http://docs.nsl.msu.edu/daq>. [34](#)
- [54] R. Harkewicz, D. J. Morrissey, B. A. Brown, J. A. Nolen Jr., N. A. Orr, B. M. Sherrill, J. S. Winfield, and J. A. Winger. *Phys. Rev. C*, **44**:2365, 1991. [36](#)
- [55] D. R. Tilley, H. R. Weller, and C. M. Cheves. *Nucl. Phys. A*, **564**:1, 1993. [39](#)
- [56] S. Grévy, N. L. Achouri, J. C. Angélique, C. Borcea, A. Buta, F. De Oliveira, M. Lewitowicz, E. Liénard, T. Martin, F. Negoita, N. A. Orr, J. Peter, S. Pietri, and C. Timis. *Phys. Rev. C*, **63**:037302, 2001. [39](#)
- [57] D. E. Alburger and D. H. Wilkinson. *Phys. Rev. C*, **13**:835, 1976. [39](#)
- [58] W. T. Milner; Oak Ridge National Laboratory, Unpublished. [41](#)
- [59] R. Harkewicz. *The Beta-decay Branching Ratios of The Neutron-rich Nucleus  $^{15}\text{B}$* . PhD thesis, Michigan State University, 1992. [50](#)
- [60] R. A. Cecil, B. D. Anderson, and R. Madey. *Nucl. Instr. and Meth.*, **161**:439, 1979. [50](#)
- [61] W. F. Mueller, J. A. Church, T. Glasmacher, D. Gutknecht, G. Hackman, P. G. Hansen, Z. Hu, K. L. Miller, and P. Quirin. *Nucl. Instrum. Methods Phys. Res. A*, **466**:492, 2001. [51](#)
- [62] Y. E. Penionzhkevich. *Phys. Of Atomic Nucl.*, **64**:1121, 2001. [61](#), [77](#), [108](#), [109](#)
- [63] A. T. Reed, O. Tarasov, R. D. Page, D. Guillemaud-Mueller, Yu. E. Penionzhkevich, R. G. Allatt, J. C. Angélique, R. Anne, C. Borcea, V. Burjan, W. N. Catford, Z. Dlouhý, C. Donzaud, S. Grévy, M. Lewitowicz, S. M. Lukyanov, F. M. Marqués, G. Martinez, A. C. Mueller, P. J. Nolan, J. Novák, N. A. Orr, F. Pougheon, P. H. Regan, M. G. Saint-Laurent, T. Siiskonen, E. Sokol, O. Sorlin, J. Suhonen, W. Trinder, and S. M. Vincent. *Phys. Rev. C*, **60**:024311, 1999. [61](#), [77](#), [81](#), [84](#), [87](#)
- [64] H. Bateman. *Proc. Cambridge Philos. Soc.*, **15**:423, 1910. [60](#), [91](#), [93](#), [123](#)
- [65] F. Hubert, J.P. Dufour, R. Del Moreal, A. Fleury, D. Jean, M.S. Pravikoff, H. Delagrangé, H. Geissel, K.-H. Schmidt, and E. Hanelt. *Z. Phys. A*, **333**:237, 1989. [67](#)

- [66] A.F. Lisetskiy L. Weissman, O. Arndt, U. Bergmann, B.A. Brown, J. Cederkall, I. Dillmann, O. Hallmann, L. Fraile, S. Franchoo, L. Gaudefroy, U. Koster, K.-L. Kratz, B. Pfeiffer, O. Sorlin, and ISOLDE coolaboration. *J. Phys. G*, **31**:553, 2005. [67](#), [97](#), [112](#)
- [67] Cary N. Davids, David R. Goosman, David E. Alburger, A. Gallmann, G. Guillaume, D. H. Wilkinson, and W. A. Lanford. *Phys. Rev. C*, **9**(1):216, 1974. [69](#)
- [68] D. E. Alburger, C. J. Lister, J. W. Olness, and D. J. Millener. *Phys. Rev. C*, **23**(5):2217, 1981. [69](#)
- [69] W. R. Harris and D. E. Alburger. *Phys. Rev. C*, **1**(1):180, 1970. [70](#)
- [70] E. K. Warburton and D. E. Alburger. *Phys. Rev. C*, **23**(3):1234, 1981. [70](#)
- [71] N. B. Gove and M. J. Martin. *Nucl. Data Tables*, 10:205, 1971. [75](#), [82](#), [107](#)
- [72] J.R. Terry, D. Bazin, B.A. Brown, C.M. Campbell, J.A. Church, J.M. Cook, A.D. Davies, D.-C. Dinca, J. Enders, A. Gade, T. Glasmacher, P.G. Hansen, J.L. Lecouey, T. Otsuka, B. Pritychenko, B. Sherrill, J.A. Tostevin, Y. Utsuno, K. Yoneda, and H. Zwahlen. *Phys. Lett. B*, **640**:86, 2006. [76](#), [78](#)
- [73] K.H. Wilcox, N.A. Jelley, R.B. Wozniak, G.J. Weisenmiller, H.L. Harney, and J. Cerny. *Phys. Rev. Lett.*, **30**:866, 1973. [77](#)
- [74] C.L. Woods, L.K. Fifield, R.A. Bark, P.V. Drumm, and M.A.C. Hotchkis. *Nucl. Phys. A*, **437**:454, 1985. [77](#)
- [75] M. Belleguic, F. Azaiez, Zs. Dombradi, D. Sohler, M. J. Lopez-Jimenez, T. Otsuka, M. G. Saint-Laurent, O. Sorlin, M. Stanoiu, Y. Utsuno, Yu.-E. Penionzhkevich, N. L. Achouri, J. C. Angelique, C. Borcea, C. Bourgeois, J. M. Daugas, F. De Oliveira-Santos, Z. Dlouhy, C. Donzaud, J. Duprat, Z. Elekes, S. Grevy, D. Guillemaud-Mueller, S. Leenhardt, M. Lewitowicz, S. M. Lukyanov, W. Mitig, M. G. Porquet, F. Pougheon, P. Roussel-Chomaz, H. Savajols, Y. Sobolev, C. Stodel, and J. Timar. *Phys. Rev. C*, **72**:054316, 2005. [77](#)
- [76] P. M. Endt. *Nucl. Phys. A*, 521:1, 1990. [81](#), [93](#), [97](#), [104](#)
- [77] R. B. Firestone. *Nucl. Data Sheet*, 106:1, 2005. [97](#), [100](#)
- [78] P. M. Endt, J. Blachot, R. B. Firestone, and J. Zipkin. *Nucl. Phys. A*, **633**:1, 1998. [102](#), [103](#)
- [79] L. Weissman, O. Arndt, U. Bergmann, J. Cederkall, I. Dillmann, O. Hallmann, L. Fraile, S. Franchoo, L. Gaudefroy, U. Koster, K. L. Kratz, A. F. Lisetskiy, B. Pfeiffer, O. Sorlin, and S. Tabor. *Phys. Rev. C*, 70:057306, 2004. [102](#), [103](#), [105](#), [106](#)

- [80] K. I. Pearce, N. M. Clarke, R. J. Griffiths, P. J. Simmonds, A. C. Dodd, D. Barker, J. B. A. England, M. C. Mannion, and C. A. Ogilvie. *Phys. Rev. C*, **35**:1617, 1987. [102](#), [104](#)
- [81] Sangjin Lee, S. L. Tabor, T. Baldwin, D. B. Campbell, I. Calderin, C. Chandler, M. W. Cooper, C. R. Hoffman, K. W. Kemper, J. Pavan, A. Pipidis, M. A. Riley, and M. Wiedeking. *Phys. Rev. C*, 73:044321, 2006. [102](#), [104](#), [105](#), [106](#), [117](#), [119](#)
- [82] E.R. Flynn and J.D. Garrett. *Phys. Rev. C*, **9**:210, 1974. [103](#)
- [83] B. A. Brown and W. A. Richter. *Phys. Rev. C*, **74**:034315, 2006. [112](#)
- [84] V. Tripathi, S. L. Tabor, P. F. Mantica, C. R. Hoffman, M. Wiedeking, A. D. Davies, S. N. Liddick, W. F. Mueller, T. Otsuka, A. Stolz, B. E. Tomlin, Y. Utsuno, and A. Volya. *Phys. Rev. Lett.*, **94**:162501, 2005. [117](#)